

Doctoral thesis

Doctoral theses at NTNU, 2024:57

Zibo Zheng

Weakly nonlinear surface waves on vertically sheared currents

NTNU
Norwegian University of Science and Technology
Thesis for the Degree of
Philosophiae Doctor
Faculty of Engineering
Department of Energy and Process Engineering



Norwegian University of
Science and Technology

Zibo Zheng

Weakly nonlinear surface waves on vertically sheared currents

Thesis for the Degree of Philosophiae Doctor

Trondheim, February 2024

Norwegian University of Science and Technology
Faculty of Engineering
Department of Energy and Process Engineering



Norwegian University of
Science and Technology

NTNU

Norwegian University of Science and Technology

Thesis for the Degree of Philosophiae Doctor

Faculty of Engineering

Department of Energy and Process Engineering

© Zibo Zheng

ISBN 978-82-326-7714-6 (printed ver.)

ISBN 978-82-326-7713-9 (electronic ver.)

ISSN 1503-8181 (printed ver.)

ISSN 2703-8084 (online ver.)

Doctoral theses at NTNU, 2024:57

Printed by NTNU Grafisk senter

Abstract

Extreme waves, also known as rogue waves, have much larger heights than surrounding waves, which are of great danger to ships and coastal structures. A subsurface shear current is able to change the properties of the surface waves significantly. Hence, rogue waves may be altered by a shear current. This thesis aims to investigate the effects of a vertically sheared background flow on weakly nonlinear deep-water waves with both a statistical study for irregular random waves and a deterministic study for a focused wave group.

First, we extend the theory of Longuet-Higgins [J. Fluid Mech. **12**, 321 (1962)] to allow for a background shear flow that varies with depth. The theory is valid up to second order in wave steepness. It is applicable to arbitrarily strong shear currents and broadband waves. The linear dispersion relation and wave field are solved by the Direct Numerical Method (DIM) proposed by Li and Ellingsen [J. Geophys. Res.: Oceans, **124**, 2527 (2019)]. The second-order corrections are solved numerically from the Rayleigh equation with the finite volume method.

To examine the effects of different shear currents on the statistics of weakly nonlinear waves, we perform simulations and generate random waves with both numerical cases and real-world data from the mouth of the Columbia River. For numerical cases, a JONSWAP spectrum and several different linear and exponential shear currents with reasonable strength are adopted. The real-world data is measured by Zippel and Thomson [J. Geophys. Res.: Oceans **122**, 3311 (2017)]. We investigate the probability density function of wave surface elevation and maxima, exceedance probability distribution of crest height, maximum wave crest among a number of consecutive waves, and the skewness of the surface elevation. The simulating results of both numerical cases and real-world data demonstrate that an opposing shear enhances the probability of rogue waves and skewness, while a following shear has opposite influences compared with the no-current case.

Knowing that the shear current can have a considerable influence on rogue waves, we proceed to examine the focused wave group on different shear

currents, which acts as a representation of the rogue wave event. The investigations are carried out for both long-crested linear and weakly nonlinear waves.

1. Linear waves: For a prescribed initial wave group surface elevation, different techniques are used to derive explicit approximate expressions of wave surface elevation and orbital velocity profiles. The approximate expressions agree well with the numerical results from DIM. Compared to the case without a current, orbital velocities are significantly amplified by a following shear and suppressed by an opposing shear; an amplification factor is defined from here, and the approximate expression of the amplification factor with respect to the parameters of a shear current is derived explicitly. Compared to the no-current case, a reasonably strong shear alters the orbital velocities substantially. The present expressions can be tested by future experiments at the NTNU fluid mechanics laboratory.
2. Weakly nonlinear waves: The nonlinear waves are solved numerically similar to the statistical study. We use Gaussian energy spectra to generate linear wave groups. The exponential shear currents are assumed to propagate at an arbitrary angle to the wave groups. The measured wave spectra and shear currents are also used in the calculation for comparison. The wave surface elevation and horizontal velocity beneath the focused point are analyzed. Our results suggest that in regions of strong oceanic currents, substantial error occurs in predicting wave impact on ocean structures if the shear currents are ignored.

Preface

This thesis is submitted to the Norwegian University of Science and Technology (NTNU) for partial fulfilment of the requirements for the degree of philosophiae doctor. The doctoral work has been performed at the Department of Energy and Process Engineering (EPT) from September 2019 to September 2023. The work has been supervised by Professor Simen Å Ellingsen and co-supervised by Associate Professor Yan Li from the University of Bergen.

The research was funded by the China Scholarship Council under Grant Agreement No. 201906060137.

The thesis consists of 5 chapters and 3 scientific papers.

Article I

Statistics of weakly nonlinear waves on currents with strong vertical shear

Zibo Zheng, Yan Li, Simen Å. Ellingsen

Physical Review Fluids, Volume 8, Issue 1, Page 014801

Author's contributions: All authors conceived the idea of the setup. ZZ carried out the detailed tasks for the derivation of the theory under the supervision of YL. ZZ performed the numerical simulation, analyzed the relevant numerical results, produced all figures, and contributed to writing the first draft. All authors discussed the results and commented on the manuscript.

Article II

Dispersive wave focusing on a shear current. Part 1: Linear approximations

Simen Å. Ellingsen, Zibo Zheng, Malek Abid, Christian Kharif, Yan Li

Submitted to: Water Waves

Author's contributions: All authors conceived the idea of the setup. SÅE derived the theory, all of which was double checked by ZZ and corrected where necessary. SÅE and ZZ performed all numerical calculations, analysed the relevant numerical results, and produced all figures except for figure 1. All authors discussed the results and commented on the manuscript.

Article III

Dispersive wave focussing on a shear current. Part 2: effect of weak non-linearity

Zibo Zheng, Yan Li, Simen Å. Ellingsen

Author's contributions: All authors conceived the idea of the setup. ZZ and YL designed the detailed setup. ZZ adapted the theory from Article I to the case of focussing waves, performed the numerical simulation, analyzed the relevant numerical results, and contributed to writing the manuscript. All authors discussed the results and commented on the manuscript.

Additional abstracts not formally included in this thesis

Interaction of weakly nonlinear focused wave group with strong shear flow

Zibo Zheng, Yan Li, Simen Å. Ellingsen

WISE conference 2023

Weakly nonlinear focused wave group on arbitrary shear based on second-order theory

Zibo Zheng, Yan Li, Simen Å. Ellingsen

EGU General Assembly 2023

Statistical analysis of weakly nonlinear waves on vertically sheared flows

Zibo Zheng, Yan Li, Simen Å. Ellingsen

WISE conference 2022

Extreme waves on vertically sheared flows: Statistical analysis of weakly nonlinear waves

Zibo Zheng, Yan Li, Simen Å. Ellingsen

EGU General Assembly 2022

Statistical properties of weakly nonlinear deepwater surface waves in a depth-dependent background flow

Zibo Zheng, Yan Li, Simen Å. Ellingsen
WISE conference 2021

Weakly nonlinear surface gravity waves in a depth-dependent background flow

Zibo Zheng, Yan Li, Simen Å. Ellingsen
EGU General Assembly 2021

21st September, 2023

Zibo Zheng

Acknowledgements

This thesis is completed under the meticulous guidance of my supervisor, Professor Simen Å. Ellingsen. I am extremely grateful to you for introducing me to the field of ocean waves and guiding me in scientific research. The journey of pursuing a doctoral degree is not easy. But I always feel lucky for studying in your group.

I am deeply indebted to my co-supervisor, Associate Professor Yan Li. You put too much effort into my Ph.D. project, which is way beyond the scope of a co-supervisor. It has been inspiring and a joy working with you. You spent too much time on our papers. I really appreciate it.

What my supervisors taught me is not only how to do scientific research, but also how to become a valuable person. If I can get a chance to stay in academia in the future, I will try to make an attentive, meticulous, and responsible supervisor like you.

I have been part of the Thermofluids group for 4 years. I got a lot of help from present and past Ph.D. students and postdocs. The journey with your companion becomes more joyful. Many kind people persuaded me not to work too long, but I did not listen. Hope nobody hates me for being a 'weirdo'. Anyway, it is my honor to meet all of you.

I will be far away, I hope all of you can lead happy lives.

To my family, your enduring support, understanding, and encouragement sustained me during the most challenging times of this journey. Your sacrifices were never in vain.

Thank you all for being part of this remarkable journey.

纸短情长，伏惟珍重

郑子波

Contents

Abstract	iii
Preface	iv
Acknowledgements	vii
Contents	ix
List of Figures	xvi
1 Introduction	1
1.1 Motivation	1
1.1.1 Rogue waves	1
1.1.2 Spatial focusing	3
1.1.3 Focusing due to dispersion	4
1.1.4 Focusing due to modulational instability	5
1.2 Wave statistics	5
1.3 Waves modified by shear current	7
1.4 Objectives	8
1.5 Thesis outline	9
2 Methodology	11
2.1 Problem statement	11

2.1.1	Governing equations	12
2.1.2	Boundary conditions	13
2.1.3	Perturbation expansion	13
2.1.4	Rayleigh equation	14
2.2	Solution with linear shear	16
2.2.1	Linear solution	17
2.2.2	Second-order correction	18
2.2.3	Waves of a narrowband spectrum	19
2.3	Solution with exponential shear	20
2.3.1	Linear solution	21
2.3.2	Second-order correction	22
2.4	Numerical method	24
2.5	Instability	24
2.5.1	Triad resonance	25
2.5.2	A critical layer in the flow	26
2.5.3	Langmuir circulation	27
2.5.4	Summary	28
3	Numerical cases	29
3.1	Power energy spectra for linear waves	30
3.2	Shear current profiles	32
3.3	Measured data from the Columbia River	33
4	Summary of research articles and conclusions	35
4.1	Summary of articles	35
4.2	Future work	37
	Bibliography	39

Research articles in full text

48

List of Figures

1.1	Locations of lost supercarriers due to rogue waves between 1969 and 1994 (Kharif and Pelinovsky 2003). Figure copyright C. Kharif and E. Pelinovsky, used with permission. . . .	2
1.2	The wave surface elevation measured at the Draupner platform.	3
1.3	Sketch of random wave surface, (a) narrowband waves, and (b) broadband waves.	7
2.1	Sketch for the wave-current system.	12
2.2	Geometry: a wave group propagating on a linear shear current.	16
2.3	The dispersion relation of gravity waves in the (a) absence and (b) presence of a linear shear current. Solid & dashed line: using ‘+’ & ‘-’ in Eq. (2.17).	17
2.4	Geometry: a wave group propagating on an exponential shear current.	20
2.5	Procedure of the numerical method.	23
2.6	Langmuir vortex cells. Black line: streamline computed from Akselsen and Ellingsen (2019) (Eq. B4). Blue and orange colors refer to clockwise and anticlockwise rotations, respectively.	27
3.1	Power energy spectra with the same bandwidth ($\nu = 0.327$). $\gamma = 3.3$ is adopted in the JONSWAP spectrum.	31
3.2	Velocity profiles $U(z)$ and shear strength δ for exponential and linear shear currents. (a) Shear profiles with $U_0 = 0.2$, $\alpha = 2.5$ and $S = -0.2$ and (b) shear strength $ \delta $ for the two profiles in (a).	32

3.3 Power energy spectra and shear profiles measured at the mouth of the Columbia River by Zippel and Thomson (2017). The wave spectra in (a)–(c) are fitted with JONSWAP-type expression (3.1) with free parameters $\tilde{\alpha}_J^*$, ω_p^* and γ : (a) $\gamma = 4.87$ & $\omega_p^* = 0.69$ rad/s, (b) $\gamma = 1.62$ & $\omega_p^* = 1.19$ rad/s, and (c) $\gamma = 3.18$ & $\omega_p^* = 2.50$ rad/s. $\tilde{\alpha}_J$ depends on the prescribed wave steepness of the simulations. Its values here are not meaningful. 33

3.4 Velocity profiles and strength of the currents at the Columbia River. (a) dotted and ‘+’ lines refers to measured data, solid lines denote fitted curves with exponential function $U(z) = U_0[\exp(\alpha z) - 1]$. (b) The shear strength δ of the two fitted curves in (a) with ‘ZT’ the current from Zippel and Thomson (2017) and ‘KN’ the current from Kilcher and Nash (2010). 34

Nomenclature

The nomenclature in the attached publications at the end of the thesis may differ from the one given here and may include items that are not listed here. This list is not exhaustive.

Abbreviations

DIM	direct integration method
EPD	exceedance probability distribution
KN	measured data from Klicher and Nash
PDF	probability density function
ZT	measured data from Zippel and Thomson

Greek symbols

α	parameter of exponential shear current
δ	shear strength
$\Delta\omega$	width of frequency bin
ε	wave steepness
γ	parameter of JONSWAP spectrum
ν	bandwidth parameter
Ω	intrinsic wave frequency
ω	wave frequency
ω_0	characteristic wave frequency
ω_i	imaginary part of complex wave frequency

ω_p	peak wave frequency
ω_r	real part of complex wave frequency
ϕ	initial phase
ψ	wave phase function
σ	standard deviation of wave surface elevation
σ_S	parameter of Gaussian spectrum
θ	angle between the directions of shear current and x axis
$\tilde{\alpha}_G$	parameter of Gaussian spectrum
$\tilde{\alpha}_J$	parameter of JONSWAP spectrum
$\tilde{\delta}$	small arbitrary constant
Ψ	stream function
ζ	wave surface elevation
ζ_c	wave crest height

Latin symbols

(k_x, k_y)	wavenumber in (x, y) direction
(x, y, z)	Cartesian coordinate system
\mathbf{c}_g	group velocity vector
\mathbf{k}	wave number vector
\mathbf{U}	shear current velocity vector
\mathbf{V}	wave velocity vector
$\mathcal{A}_+, \mathcal{A}_-, \mathcal{W}, \mathfrak{R}$	parameters for hypergeometric function
\mathcal{C}	arbitrary constant
\mathcal{F}	forcing term of combined boundary condition
\mathcal{N}	forcing term of Rayleigh equation
\mathcal{R}	take the real part

\tilde{w}_1, \tilde{w}_2	general solution of second-order bound wave on exponential shear current
\tilde{w}_3	particular solution of second-order bound wave on exponential shear current
${}_2F_1$	hypergeometric function
a	linear wave amplitude
b	distance between two adjacent rays
BFI	Benjamin-Feir Index
c	phase velocity
c_g	group velocity scalar
g	gravitational acceleration
H	wave height
H_s	significant wave height
k	length of wave number vector
k_0	characteristic wavenumber
L_c	characteristic length
m_j	j -th moment of the wave spectrum
p	wave pressure
S	parameter of linear shear current
S_G	Gaussian spectrum
S_J	JONSWAP spectrum
t	time coordinate
u	wave velocity in x -direction
U_0	parameter of exponential shear current
u_c	characteristic velocity
v	wave velocity in y -direction

w wave velocity in z -direction

z_c critical layer

Modifiers

$(\cdot)^*$ dimensional variable

$(\cdot)'$ derivative with respect to z

$(\cdot)^{(1)}$ linear wave

$(\cdot)^{(2)}$ second-order bound wave

$(\cdot)_+$ superharmonic wave

$(\cdot)_-$ subharmonic wave

$(\cdot)_1$ first linear wave

$(\cdot)_2$ second linear wave

$(\cdot)_3$ 3-dimensional variable

$(\cdot)_i$ i -th linear wave

$(\hat{\cdot})$ Fourier space

$\nabla(\cdot)$ gradient

$\partial(\cdot)$ derivative with respect to (\cdot)

1

Introduction

1.1 Motivation

1.1.1 Rogue waves

Rogue or freak waves denote the waves with large amplitudes, appearing surprisingly in the ocean, which are sometimes catastrophic events. The ships and floating platforms could be destroyed by such large waves. From 1969 to 1994, more than 22 supercarriers were lost due to rogue wave events ([Kharif and Pelinovsky 2003](#)), which caused 525 casualties. The locations of these accidents are shown in Fig. 1.1. Due to the rareness of rogue waves, most of the measured data for them were obtained by oil platforms ([Dysthe et al. 2008](#)).

One well-known rogue wave event was recorded at the Draupner platform on January 1st, 1995 ([Hayer and Andersen 2000](#)), which happened in the North Sea and had been studied by many authors. This event is called the New Year's Wave because of the special date. The wave surface elevation is shown in Fig. 1.2. The significant wave height of this event was 11.8 m but the highest wave crest exceeded 18.5 m. Another example of a rogue wave was measured on November 17, 1984, at the Gorm field in the North Sea. The largest wave crest was 11 m while the significant wave height was 5 m. On November 9, 2007, the Andrea rogue wave was recorded in the North

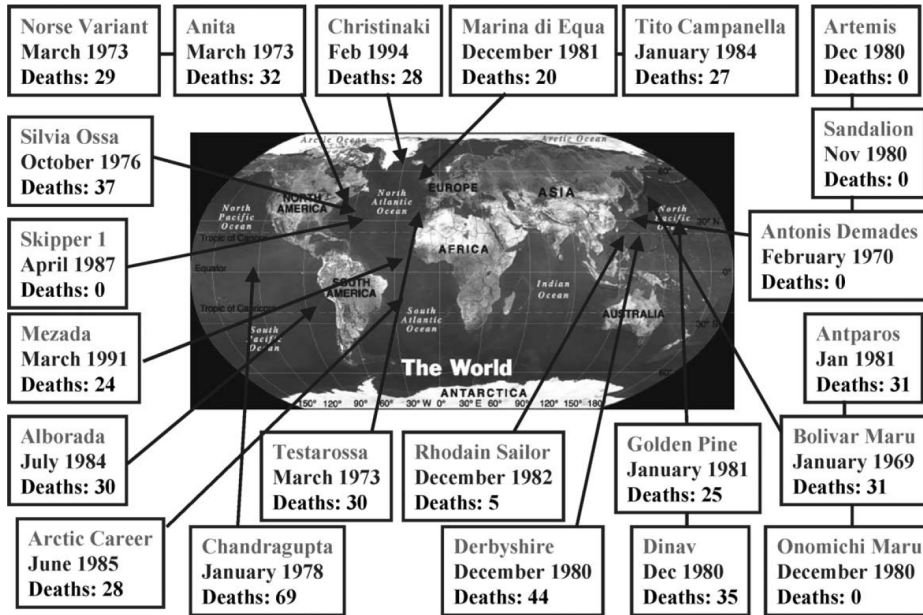


Figure 1.1: Locations of lost supercarriers due to rogue waves between 1969 and 1994 (Kharif and Pelinovsky 2003). Figure copyright C. Kharif and E. Pelinovsky, used with permission.

Sea from a bridge between two Ekofish platforms (Donelan and Magnusson 2017). This giant wave had a crest height of 14.9 m, which exceeded the significant wave height by a factor of 1.62. The above three rogue waves have been well studied (Adcock et al. 2011, Donelan and Magnusson 2017). Many other rogue wave events have also been observed since the 19th century. Liu (2007) gave a chronology of such events up to 2007. Didenkulova et al. (2023) collected 429 rogue wave events from 2005 to 2021.

For the definition of rogue waves, this thesis follows the criteria used by Dysthe et al. (2008), which is given by

$$\zeta_c/H_s > 1.25, \quad (1.1)$$

where, H is zero-upcrossing wave height, H_s is significant wave height and ζ_c refers to wave crest height. Here, H_s is given by $H_s = 4\sigma$ with σ the standard deviation of the wave surface elevation ζ . There is a disadvantage with this criteria. The rogue waves could also occur in a calm sea, which are not necessarily ‘wall of water’. However, this point is not considered in the thesis.

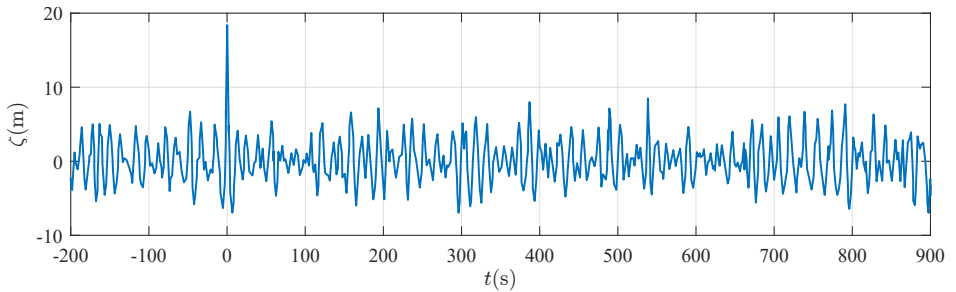


Figure 1.2: The wave surface elevation measured at the Draupner platform.

Several physical mechanisms could serve as possible explanations of rogue waves, they are (Adcock and Taylor 2014, Dysthe et al. 2008, Kharif and Pelinovsky 2003, Kharif et al. 2008, Slunyaev et al. 2011)

- Spatial focusing
- Focusing due to dispersion
- Focusing due to modulational instability

But there is no consensus on which one actually causes rogue wave events in the real world. Although the three mechanisms could take place in the absence of a shear current, it might have a significant influence on them. The focus of this thesis is on the impact of shear currents on dispersive focusing.

1.1.2 Spatial focusing

Varying bottoms or currents could refract waves and produce caustic points, at which the rogue waves can happen. Spatial focusing can be explained by ray theory through the wave action balance equation, which can be expressed as (Kharif and Pelinovsky 2003, Mei et al. 2005)

$$\frac{\partial}{\partial t} \left(\frac{a^2}{\omega} \right) + \nabla \cdot \left(\frac{\mathbf{c}_g a^2}{\omega} \right) = 0, \quad (1.2)$$

where a is wave amplitude, ω is wave frequency and c_g is group velocity of a 2-dimensional wave. It can be used to calculate the wave amplitude a at different locations. The wave action flux can be found through Eq. (1.2)

$$c_g b a^2 = \text{const} \quad \text{with } c_g = |\mathbf{c}_g|, \quad (1.3)$$

where $b(x, y)$ is the distance between two adjacent rays. Eq. (1.3) means the action flux between two rays should be a constant. Clearly, $b = 0$ or

$c_g = 0$ can lead to an infinite wave amplitude within the framework of this linear theory.

The intersecting rays are caused by $b = 0$, which can be achieved by varying the bottom topography. The wave can be refracted by an uneven bottom and its direction changes correspondingly. However, the *infinity* wave amplitude never happens in the real world. It just becomes larger than neighboring waves. At such a point, the linear theory is not valid. Also, with more rays overlapping at the same point the local amplitude increases (Kharif et al. 2008). The most extreme event can be accomplished by cylindrical waves (Brekhovskikh 2012).

The other candidate for spatial focusing requires $c_g = 0$, which means the group velocity at this point is zero. This condition can be achieved by introducing an opposing current. For a horizontal current $\mathbf{U}(x, y)$, the group velocity of a 3-dimensional monochromatic wave is give by

$$\mathbf{c}_g = \frac{d\omega}{d\mathbf{k}} = \frac{d\Omega}{d\mathbf{k}} + \mathbf{U}, \quad (1.4)$$

where, Ω is the intrinsic frequency. With proper opposing current, the group velocity could become a singularity, and the energy transfer is stopped. Such a singularity can not happen in nature. The waves can be captured and trapped in the middle of the current and grow larger, which might be the physical mechanism of extreme events in Agulhas current (Lavrenov 1998, Shrira and Slunyaev 2014).

1.1.3 Focusing due to dispersion

This kind of physical mechanism is also called dispersive focusing. The waves in the ocean are very random, which are superpositions of infinitely many regular waves. Due to the dispersion relation, these waves have different phase velocities, which explains why the sea surface changes all the time. Also, because of wave dispersion, large waves could happen when faster waves catch up with slower ones so that many crests or troughs pile on top of each other. This process is called wave focusing and this location is the focal point. With more wave crests coming to the focal point, the local wave becomes larger.

Forming a giant wave is of fairly low probability and it is a purely statistical problem. For this reason, it is common to perform statistical analysis for this physical mechanism, which will be explained in detail in Section 1.2. This type of focusing only relies on wave dispersion, which is more likely to occur than the other two physical mechanisms mentioned in Section 1.1.1.

Considering finite water depth, due to the refraction of the bottom topography, the wave properties can be affected. Therefore, the statistical results of the random waves show a substantial departure from the case with a flat bottom. Several different bathymetries have been well studied. If the waves propagate over a sloping bottom, from a deeper domain to a shallower domain, the probability of a rogue wave has a local maximum near the shallower side (Mendes and Kasparian 2022, Trulsen et al. 2012). A submerged step (Bolles et al. 2019, Li et al. 2021), shoal (Mendes and Kasparian 2023, Trulsen et al. 2020), or smooth bar (Lawrence et al. 2022) have a similar influence on the wave statistics. Dispersive focusing can also be affected by the shear current, which will be explained in detail in Section 1.3.

1.1.4 Focusing due to modulational instability

The uniform wave train is unstable to a small sideband disturbance, which was discovered by Benjamin and Feir (1967). Hence, this phenomenon is also called the Benjamin-Feir (BF) instability. It refers to a continuous energy transfer from the primary motion to sidebands. The uniform wave train could become highly irregular and its maximum amplitude could be significantly enhanced.

The ratio $BFI = \text{wave steepness}/\text{bandwidth}$ is defined as the BF index (Janssen 2003). The bandwidth parameter is used to describe how broad the wave spectrum is. Wave groups with $BFI > 1$ have been shown to be unstable (Dysthe et al. 2003, Janssen 2003). Hence, BF instability requires the wave spectrum to be *narrow*. Also, it is observed that the BF instability only occurs in *long-crested* sea (Gramstad and Trulsen 2007).

Although BF instability can be used to generate rogue waves in laboratory settings, the *narrowband* and *long-crested* constraints mean it rarely occurs in fully developed seas.

It is worth noting that a shear current can enhance or weaken the BF instability, which depends on the relative direction of the waves and the current (Steer et al. 2020, Toffoli et al. 2015). The BF instability can be almost completely attenuated by a tailored shear (Pizzo et al. 2023).

1.2 Wave statistics

For linear random waves, the probability density function of wave surface elevation satisfies Gaussian distribution due to the central limit theorem,

$$p(\zeta) = \frac{1}{\sqrt{2\pi}\sigma} \exp\left(-\frac{\zeta^2}{2\sigma^2}\right), \quad (1.5)$$

where ζ denotes the wave surface elevation and $p(\cdot)$ is the probability density function. It is called the Gaussian Sea. The wave surface is represented by a superposition of many linear monochromatic waves. If the wave spectrum is fairly narrow, the exceedance probability of crest heights is given by the Rayleigh distribution

$$P(\zeta_c > \zeta) = \exp\left(-8\frac{\zeta^2}{H_s^2}\right), \quad (1.6)$$

which was shown by [Longuet-Higgins \(1952\)](#). The occurrence probability of rogue waves is then about 10^{-4} . With a broad wave spectrum, the exceedance probability of crest heights should not satisfy the Rayleigh distribution. But the probability of rogue waves is still approximately 10^{-4} ([Zheng et al. 2023](#)).

One clear difference between narrowband and broadband waves lies in the zero-crossing wave crest shape. Here, zero-crossing means the points on the wave surface with $\zeta = 0$. For narrowband waves, there is only one local peak between two adjacent zero-crossings, which denotes the crest height. However, if the wave spectrum has finite width, several local peaks can occur on one wave crest, which are called wave maxima. And the highest one represents the crest height. The comparison between narrowband and broadband waves is shown in [Fig. 1.3](#).

In the ocean, waves usually have steeper crests and flatter troughs, which can be better described by second-order theory than linear theory ([Forristall 2000](#)). Also, the prediction including second-order corrections fits the field measurement well in most circumstances ([Dysthe et al. 2008](#), [Fedele et al. 2016](#)). However, seeking explicit expressions for the probability density function of wave surface elevation and crest heights becomes tough. Such expressions can only be found by adopting the narrowband assumption ([Socquet-Juglard et al. 2005](#), [Tayfun 1980](#)) or by approximation ([Longuet-Higgins 1963](#), [Srokosz 1998](#)). Considering that the wave spectrum in fully developed seas is not very narrow, [Tayfun and Fedele \(2007\)](#) and [Fedele and Tayfun \(2009\)](#) derived the probability distribution of wave heights and crests for a broadband sea state, which gave good results in predicting large waves.

Without a shear current, the higher-order theory has been well established for narrowband ([Dysthe and Trulsen 1999](#), [Gramstad and Trulsen 2007](#), [Janssen 2003](#), [Onorato et al. 2001](#)) and broadband ([Annenkov and Shrira 2006](#), [Fedele et al. 2016](#), [Fujimoto et al. 2019](#), [Janssen 2003](#), [Onorato et al.](#)

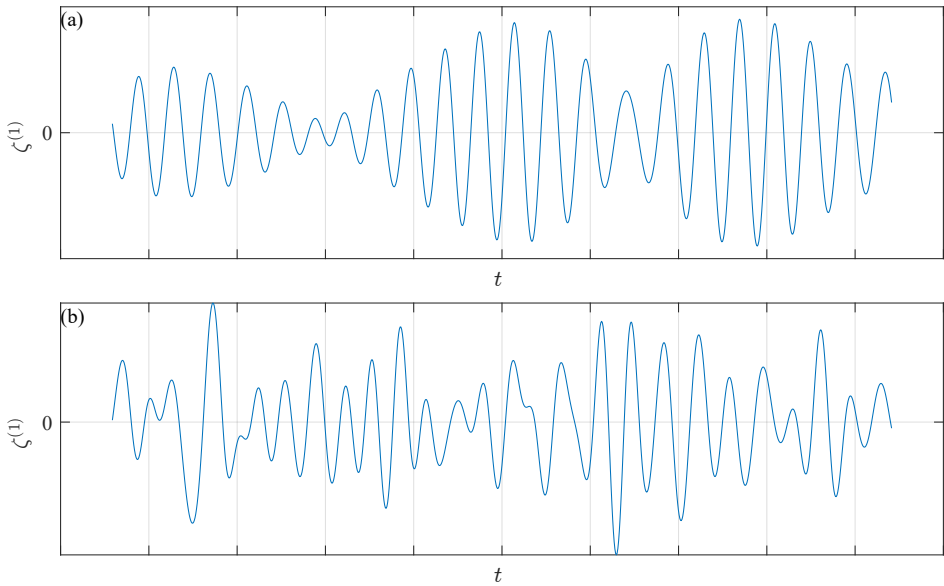


Figure 1.3: Sketch of random wave surface, (a) narrowband waves, and (b) broadband waves.

2005, Toffoli et al. 2009, Xiao et al. 2013) waves. The fully nonlinear theory was also discussed extensively using different methods (Gibbs and Taylor 2005, Henderson et al. 1999, Klahn et al. 2021, Zheng et al. 2020). Taking an arbitrary shear current into consideration can introduce dramatic complexity to the wave theory. Therefore, in the presence of a shear current, only second-order theory is developed in this thesis, which can also show us whether higher-order theory is worth doing.

1.3 Waves modified by shear current

Waves and shear currents coexist in nature (Dalrymple 1973). For a wave-current system, if the shear current is omitted, the wave properties could be predicted with substantial error (Peregrine 1976), which of course depends on the strength of the current. The currents, from small to large scale, generally can be categorized into four types, they are

- Surface current: generated by wind,
- River delta: due to the freshwater jet from the river on top of the heavier salt water beneath,
- Tidal current: influenced by the sun and moon, occurs in the coastal regions,

- Ocean circulation: correlated with air temperatures, sea levels, and extreme weather events. It normally does not have considerable vertical shear.

The shear current could be of large magnitude and strong surface shear. One of the most famous cases is the Columbia River current. It could be the possible reason for extreme waves and has been investigated intensively (González 1984, González et al. 1981, Kilcher and Nash 2010, Zippel and Thomson 2017). The recent work of Zippel and Thomson (2017) provides detailed data measured at the mouth of the Columbia River. Hence, the Columbia River current is also considered in this thesis. It is shown that this current has considerable influence on both wave statistics and kinematics.

It is well known that potential theory has been extensively employed as the simplest solution for modeling ocean waves. The velocity potential can be introduced to simplify the equations. The analytical solution can be solved by virtue of perturbation expansion, which was first found by Stokes (1847). Then Stokes' theory was extended to fifth order in wave steepness (Fenton 1985, Skjelbreia and Hendrickson 1960) for a monochromatic wave. Given the fact that the waves in the ocean are a superposition of infinitely many monochromatic waves, the nonlinear wave-wave interaction was developed to second-order by Ref. (Dalzell 1999, Longuet-Higgins and Stewart 1962). The Ref. (Hasselmann 1962, Phillips 1960, Zakharov 1968) uncovered that the wave dynamics is dominated by third-order processes.

However, for a wave-shear current system, the analytical solution is hard to find due to the failure of the potential theory. The waves on a few specific shear profiles can be solved analytically, such as linear (Dalrymple 1974, Ellingsen and Brevik 2013, Thompson 1949), exponential (Abdullah 1949, Young and Wolfe 2014), cosine (Kirby and Chen 1989) and powerlaw (Fenton 1973, Lighthill 1953) profiles. For complicated shear profiles, piecewise linear (Smeltzer and Ellingsen 2017, Zhang 2005) and approximation method (Ellingsen and Li 2017, Shrira 1993, Zakharov and Shrira 1990) have been successfully used. To account for more general and realistic shear currents, Li and Ellingsen (2019) developed a direct integration method (DIM), which solves the linear dispersion relation numerically. This thesis extends the work by Li and Ellingsen (2019) to allow for weakly nonlinear waves.

1.4 Objectives

As mentioned above, rogue waves can be extremely dangerous events. However, the mechanism of their formation is still unclear. The aim of this thesis

is to investigate the influence of shear currents on the properties of extreme waves. This problem is studied from two aspects: wave statistics and wave kinematics.

How vertically sheared currents modify the Benjamin-Feir instability has been studied several times ([Baumstein 1998](#), [Francius and Kharif 2017](#), [Pizzo et al. 2023](#), [Steer et al. 2020](#), [Thomas et al. 2012](#)). However, to the best of our knowledge, there is no study concerning the influence of an arbitrary shear current on the probability of rogue waves based on broadband theory. For wave statistics, this work seeks to figure out the impacts of different shear currents on several aspects: the distribution of wave surface elevation, wave maxima, and crest height.

In this thesis, we consider only rogue waves which are formed by dispersive focusing. Hence, the prescribed focused wave group can be used to investigate the kinematics of such extreme waves. For linear waves, approximate expressions for wave surface elevation and velocity may be derived. If the second-order correction is introduced, the shear current might have an even more considerable influence on particle velocity. Hence, the possible presence of a shear current needs to be considered when performing simulations of the wave-structure interaction ([Dalrymple 1973](#), [Xin et al. 2023](#)).

1.5 Thesis outline

The organization of this thesis is as follows. The theory and numerical method are given in Chapter 2. The numerical cases are presented in Chapter 3. Chapter 4 summarises the three publications, and the full-length papers are given at the end of the thesis.

2

Methodology

In this Chapter, the theory developed by [Zheng et al. \(2023\)](#) is reviewed. It is based on several assumptions; they are listed here.

- The fluid flow is assumed to be inviscid and incompressible.
- The waves are driven by gravity. Surface tension is neglected.
- The shear current is allowed to be strong, which can affect the waves but is not affected by the waves.
- The currents can vary in the vertical direction, but are uniform in the horizontal plane.
- The shear currents are large-scale. Its variation in time and horizontal directions is negligible compared to fast-varying waves.

2.1 Problem statement

The fluid flow is assumed to be homogeneous, stationary, and rotational. Therefore, potential wave theory cannot be used. The geometry is assumed to be three-dimensional with (x^*, y^*) the horizontal plane and z^* the vertical axis pointing upward. Here, the superscript $*$ is used to represent the dimensional variables. Time is represented by t^* . We also assume that the water is deep for linear and second-order waves. A Cartesian coordinate system is adopted and the $z^* = 0$ is set at still water surface in the absence of waves and a current. The velocity field is a superposition of wave

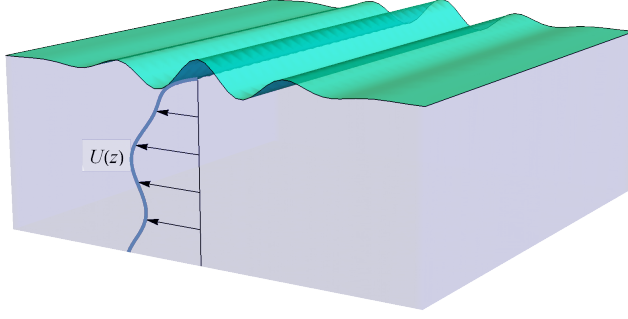


Figure 2.1: Sketch for the wave-current system.

velocities $\mathbf{V}_3^*(x^*, y^*, z^*, t^*) = (\mathbf{V}^*(x^*, y^*, z^*, t^*), w^*(x^*, y^*, z^*, t^*))$ and shear current velocities $\mathbf{U}_3^*(z^*) = (\mathbf{U}^*(z^*), 0)$. The velocity $\mathbf{U}^*(x^*, y^*, z^*, t^*)$ and $\mathbf{V}^*(x^*, y^*, z^*, t^*) = (u^*(x^*, y^*, z^*, t^*), v^*(x^*, y^*, z^*, t^*))$ refer to the current and wave velocity in the horizontal plane, where $u^*(x^*, y^*, z^*, t^*)$, $v^*(x^*, y^*, z^*, t^*)$ and $w^*(x^*, y^*, z^*, t^*)$ refer to the wave velocity in the x^* -, y^* - and z^* - directions, respectively. The wave surface elevation and the wave-induced change in the pressure are expressed as $\zeta^*(x^*, y^*, t^*)$ and $p^*(x^*, y^*, z^*, t^*)$, respectively.

For brevity, the space vector (x^*, y^*, z^*) and time t^* of the above variables are omitted in the rest of this chapter.

2.1.1 Governing equations

The waves propagate atop a depth-dependent background current. The sketch of such a wave-current system is shown in Fig. 2.1. The governing equations contain the continuity equation and the Euler equation, which can be expressed as (Peregrine 1976)

$$\nabla_3^* \cdot \mathbf{V}_3^* = 0, \quad (2.1)$$

$$\partial_{t^*} \mathbf{V}_3^* + (\mathbf{V}_3^* \cdot \nabla_3^*) \mathbf{U}_3^* + (\mathbf{U}_3^* \cdot \nabla_3^*) \mathbf{V}_3^* + \nabla_3^* p^* = -(\mathbf{V}_3^* \cdot \nabla_3^*) \mathbf{V}_3^*, \quad (2.2)$$

for $-\infty < z^* < \zeta^*$. Here $\partial_{(\dots)}$ refers to $\frac{\partial}{\partial(\dots)}$ and $\nabla_3^* = (\nabla^*, \partial_{z^*})$ represents the three-dimensional gradient operator with ∇^* the gradient operator in horizontal plane.

The dimensional variables are nondimensionalized by a characteristic length $L_c^* = g^*/\omega_0^{*2}$ and a characteristic velocity $u_c^* = g^*/\omega_0^*$, where g^* is gravitational acceleration and ω_0^* is characteristic wave frequency. Using L_c^* and u_c^* yields dimensionless gravitational acceleration $g = 1$. The density is

absorbed into pressure. Hence, dimensional mass is not introduced.

Then the dimensionless governing equations become

$$\nabla_3 \cdot \mathbf{V}_3 = 0; \quad (2.3)$$

$$\partial_t \mathbf{V}_3 + (\mathbf{V}_3 \cdot \nabla_3) \mathbf{U}_3 + (\mathbf{U}_3 \cdot \nabla_3) \mathbf{V}_3 + \nabla_3 p = -(\mathbf{V}_3 \cdot \nabla_3) \mathbf{V}_3, \quad (2.4)$$

2.1.2 Boundary conditions

The pressure at the air-water interface is constant. Here we assume it is 0 without loss of generality. Then the kinematic and dynamic boundary at the wave surface can be expressed as

$$p - \zeta = 0 \quad \text{and} \quad w = \partial_t \zeta + (\mathbf{V} + \mathbf{U}) \cdot \nabla \zeta \quad \text{for} \quad z = \zeta, \quad (2.5)$$

The water is assumed to be infinitely deep, and the boundary condition at the bottom is given by

$$(u, v, w, p) = 0 \quad \text{for} \quad z \rightarrow -\infty \quad (2.6)$$

2.1.3 Perturbation expansion

Perturbation expansion is a mathematical technique which can be used to solve complex wave phenomena approximately. Wave solutions will depend on a small quantity $\varepsilon = ka$, which is known as the wave steepness. Also, ε is presumed to be far less than unity (Dean and Dalrymple 1991). Then the wave solutions can be written in such a form

$$\mathbf{V}_3 = \varepsilon \mathbf{V}_3^{(1)} + \varepsilon^2 \mathbf{V}_3^{(2)}, \quad (2.7a)$$

$$\zeta = \varepsilon \zeta^{(1)} + \varepsilon^2 \zeta^{(2)}, \quad (2.7b)$$

$$p = \varepsilon p^{(1)} + \varepsilon^2 p^{(2)}, \quad (2.7c)$$

where, the superscript ‘(1)’ and ‘(2)’ refer to linear terms and second-order corrections, respectively.

Following the theory developed by Stokes (1847), the linear waves should take the form

$$\begin{bmatrix} \mathbf{V}_3^{(1)}(\mathbf{x}, z, t) \\ \zeta^{(1)}(\mathbf{x}, t) \\ p^{(1)}(\mathbf{x}, z, t) \end{bmatrix} = \mathcal{R} \left\{ \frac{1}{4\pi^2} \int \begin{bmatrix} \hat{\mathbf{V}}_3^{(1)}(\mathbf{k}, z) \\ \hat{\zeta}^{(1)}(\mathbf{k}) \\ \hat{p}^{(1)}(\mathbf{k}, z) \end{bmatrix} e^{i\psi(\mathbf{k}, \mathbf{x}, t)} d\mathbf{k} \right\}, \quad (2.8)$$

where, $\psi = \mathbf{k} \cdot \mathbf{x} - \omega t + \phi$ refers to the wave phase with \mathbf{k} the wavenumber vector, $\mathbf{x} = (x, y)$ the horizontal spatial vector, and ϕ the initial phase. \Re represents taking the real part. Here, the variables with and without a hat symbol $\hat{\cdot}$ refer to the variables in Fourier space and in real space, respectively.

Similarly, the second-order correction can be described by

$$\begin{aligned} \begin{bmatrix} \mathbf{V}_3^{(2)}(\mathbf{x}, z, t) \\ \zeta^{(2)}(\mathbf{x}, t) \\ p^{(2)}(\mathbf{x}, z, t) \end{bmatrix} &= \Re \left\{ \frac{1}{16\pi^4} \iint \begin{bmatrix} \hat{\mathbf{V}}_{3,+}^{(2)}(\mathbf{k}_1, \mathbf{k}_2, z) \\ \hat{\zeta}_+^{(2)}(\mathbf{k}_1, \mathbf{k}_2) \\ \hat{p}_+^{(2)}(\mathbf{k}_1, \mathbf{k}_2, z) \end{bmatrix} e^{i(\psi_1 + \psi_2)} d\mathbf{k}_1 d\mathbf{k}_2 \right\} \\ &+ \Re \left\{ \frac{1}{16\pi^4} \iint \begin{bmatrix} \hat{\mathbf{V}}_{3,-}^{(2)}(\mathbf{k}_1, \mathbf{k}_2, z) \\ \hat{\zeta}_-^{(2)}(\mathbf{k}_1, \mathbf{k}_2) \\ \hat{p}_-^{(2)}(\mathbf{k}_1, \mathbf{k}_2, z) \end{bmatrix} e^{i(\psi_1 - \psi_2)} d\mathbf{k}_1 d\mathbf{k}_2 \right\}. \end{aligned} \quad (2.9)$$

where, $\psi_i = \psi(\mathbf{k}_i, \mathbf{x}, t)$ $i = 1, 2$ is a shorthand. The subscripts ‘+’ and ‘-’ denote superharmonic and subharmonic waves, respectively, which come from the interaction between linear waves. \mathbf{k}_1 and \mathbf{k}_2 refer to the wavenumbers of two interacting linear waves.

2.1.4 Rayleigh equation

To solve the boundary value problem constituted by Eq. (2.3)-(2.6), Eq. (2.7) is inserted to separate the linear and second-order terms. Then one linear and one second-order boundary value problem can be obtained. For linear waves, a Direct Numerical Method (DIM) was developed by [Li and Ellingsen \(2019\)](#) for the wave-current system, which can solve the linear dispersion relation and wave fields. With the assistance of DIM, only second-order corrections remain to be solved.

By eliminating the horizontal velocity $\mathbf{V}^{(2)}$ and pressure $p^{(2)}$, the governing equations are arranged into a so-called Rayleigh equation (or inviscid Orr-Sommerfeld equation), which can be written

$$(\partial_t + \mathbf{U} \cdot \nabla) \nabla_3^2 w^{(2)} - \mathbf{U}'' \cdot \nabla w^{(2)} = \mathcal{N}^{(2)}(\mathbf{x}, z, t), \quad (2.10a)$$

for $-\infty < z < \zeta$, where $(\dots)' = \partial_z(\dots)$. Doing the same elimination to the boundary conditions, yields

$$\begin{aligned} (\partial_t + \mathbf{U} \cdot \nabla)^2 w^{(2)'} - \mathbf{U}' \cdot (\partial_t + \mathbf{U} \cdot \nabla) \nabla w^{(2)} - \nabla^2 w^{(2)} \\ = \mathcal{F}^{(2)}(\mathbf{x}, z, t) \quad \text{for } z = 0, \end{aligned} \quad (2.10b)$$

$$w^{(2)} = 0 \quad \text{for } z \rightarrow -\infty, \quad (2.10c)$$

where the forcing terms $\mathcal{F}^{(2)}$ and $\mathcal{N}^{(2)}$ refer to the interaction between linear waves; they are expressed as

$$\mathcal{N}^{(2)} = \nabla \cdot [(\mathbf{V}_3^{(1)} \cdot \nabla_3) \mathbf{V}^{(1)}]' - \nabla^2 [(\mathbf{V}_3^{(1)} \cdot \nabla_3) w^{(1)}], \quad (2.11a)$$

$$\begin{aligned} \mathcal{F}^{(2)} = & -\nabla^2 (\mathbf{V}^{(1)} \cdot \nabla \zeta^{(1)}) - [\nabla^2 (\partial_t + \mathbf{U} \cdot \nabla) p^{(1)'} - \nabla^2 w^{(1)'}] \zeta^{(1)} \\ & - \zeta^{(1)} \nabla^2 (\mathbf{U}' \cdot \nabla) p^{(1)} + (\partial_t + \mathbf{U} \cdot \nabla) \nabla \cdot [(\mathbf{V}_3^{(1)} \cdot \nabla_3) \mathbf{V}^{(1)}]. \end{aligned} \quad (2.11b)$$

Similar to Eq. (2.9), the forcing terms $\mathcal{F}^{(2)}$ and $\mathcal{N}^{(2)}$ should also be transformed into Fourier space

$$\begin{aligned} \begin{bmatrix} \mathcal{F}^{(2)}(\mathbf{x}, z, t) \\ \mathcal{N}^{(2)}(\mathbf{x}, z, t) \end{bmatrix} = & \mathcal{R} \left\{ \frac{1}{16\pi^4} \iint \begin{bmatrix} \hat{\mathcal{F}}_+^{(2)}(\mathbf{k}_1, \mathbf{k}_2, z) \\ \hat{\mathcal{N}}_+^{(2)}(\mathbf{k}_1, \mathbf{k}_2, z) \end{bmatrix} e^{i(\psi_1 + \psi_2)} d\mathbf{k}_1 d\mathbf{k}_2 \right\} \\ & + \mathcal{R} \left\{ \frac{1}{16\pi^4} \iint \begin{bmatrix} \hat{\mathcal{F}}_-^{(2)}(\mathbf{k}_1, \mathbf{k}_2, z) \\ \hat{\mathcal{N}}_-^{(2)}(\mathbf{k}_1, \mathbf{k}_2, z) \end{bmatrix} e^{i(\psi_1 - \psi_2)} d\mathbf{k}_1 d\mathbf{k}_2 \right\}. \end{aligned} \quad (2.12)$$

Now the boundary value problem in Fourier \mathbf{k} space is obtained, given by

$$\hat{w}_\pm^{(2)''} - \left(|\mathbf{k}_\pm|^2 + \frac{\mathbf{k}_\pm \cdot \mathbf{U}''}{\mathbf{k}_\pm \cdot \mathbf{U} - \omega_\pm} \right) \hat{w}_\pm^{(2)} = \frac{\hat{\mathcal{N}}_\pm^{(2)}(\mathbf{k}_\pm, z)}{\mathbf{k}_\pm \cdot \mathbf{U} - \omega_\pm}, \quad (2.13a)$$

for $-\infty < z < 0$, and boundary conditions

$$\begin{aligned} -(\mathbf{k}_\pm \cdot \mathbf{U} - \omega_\pm)^2 \hat{w}_\pm^{(2)'} + [\mathbf{k}_\pm \cdot \mathbf{U}'(\mathbf{k}_\pm \cdot \mathbf{U} - \omega_\pm) + |\mathbf{k}_\pm|^2] \hat{w}_\pm^{(2)} \\ = \hat{\mathcal{F}}_\pm^{(2)}(\mathbf{k}_\pm, z) \quad \text{for } z = 0, \end{aligned} \quad (2.13b)$$

$$\hat{w}_\pm^{(2)} = 0 \quad \text{for } z \rightarrow -\infty. \quad (2.13c)$$

where $\mathbf{k}_\pm = \mathbf{k}_1 \pm \mathbf{k}_2$, $\omega_\pm = \omega(\mathbf{k}_1) \pm \omega(\mathbf{k}_2)$. When the vertical velocity $\hat{w}_\pm^{(2)}$ is solved, the inverse Fourier transform is used to obtain the corresponding variable $w_\pm^{(2)}$ in real space. Inserting into governing equation (2.3) and (2.4) and kinematic boundary condition (2.5), then gives

$$(\partial_t + \mathbf{U} \cdot \nabla) \zeta^{(2)} = w^{(2)} + \zeta^{(1)} w^{(1)'} - \frac{1}{2} \mathbf{U}' \cdot \nabla (\zeta^{(1)})^2 - \mathbf{V}^{(1)} \cdot \nabla \zeta^{(1)}, \quad (2.14a)$$

$$\nabla^2 p^{(2)} = (\partial_t + \mathbf{U} \cdot \nabla) w^{(2)'} - \nabla w^{(2)} \cdot \mathbf{U}' - \nabla \cdot (\mathbf{V}_3^{(1)} \cdot \nabla_3) \mathbf{V}^{(1)}, \quad (2.14b)$$

$$(\partial_t + \mathbf{U} \cdot \nabla) \mathbf{V}^{(2)} = -w^{(2)} \mathbf{U}' - \nabla p^{(2)} - (\mathbf{V}_3^{(1)} \cdot \nabla_3) \mathbf{V}^{(1)} \quad (2.14c)$$

The second-order wave surface elevation $\zeta^{(2)}$, pressure $p^{(2)}$, and horizontal velocity vector $\mathbf{V}^{(2)}$ can be solved from Eq. (2.14).

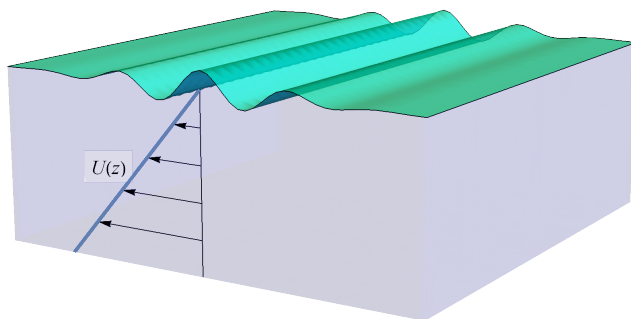


Figure 2.2: Geometry: a wave group propagating on a linear shear current.

2.2 Solution with linear shear

In this section, the shear current profile is assumed to vary linearly with depth. The geometry of the wave-current system is shown in Fig. 2.2. For this simple case, linear wave theory has been extensively studied (Brevik 1978, Constantin et al. 2008, Ellingsen 2014, Ellingsen and Brevik 2013, Hsu et al. 2016, Teles Da Silva and Peregrine 1988). The second-order correction described by Eq. (2.13) can also be solved analytically. The three-dimensional wave solution of the initial value problem on a linear shear current has been solved analytically by Akselsen and Ellingsen (2019). Their solutions are very general but difficult to use.

In the water channel, the waves are usually two-dimensional. Hence, we derive the analytical solution for two-dimensional waves on linear shear current corrected to second order in wave steepness. The solutions are greatly simplified compared with Akselsen and Ellingsen (2019). For this specific case, potential theory still applies (Ellingsen and Brevik 2013, Peregrine 1976), which is easier to solve. However, we still use the theory in Section 2.1 to be consistent with the following sections.

In this section, the y -axis is ignored. The shear profile and wavenumber then reduce to $\mathbf{U} = (U(z), 0)$ in x - z plane and k in x -direction ($k > 0$). Without loss of generality, we assume the linear waves propagate in the x -direction while the direction of the shear current can be the same with or opposite to the x -direction. The expression of the shear current profile is given by

$$U(z) = Sz, \quad (2.15)$$

where S can be positive (opposing shear) or negative (following shear). Here, $U(0) = 0$ is adopted, because we are only interested in the shear rather than the surface current $U(0)$.

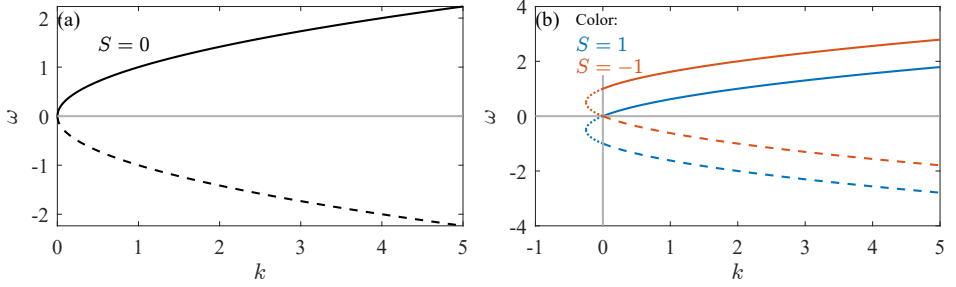


Figure 2.3: The dispersion relation of gravity waves in the (a) absence and (b) presence of a linear shear current. Solid & dashed line: using ‘+’ & ‘-’ in Eq. (2.17).

2.2.1 Linear solution

Considering the linear wave first, the solutions are found as (Akselsen and Ellingsen 2019, Ellingsen 2016, Zheng et al. 2023)

$$\hat{w}^{(1)}(\mathbf{k}, z) = \hat{w}_0^{(1)} e^{kz} \quad (2.16a)$$

$$\hat{u}^{(1)}(\mathbf{k}, z) = i\hat{w}_0^{(1)} e^{kz} \quad (2.16b)$$

$$\hat{p}^{(1)}(\mathbf{k}, z) = -i \frac{(Szk - \omega) - S}{k} \hat{w}_0^{(1)} e^{kz} \quad (2.16c)$$

$$\hat{w}_0^{(1)}(\mathbf{k}) = -i\hat{\zeta}^{(1)}\omega \quad (2.16d)$$

with dispersion relation

$$\omega = -\frac{S}{2} \pm \sqrt{k + \frac{S^2}{4}}, \quad (2.17)$$

It is worth noting, that the ‘+’ and ‘-’ were explained as ‘downstream’ and ‘upstream’ relative to the current in our publication (Zheng et al. 2023), which is correct but not very clear. This will be explained in the following.

The dispersion relation is shown in Fig. 2.3. The gravity wave solution in the absence of a current is plotted in Fig. 2.3 (a) for comparison, where the solid and dashed lines refer to $\omega = \sqrt{k}$ and $\omega = -\sqrt{k}$, respectively. Clearly, the dashed line with negative frequency refers to the wave propagating in the $-k$ direction. Since the wave direction is prescribed at the beginning, only the positive frequency, denoted by the solid line, is considered. Similarly, in Fig. 2.3 (b) the dashed lines are also ignored. The two gray horizontal and vertical lines refer to $\omega = 0$ and $k = 0$, respectively, which separate each curve into three parts. The dotted lines refer to negative k , which cannot

be achieved. Therefore, only solution ‘+’ (solid lines in Figs. 2.3 (a) and (b) in Eq. (2.17) are considered.

However, the solution ‘-’ in Eq. (2.17) is not always ignored. If the surface current $U(0)$ is nonzero, this expression is also likely to contribute to a positive frequency solution. For more information, one can consult Fig. 1 in [Peregrine \(1976\)](#). Therefore, whether the solution ‘-’ is considered depends on the specific current profile and ω .

A different reference can be used to allow negative frequency, in which method the direction of the current is fixed and the wave propagating in both directions is then denoted by ‘+’ and ‘-’ solutions (see, e.g. ([Ellingsen 2014](#), [Shrira 1993](#))).

2.2.2 Second-order correction

Substituting the linear solutions (Eq. (2.16)) and dispersion relation (Eq. (2.17)) into the boundary value problem described by Eq. (2.13), yields

$$\hat{w}_{\pm}^{(2)''} - k_{\pm}^2 \hat{w}_{\pm}^{(2)} = 0 , \quad (2.18a)$$

for $-\infty < z < 0$, and boundary conditions

$$-\omega_{\pm}^2 \hat{w}_{\pm}^{(2)'} + [-k_{\pm} S \omega_{\pm} + k_{\pm}^2] \hat{w}_{\pm}^{(2)} = \hat{\mathcal{F}}_{\pm}^{(2)}(k_{\pm}, z) \quad \text{for } z = 0 , \quad (2.18b)$$

$$\hat{w}_{\pm}^{(2)} = 0 \quad \text{for } z \rightarrow -\infty , \quad (2.18c)$$

with

$$\begin{aligned} \frac{\hat{\mathcal{F}}_{\pm}^{(2)}(k_{\pm}, z)}{\hat{\zeta}_1 \hat{\zeta}_2} = & \omega_{\pm} k_{\pm} \omega_1 \omega_2 \left(-\frac{k_{\pm}}{2} + \frac{k_2 \pm k_1}{2} \right) - k_{\pm}^3 \frac{\omega_1 + \omega_2 + S}{2} \\ & + k_{\pm}^2 \omega_{\pm} \frac{\omega_1^2 + \omega_2^2}{2} . \end{aligned} \quad (2.19)$$

Solving Eq. (2.18) and performing inverse Fourier transform, yield

$$w_{\pm}^{(2)} = \frac{\mathcal{F}_{\pm}^{(2)}}{k_{\pm}^2 - |k_{\pm}| \omega_{\pm}^2 - k_{\pm} S \omega_{\pm}} e^{|k_{\pm}|z} , \quad (2.20a)$$

with

$$\begin{aligned} \frac{\mathcal{F}_{\pm}^{(2)}(x, z, t)}{a_1 a_2 \sin \psi_{\pm}} = & \omega_{\pm} k_{\pm} \omega_1 \omega_2 \left(-\frac{k_{\pm}}{2} + \frac{k_2 \pm k_1}{2} \right) - k_{\pm}^3 \frac{\omega_1 + \omega_2 + S}{2} \\ & + k_{\pm}^2 \omega_{\pm} \frac{\omega_1^2 + \omega_2^2}{2} , \end{aligned} \quad (2.20b)$$

where a_1 and a_2 are the amplitudes of two linear waves in real space. $\psi_{\pm} = k_{\pm}x - \omega_{\pm}t$ is the phase function. For brevity, we define

$$\mathfrak{F}_{\pm}^{(2)} = \frac{\mathcal{F}_{\pm}^{(2)}(x, z, t)}{a_1 a_2 \sin \psi_{\pm}}. \quad (2.20c)$$

The wave surface elevation and velocity can be obtained by inserting Eq. (2.20a) into Eq. (2.14):

$$\zeta_{\pm}^{(2)} = \left[\frac{\mathfrak{F}_{\pm}^{(2)}/\omega_{\pm}}{k_{\pm}^2 - |k_{\pm}|\omega_{\pm}^2 - k_{\pm}S\omega_{\pm}} + \frac{k_{\pm}(\omega_1 + \omega_2 + S)}{2\omega_{\pm}} \right] a_1 a_2 \cos \psi_{\pm}, \quad (2.20d)$$

$$u_{\pm}^{(2)} = \frac{|k_{\pm}|\mathfrak{F}_{\pm}^{(2)}/k_{\pm}}{k_{\pm}^2 - |k_{\pm}|\omega_{\pm}^2 - k_{\pm}S\omega_{\pm}} e^{|k_{\pm}|z} a_1 a_2 \cos \psi_{\pm}. \quad (2.20e)$$

In the absence of a current, using $S = 0$ and the dispersion relation $\omega^2 = k$ (using $g = 1$), we find

$$w_{+}^{(2)} = u_{+}^{(2)} = 0, \quad (2.21a)$$

$$w_{-}^{(2)} = u_{-}^{(2)} = \frac{2|k_1 - k_2|(\omega_1 - \omega_2)\omega_1\omega_2}{(\omega_1 - \omega_2)^2 - |k_1 - k_2|}, \quad (2.21b)$$

$$\zeta_{+}^{(2)} = \frac{k_1 + k_2}{2}, \quad (2.21c)$$

$$\zeta_{-}^{(2)} = \frac{k_1 + k_2}{2} + \frac{\omega_1\omega_2}{2} \times \frac{(\omega_1 - \omega_2)^2 + |k_1 - k_2|}{(\omega_1 - \omega_2)^2 - |k_1 - k_2|}, \quad (2.21d)$$

which agree with Dalzell (1999)'s results (Eq. (25)–(28)). Here, we omit the $a_1 a_2 \cos \psi_{\pm}$ or $a_1 a_2 \sin \psi_{\pm}$ on the right-hand side of the above equation for brevity.

2.2.3 Waves of a narrowband spectrum

In this section, a limiting case is considered, that is, the narrowband wave spectrum. It is well known that under such circumstances, both the surface elevation and the velocity of subharmonic waves should approach zero in the absence of a shear current. It is unknown whether the presence of a linear shear current can change this fact. This point is checked in the rest of this section.

First, the narrowband waves are achieved by assuming $\omega_1 = (1 + \tilde{\delta})\omega_2$ with $\tilde{\delta} \ll 1$. Without loss of generality, $\tilde{\delta}$ is set positive. Using $\omega_{-} \equiv \omega_1 - \omega_2 = \tilde{\delta}\omega_2$, we obtain

$$k_{-} \equiv k_1 - k_2 = \tilde{\delta}\omega_2(\omega_1 + \omega_2 + S). \quad (2.22)$$

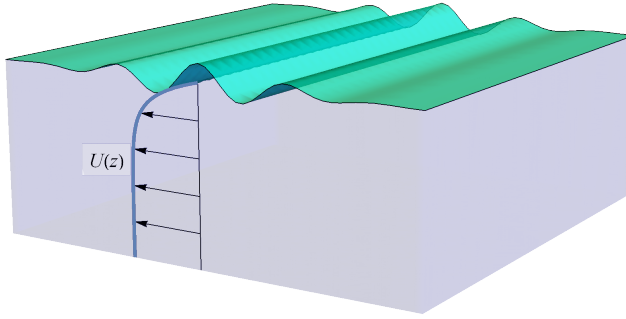


Figure 2.4: Geometry: a wave group propagating on an exponential shear current.

Then, substituting k_- and ω_- in Eq. (2.20), yields

$$w_-^{(2)} = - \frac{\omega_2(\omega_1 + \omega_2 + S)^3}{2(\omega_1 + \omega_2)} \tilde{\delta} a_1 a_2 \sin \psi_- + \mathcal{O}(\tilde{\delta}^2) , \quad (2.23a)$$

$$\zeta_-^{(2)} = - \frac{S(\omega_1 + \omega_2 + S)^2}{2(\omega_1 + \omega_2)} a_1 a_2 \cos \psi_- + \mathcal{O}(\tilde{\delta}) . \quad (2.23b)$$

If an extremely narrowband wave group is considered, we obtain

$$\lim_{\tilde{\delta} \rightarrow 0} w_-^{(2)} = 0 , \quad (2.24a)$$

$$\lim_{\tilde{\delta} \rightarrow 0} \zeta_-^{(2)} = - \frac{S(\omega_1 + \omega_2 + S)^2}{2(\omega_1 + \omega_2)} a_1 a_2 \cos \psi_- . \quad (2.24b)$$

Clearly, the narrowband approximation leads to vanishing velocity but a finite set-up or set-down of the wave surface elevation. However, this point is not very meaningful. The reason is that the linear shear current makes little sense in deep water. But from this point, the results suggest that investigating this problem in finite water depth is worth doing.

2.3 Solution with exponential shear

Except for the linear shear current discussed in the last section, the waves on an exponential shear current can also be solved ‘*analytically*’. The geometry of this case is shown in Fig. 2.4. The linear wave solution and stability have been extensively investigated (Morland and Saffman 1993, Young and Wolfe 2014). This section explores the effect of a shear current on the second-order correction of waves.

2.3.1 Linear solution

First, the shear current is expressed as

$$\mathbf{U}(z) = [U(z) \cos(\theta), U(z) \sin(\theta)], \quad \text{with} \quad (2.25a)$$

$$U(z) = U_0[\exp(\alpha z) - 1], \quad (2.25b)$$

where, θ is the angle between the direction of the shear current and x -axis. Waves propagate in the x -direction, that is, $\mathbf{k} = (k, 0)$. Given such a current, the wave solutions permit

$$w^{(1)}(z) = w_0 e^{kz} {}_2F_1(\mathcal{A}_-, \mathcal{A}_+; \mathfrak{R}; \mathcal{W}(z)) \sin \psi, \quad (2.26a)$$

$$u^{(1)}(z) = i \frac{w^{(1)'}}{k} \cos \psi, \quad (2.26b)$$

$$v^{(1)}(z) = i \frac{U' \sin(\theta) w^{(1)}(z)}{U k \cos(\theta) - \omega} \cos \psi, \quad (2.26c)$$

$$w_0 = -i a \omega \quad (2.26d)$$

with

$$\mathcal{A}_{\pm} = (k \pm \sqrt{\alpha^2 + k^2})/\alpha; \quad \mathfrak{R} = 1 + 2k/\alpha; \quad \mathcal{W}(z) = \frac{kU_0 \cos(\theta) e^{\alpha z}}{\omega + kU_0 \cos(\theta)}, \quad (2.27a)$$

$$w^{(1)'} = k w^{(1)}(z) - \frac{\alpha k U_0 w_0 \cos(\theta)}{(\omega + kU_0 \cos(\theta)) \mathfrak{R}} e^{(k+\alpha)z} {}_2F_1(\mathcal{A}_- + 1, \mathcal{A}_+ + 1; \mathfrak{R} + 1; \mathcal{W}(z)) \sin \psi, \quad (2.27b)$$

where, ${}_2F_1$ is a hypergeometric function, which is expressed as

$${}_2F_1(a, b; c; d) = \sum_{n=0}^{\infty} \frac{ab}{c} \left(\frac{d^n}{n!} \right). \quad (2.28)$$

However, the dispersion relation is still implicit due to the complexity of the hypergeometric function (2.28), and needs to be solved numerically from the combined boundary condition:

$$\omega^2 w'(0) - k(k - \omega \alpha U_0 \cos(\theta)) w(0) = 0. \quad (2.29)$$

Then, the full linear wave solutions have been obtained.

2.3.2 Second-order correction

Considering the second-order correction, we need to solve an inhomogeneous ordinary differential equation (2.13). Similarly to the linear solution (2.26), the two general solutions to Eq. (2.13) take the following form:

$$\tilde{w}_{1,\pm}(z) = e^{k_{\pm}z} {}_2F_1(\mathcal{A}_{1,-}, \mathcal{A}_{1,+}; \mathfrak{R}_1; \mathcal{W}(z)), \quad (2.30a)$$

$$\tilde{w}_{2,\pm}(z) = e^{-k_{\pm}z} {}_2F_1(\mathcal{A}_{2,-}, \mathcal{A}_{2,+}; \mathfrak{R}_2; \mathcal{W}(z)), \quad (2.30b)$$

with

$$\mathcal{A}_{1,\pm} = \frac{k_{\pm} \pm \sqrt{\alpha^2 + k_{\pm}^2}}{\alpha}; \quad \mathfrak{R}_1 = 1 + 2k_{\pm}/\alpha; \quad \mathcal{W}(z) = \frac{k_{\pm} U_0 \cos(\theta) e^{\alpha z}}{\omega_{\pm} + k_{\pm} U_0 \cos(\theta)}, \quad (2.31a)$$

$$\mathcal{A}_{2,\pm} = \frac{-k_{\pm} \pm \sqrt{\alpha^2 + k_{\pm}^2}}{\alpha}; \quad \mathfrak{R}_2 = 1 - 2k_{\pm}/\alpha, \quad (2.31b)$$

A particular solution can be sought using the Wronskian (Bender and Orszag 2013, section 1.3). It is given by

$$\tilde{w}_{3,\pm} = -\tilde{w}_{1,\pm}(z) \int_{\tilde{z}} \frac{\mathcal{N}(\tilde{z}) \tilde{w}_{2,\pm}(z)}{W(\tilde{z})} d\tilde{z} + \tilde{w}_{2,\pm}(z) \int_{\tilde{z}} \frac{\mathcal{N}(\tilde{z}) \tilde{w}_{1,\pm}(z)}{W(\tilde{z})} d\tilde{z}, \quad (2.32)$$

where, $W(\tilde{z}) = W[\tilde{w}_{1,\pm}(z), \tilde{w}_{2,\pm}(z)]$ is the Wronskian.

The general solution $\tilde{w}_{2,\pm}$ needs to be abandoned because of the bottom boundary condition. Then, the full expression of vertical velocity becomes

$$\hat{w}_{\pm}^{(2)} = \mathcal{C} \tilde{w}_{1,\pm}(z) + \tilde{w}_{3,\pm}, \quad (2.33)$$

where, the constant \mathcal{C} is determined from the surface boundary condition. Performing an inverse Fourier transform to Eq. (2.33) and substituting the result back into Eq. (2.14) yields the surface elevation and horizontal velocity. They are straightforward to calculate but not reproduced explicitly due to the bulkiness of the resulting expressions.

It is hard to integrate $\tilde{w}_{3,\pm}$ analytically. One substitution is to do the integral numerically using Simpson's rule or another numerical approximation. However, numerical integration requires a fine mesh, which leads to heavier calculation of hypergeometric function. Hence, the analytical solution in this section is straightforward but time-consuming.

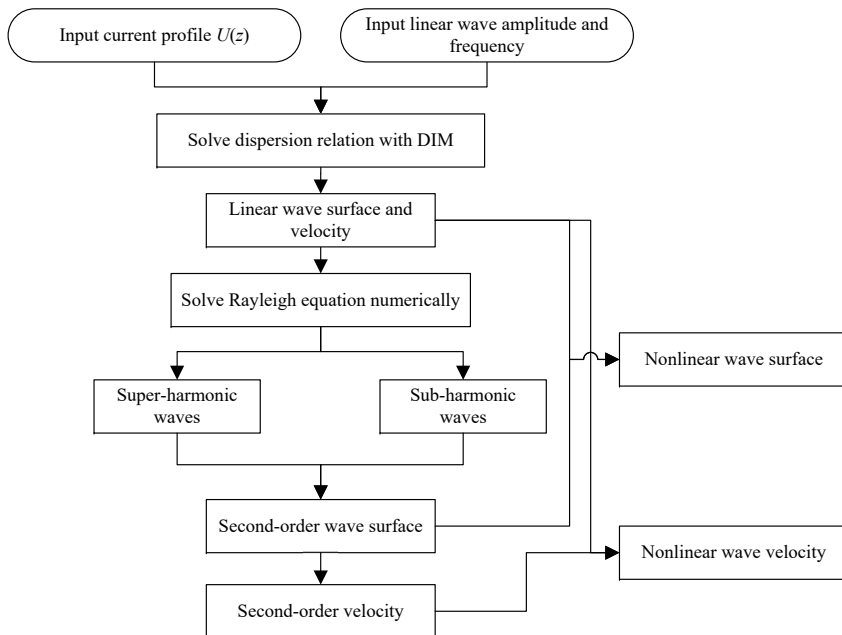


Figure 2.5: Procedure of the numerical method.

2.4 Numerical method

As demonstrated in the previous sections, the linear shear profile is a fairly rough approximation of the real cases. The exponential shear current is more reasonable but difficult to work with analytically. Hence, a numerical method is introduced in this section, which can solve the boundary value problem (equation) effectively and accurately. Also, the shear profile can then be arbitrary. A flow chart of the numerical procedure is given in Fig. 2.5.

To calculate the second-order correction, the input parameters required are as follows:

- shear current profile,
- linear wave amplitudes,
- linear wave frequency or wavenumber,

For a given shear profile, the linear dispersion relation is implicit, which can be solved using the weak-shear approximation (Kirby and Chen 1989) or the direct numerical method (DIM) (Li and Ellingsen 2019). Here, the DIM code is adopted, which can also provide the linear velocity fields.

Then, the elevation, velocities, and pressure of the linear waves are substituted into the boundary value problem Eq. (2.13). The second-order vertical velocity $\hat{w}_{\pm}^{(2)}$ can be solved with the finite difference method or the finite volume method. Performing an inverse Fourier transform and substituting the result into (2.14) give the wave surface elevation $\zeta^{(2)}$, pressure $p^{(2)}$, and horizontal velocity vector $\mathbf{V}^{(2)}$.

2.5 Instability

The previous sections give the boundary value problem and solutions for the wave-shear current interaction. However, three types of singularities exist in the system, which are omitted in the solutions:

- triad resonance,
- a critical layer in the flow,
- Langmuir circulation.

They are introduced briefly in this section.

2.5.1 Triad resonance

The nonlinear resonant interaction between two or more monochromatic waves was proposed by Phillips (1960), which was then extended by Longuet-Higgins and Stewart (1962). This phenomenon refers to energy transfer between waves. If the following conditions are satisfied simultaneously, then the wave amplitudes cease to be constants.

$$\mathbf{k}_1 \pm \mathbf{k}_2 \pm \dots \mathbf{k}_n = 0, \quad (2.34a)$$

$$\omega_1 \pm \omega_2 \pm \dots \omega_n = 0, \quad (2.34b)$$

where, $n = 3$ and 4 refer to triad and quartet resonance, respectively. However, it is demonstrated by Phillips (1960) that such resonance cannot occur for second-order deep-water *surface gravity* waves *in the absence of a current*. That is because the above conditions cannot be satisfied at the same time given $n = 3$. Hence, in such circumstances, energy transfer occurs only at third-order waves ($n = 4$).

The triad resonance has been investigated extensively by introducing capillary waves (McGoldrick 1965), internal waves (Akylas and Kakoutas 2023, Alam 2012, Choi et al. 2021), or a shear current (Craig 1968, Drivas and Wunsch 2016, Kelly 1968). Here, this mechanism is explained by introducing a simple linear shear current.

In this case, three-dimensional waves are required. Therefore, the solutions in Section 2.2 cannot be used directly. However, the three-dimensional solutions should contain a term similar to the right-hand side of Eq. (2.20)(a). The conditions in Eq. (2.34) denote that the wavenumber and frequency of a second-order bound wave satisfy the linear dispersion relation. Using (2.17), we obtain $k_{\pm}^2 - |k_{\pm}| \omega_{\pm}^2 - k_{\pm} S \omega_{\pm} = 0$. Clearly, it demonstrates that the wave velocities and amplitude in Eq. (2.20) go to infinity due to the zero denominator. Such non-physical results are caused by improper assumptions. To solve this problem, the energy exchange should be allowed by assuming the amplitudes of wave velocities and surface vary slowly in time:

$$\begin{bmatrix} \mathbf{V}^{(1)}(\mathbf{x}, z, t) \\ \zeta^{(1)}(\mathbf{x}, t) \\ p^{(1)}(\mathbf{x}, z, t) \end{bmatrix} = \mathcal{R} \left\{ \frac{1}{4\pi^2} \int \begin{bmatrix} \hat{\mathbf{V}}^{(1)}(\mathbf{k}, t, z) \\ \hat{\zeta}^{(1)}(\mathbf{k}, t) \\ \hat{p}^{(1)}(\mathbf{k}, t, z) \end{bmatrix} e^{i\psi(\mathbf{k}, \mathbf{x}, t)} d\mathbf{k} \right\}. \quad (2.35a)$$

Solving the boundary value problem again with the above assumption, one might observe the periodic energy transfer between three waves as the work by Drivas and Wunsch (2016).

However, it is observed by Craik (1968) that triad resonance requires a fairly strong shear current. For the work by Drivas and Wunsch (2016), a discontinuous vorticity is required. Currents in the ocean or at the mouth of the river are usually weaker than that which is necessary for the triad resonance to occur. Also, this phenomenon is not observed in our numerical simulations.

2.5.2 A critical layer in the flow

A singularity of Eq. (2.14) occurs at a layer $z = z_c$ such that $\mathbf{k} \cdot \mathbf{U}(z_c) - \omega = 0$, which is called the critical layer. Here, the wavenumber and frequency can come from linear or second-order bound waves. The horizontal velocity is infinite at this layer z_c from our framework. This problem is studied extensively in the theory of hydrodynamic stability (Drazin and Reid 2004). It can be solved by introducing viscosity or using the ‘rule for going around the singularity’ (Zakharov and Shrira 1990).

Within the critical layer region, introducing viscosity could eliminate the pole of the equations. Inviscid solutions for a real flow with a high Reynolds number are still reliable if we are far from the critical layer z_c (Benney 1961). A similar phenomenon is also observed by Craik (1968) and Zakharov and Shrira (1990), even a small viscous force is dominant in the vicinity of the critical layer.

The ‘rule for going around the singularity’ concerns the wave growth in the flow of a real fluid (Zakharov and Shrira 1990). The wave motion should be solved from the Cauchy-Poisson problem. Then the waves grow slowly as a result of the wind or other forces. Under such circumstances, the wave frequency is no longer real: $\omega = \omega_r + i\omega_i$. Here, ω_r refers to the real wave frequency and ω_i denotes the growth rate of a wave, which refers to the energy exchange between the wave and the ambient environment. This idea is similar to the Miles instability for wave generation by wind (Miles 1957).

For a wave-shear current system, the growth rate of waves has been investigated with both piecewise-linear (Caponi et al. 1991) and smooth shear profiles (Morland et al. 1991). The imaginary frequency ω_i can be solved from the combined boundary condition, which is proportional to the curvature of the current $U''(z)$ (Shrira 1993, Eq. 5.3) if the shear is weak. Using complex frequency could remove this singularity at the critical layer. An extreme case considered by Craik (1968) describes the energy transfer from a shear current to the waves through the critical layer. They investigated the triad resonance in a linear shear flow and introduced the viscosity to remove the pole.

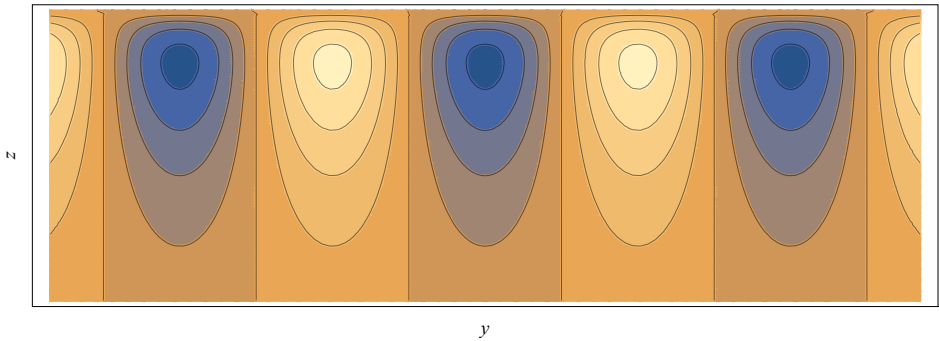


Figure 2.6: Langmuir vortex cells. Black line: streamline computed from [Akselsen and Ellingsen \(2019\)](#) (Eq. B4). Blue and orange colors refer to clockwise and anticlockwise rotations, respectively.

2.5.3 Langmuir circulation

Langmuir circulation refers to sets of vortices parallel to the shear current direction, which occurs in upper oceans and lakes ([Craig 1970](#)). The streamlines of Langmuir circulation are shown in Fig. 2.6. This phenomenon was first investigated by Langmuir in 1938. The vertical dimension of the surface wave field $\mathcal{O}(5\text{m})$ is quite modest compared to the depth of the ocean ([Sullivan and McWilliams 2010](#)). Hence, the ocean surface waves have a trivial influence on the deeper ocean. However, the Langmuir circulation, formed by the wave-shear current interaction, plays an important role in the mixing of the upper ocean ([Belcher et al. 2012](#)). A dramatic error might occur in the prediction of the dynamics of the ocean surface boundary layer if this phenomenon is ignored.

As mentioned before, Langmuir circulation is another singularity in our boundary value problem. Similarly to the critical layer problem, this pole is caused by $\mathbf{k}_- \cdot \mathbf{U} - \omega_- = 0$. But it occurs only in subharmonic waves and requires $\omega_- \equiv \omega_1 - \omega_2 = 0$ and $\mathbf{k}_- \cdot \mathbf{U} = 0$. A simple case of Langmuir circulation is achieved by two waves with $\mathbf{k}_1 = (k_{1x}, k_{1y})$ and $\mathbf{k}_2 = (k_{1x}, -k_{1y})$ and a shear current $\mathbf{U} = (U, 0)$. This condition contributes to a pole for all z below the surface rather than a specific layer. This case consists of a pair of gravity waves propagating at equal and opposite angles to the current direction. Then the subharmonic wave is steady in time and x -direction and oscillatory only in y -direction as shown in Fig. 2.6. However, the formation of Langmuir rolls does not strictly depend on such perfectly symmetric waves. A small discrepancy in angle is also allowed ([Akselsen and Ellingsen 2019](#)), which leads to deformed rolls.

A famous viscous model was proposed by [Craik and Leibovich \(1976\)](#), which is solved by large-eddy simulation and widely used in oceanography ([Belcher et al. 2012](#), [McWilliams et al. 1997](#), [Sullivan et al. 2007](#)). A simpler inviscid model proposed by [Craik \(1970\)](#) could also grasp some notable features of Langmuir circulation. In their work, the stream function $\Psi(y, z, t)$ (Eq. 3.9 in [Craik \(1970\)](#)) has a form of

$$\Psi(y, z, t) = \varphi(z, t) \exp(2ik_1y z) \quad \text{with} \quad (2.36)$$

$$\varphi(z, t) = ta_1 a_2 \frac{ik_1 y}{k_1^4} f(z). \quad (2.37)$$

The full expression of $f(z)$ is found in [Akselsen and Ellingsen \(2019\)](#) (Eq. B4). Clearly, the wave amplitude increases linearly with time.

2.5.4 Summary

To summarize, a stability analysis is beyond the scope of this thesis. Hence, the critical layer problem, Langmuir circulation, and triad resonance are excluded. If triad resonance is of interest, one may develop a pseudo-spectral method analogous to the method of [Kent and Choi \(2007\)](#).

3

Numerical cases

This chapter introduces the power energy spectra and shear currents used in the simulations. Three types of power energy spectra are used, they are

- JONSWAP spectra,
- Gaussian spectra,
- measured spectra from the mouth of the Columbia River.

Also, we adopt three types of shear current:

- linear shear currents,
- exponential shear currents,
- measured shear profiles from the mouth of the Columbia River.

The linear wave amplitudes and frequencies are generated from the wave spectra. The linear dispersion relation and the velocity fields are solved from the DIM proposed by [Li and Ellingsen \(2019\)](#). Then the second-order correction can be calculated with the theory in [Chapter 2](#) based on the linear wave solutions.

In our simulations, the waves propagate in x -direction while the current propagates at an arbitrary angle to the waves.

3.1 Power energy spectra for linear waves

The JONSWAP spectrum proposed by [Hasselmann et al. \(1973\)](#) is expressed as ([Naess and Moan 2012](#), Eq. 8.15)

$$S_J(\omega) = \frac{\tilde{\alpha}_J}{\omega^5} \exp[-1.25(\omega_p/\omega)^4] \gamma^{b_J(\omega)}, \quad (3.1)$$

where the peak enhancement factor γ appears with an exponent

$$b_J(\omega) = \exp\left[-\frac{(\omega - \omega_p)^2}{2\sigma_J^2\omega_p^2}\right], \quad (3.2)$$

and

$$\sigma_J = \begin{cases} 0.07, & \omega \leq \omega_p \\ 0.09, & \omega > \omega_p, \end{cases} \quad (3.3)$$

where ω_p is the peak frequency.

We also adopt the Gaussian spectrum, which is another commonly used spectrum. The expression is given by

$$S_G(\omega) = \tilde{\alpha}_G \exp\left[-\frac{(\omega - \omega_p)^2}{2\sigma_s^2}\right]. \quad (3.4)$$

Recall that the characteristic frequency ω_0^* is used to nondimensionalize the equations. Here, we choose $\omega_0^* \equiv \omega_p^*$ and obtain $\omega_p = 1$, which gives rise to a simpler expression for the spectrum. $\tilde{\alpha}_J$, γ , $\tilde{\alpha}_G$ and σ_s are free parameters to determine the spectrum shape, where γ and σ_s changes the width of the spectrum. The parameters $\tilde{\alpha}_J$ and $\tilde{\alpha}_G$ are chosen so that the total wave energy m_0 is a prescribed constant. m_j is the j -th moment of the spectrum, defined as

$$m_j = \int_0^\infty S(\omega)\omega^j d\omega \quad \text{with } j = 0, 1, 2, 3\dots \quad (3.5)$$

where $S(\omega)$ refers to the expression of a power energy spectrum, which can be the JONSWAP spectrum or the Gaussian spectrum.

Following [Longuet-Higgins \(1975\)](#), the bandwidth parameter is defined as

$$\nu = \sqrt{m_0 m_2 / m_1^2 - 1}, \quad (3.6)$$

which has a substantial influence on the appearance of wave surface as shown in [Fig. 1.3](#). The comparison between the two spectra is given in [Fig. 3.1](#). Apparently, the JONSWAP spectrum has a larger tail on the

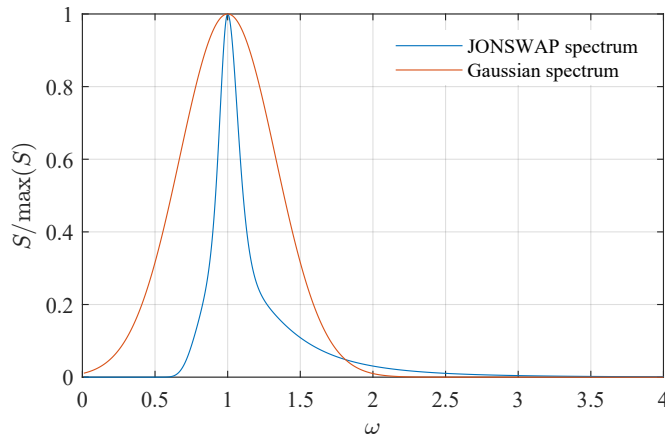


Figure 3.1: Power energy spectra with the same bandwidth ($\nu = 0.327$). $\gamma = 3.3$ is adopted in the JONSWAP spectrum.

high-frequency side, which is believed to have a substantial impact on the nonlinear properties of random waves (Tang et al. 2022).

Following Tayfun (1980) and Tucker et al. (1984), the linear wave fields are generated from the power energy spectrum $S(\omega)$. The linear wave surface is treated as a superposition of N monochromatic waves, given by

$$\zeta^{(1)} = \sum_{i=1}^N a_i \cos(\mathbf{k}_i \cdot \mathbf{x} - \omega_i t + \phi_i), \quad (3.7)$$

where $\phi_i \in [0, 2\pi)$ is the initial phase. In our simulations, the waves propagate in x -direction. We obtain $\mathbf{k} \cdot \mathbf{x} \equiv kx$. The linear amplitude is expressed as

$$a_i = \sqrt{2S(\omega_i)\Delta\omega_i}. \quad (3.8)$$

The wave spectrum is truncated at $[\omega_1, \omega_N]$ and discretized into N bands with $\Delta\omega_i$ the width of the i -th band.

It is worth noting that the generation of random waves and a focused wave group requires different amplitude a_i and phase ϕ_i .

- Random waves: as suggested by Tucker et al. (1984), a_i should be Rayleigh-distributed and ϕ_i has a uniform distribution on $[0, 2\pi)$.
- Focused wave group: ϕ_i is chosen to ensure the wave focusing happens at a prescribed location and time.

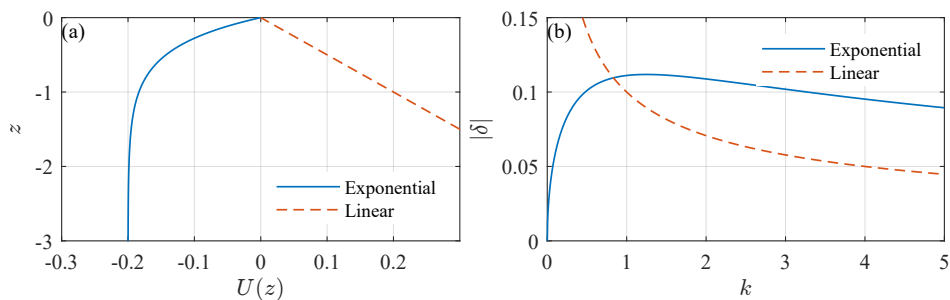


Figure 3.2: Velocity profiles $U(z)$ and shear strength δ for exponential and linear shear currents. (a) Shear profiles with $U_0 = 0.2$, $\alpha = 2.5$ and $S = -0.2$ and (b) shear strength $|\delta|$ for the two profiles in (a).

Given the linear wave fields, the second-order bound waves for each pair of linear waves are calculated from the theory in Chapter 2.

3.2 Shear current profiles

We adopt exponential and linear shear profiles, which are expressed as

$$U_{\text{exp}}(z) = U_0[\exp(\alpha z) - 1], \quad (3.9)$$

$$U_{\text{lin}}(z) = Sz, \quad (3.10)$$

respectively. α , U_0 , and S refer to the dimensionless parameters that determine the shape of the shear profiles. As mentioned above, the two-dimensional shear current is expressed as $\mathbf{U}(z) = (U(z) \cos(\theta), U(z) \sin(\theta))$ with θ the angle between the shear current and the linear waves. Example shear profiles $U(z)$ are presented in Fig. 3.2(a).

A nondimensional parameter δ was proposed by Ellingsen and Li (2017) (Eq. 12) to describe the shear strength relative to a specific monochromatic wave. It provides a quantitative description of the effect of the shear current on the dispersion relation. The expression is given by (note that the prefactor occurs because, in our nondimensional units, the phase velocity without current is $c_0 = 1/\sqrt{k}$)

$$\delta = \sqrt{k} \int_{-\infty}^0 U'(z) e^{2kz} dz. \quad (3.11)$$

The strength of two currents is given in Fig. 3.2 (b). The linear shear current gives an unrealistically large shear strength for long waves because of the infinity velocity in deep water. However, realistic currents have very little

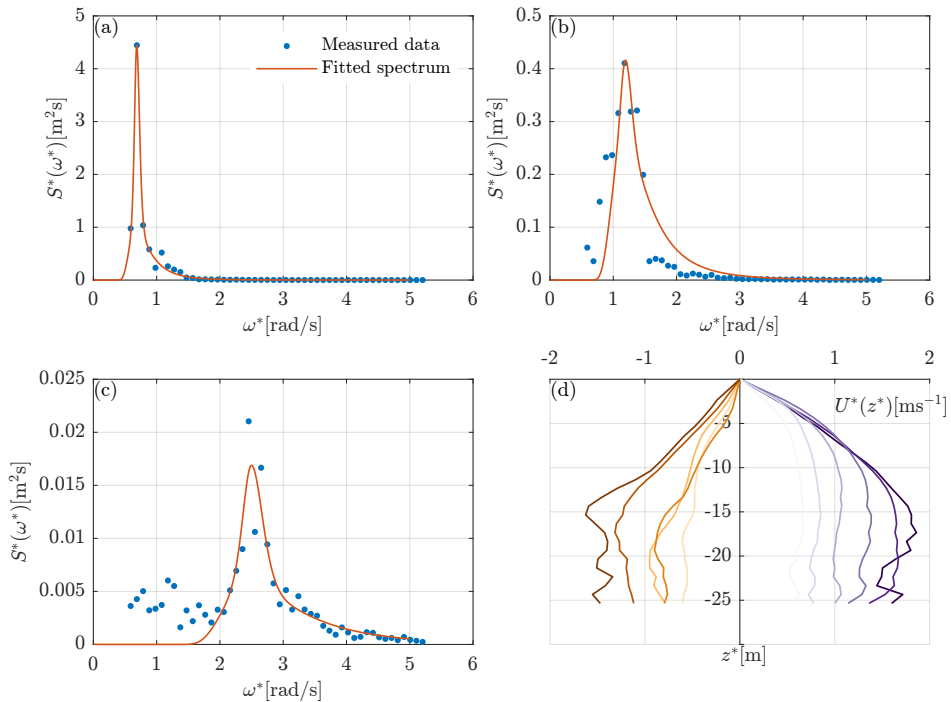


Figure 3.3: Power energy spectra and shear profiles measured at the mouth of the Columbia River by Zippel and Thomson (2017). The wave spectra in (a)–(c) are fitted with JONSWAP-type expression (3.1) with free parameters $\tilde{\alpha}_J^*$, ω_p^* and γ : (a) $\gamma = 4.87$ & $\omega_p^* = 0.69$ rad/s, (b) $\gamma = 1.62$ & $\omega_p^* = 1.19$ rad/s, and (c) $\gamma = 3.18$ & $\omega_p^* = 2.50$ rad/s. $\tilde{\alpha}_J$ depends on the prescribed wave steepness of the simulations. Its values here are not meaningful.

shear far beneath the surface. By comparison with the shear strength at the Columbia River in Fig. 3.4 (b), we will see the exponential current in this figure is not unreasonably strong.

3.3 Measured data from the Columbia River

The current at the mouth of the Columbia River has been studied extensively for its strong shear. The data measured by Zippel and Thomson (2017) and Kilcher and Nash (2010) are adopted. The wave spectra and shear current profiles measured by Zippel and Thomson (2017) are given in Fig. 3.3.

The shear profile measured by Kilcher and Nash (2010) is shown in Fig. 3.4 (a), which also includes one of the strongest shear currents by Zippel and Thomson (2017) for comparison. The maximum shear strength $|\delta|$ shown

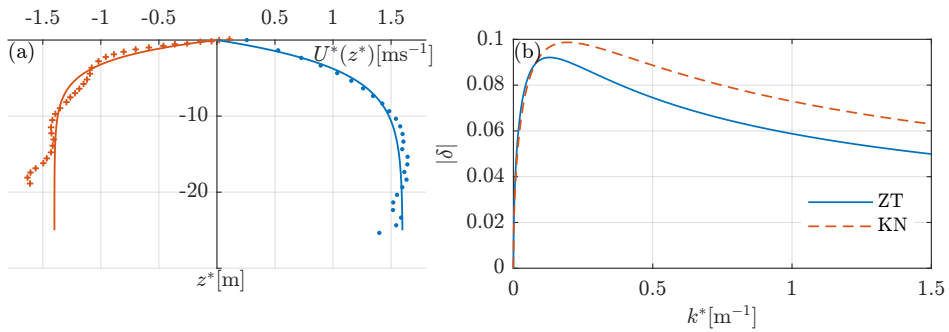


Figure 3.4: Velocity profiles and strength of the currents at the Columbia River. (a) dotted and ‘+’ lines refers to measured data, solid lines denote fitted curves with exponential function $U(z) = U_0[\exp(\alpha z) - 1]$. (b) The shear strength δ of the two fitted curves in (a) with ‘ZT’ the current from Zippel and Thomson (2017) and ‘KN’ the current from Kilcher and Nash (2010).

in Fig. 3.4 (b) is around 0.1, which suggests the exponential current in Fig. 3.2 is strong but reasonable, and may even be described as ‘weak’ in the sense that weak-shear theory may be approximately used (Ellingsen and Li 2017).

It is worth noting that a sufficient criterion for the weak-shear theory of Stewart and Joy (1974) to be accurate is that $\delta \ll 1$ (Ellingsen and Li 2017), which is satisfied for the Columbia River current even though it is often described as very strongly sheared. This fact is used to derive explicit expressions for wave surface elevation, orbital velocity, and amplification in Article II.

4

Summary of research articles and conclusions

The properties of surface gravity waves are altered by their ambient currents. This thesis aims to investigate the influence of a shear current on rogue wave events. Several physical mechanisms are possible to generate such events, but we focus only on dispersive focusing. To solve the problem, a boundary value problem is established and presented in (Article I). Then we first investigate whether the influences of different shear currents on the probability of rogue waves are substantial, which is shown in (Article I). Based on the positive answer of that paper, we then proceed and analyze the impacts of oblique shear currents on the behavior of extreme waves with linear approximation (Article II) and weakly nonlinear numerical calculations (Article III). Both the surface elevation and velocity profiles of the focused wave group are investigated.

4.1 Summary of articles

Article I

Statistics of weakly nonlinear waves on currents with strong vertical shear.

Zibo Zheng, Yan Li, Simen Å. Ellingsen

Physical Review Fluids

This work examines the effects of a shear current on the nonlinear properties of the surface gravity waves. First, we develop a weakly nonlinear theory, correct to second-order in wave steepness, which extends [Longuet-Higgins and Stewart \(1962\)](#) to allow for a depth-dependent background flow. The linear wave field is solved with the DIM method proposed by [Li and Ellingsen \(2019\)](#).

The theory is solved numerically to analyze the impacts of a shear current on wave statistics. Random wave simulations are performed with different shear currents. Based on the time record of wave surface elevation, the probability density function (PDF) of wave surface, the exceedance probability distribution (EPD) of wave crests, skewness, and expected maximum wave crest are investigated in detail.

From the simulations, the statistical properties mentioned above for linear wave fields coincide well with the theoretical expressions. The second-order correction serves as steepening the wave crests and flattening the troughs. An opposing shear strengthens the wave amplitudes while a following shear has the opposite effect. Therefore, compared to the no-current cases, the probability of rogue waves increases (decreases) significantly due to the presence of an opposing (following) shear. The skewness and expected maximum wave crest are also enhanced by an opposing shear.

In addition, analytical expressions for skewness and PDF of wave surface and EPD of crest heights are derived using the narrowband approximation following the works of several predecessors ([Fedele and Tayfun 2009](#), [Forristall 2000](#), [Longuet-Higgins 1963](#)). Such narrowband expressions show a clear departure from the broadband simulations.

Article II

Dispersive wave focusing on a shear current. Part 1: Linear approximations.

Simen Å. Ellingsen, Zibo Zheng, Malek Abid, Christian Kharif, Yan Li
Water Waves (submitted)

In this work, the dispersive focusing of linear waves altered by different shear currents is examined. Due to the complexity of the wave-shear current system, explicit solutions are usually not available even in linear order. To illustrate the impact of shear current on wave surface elevation and kinematics, we derived explicit approximate solutions with proper assumptions.

For wave surface, given a short wave group, the stationary phase method is adopted and gives accurate results compared with numerical results from the

DIM code. For a long wave group with a Gaussian envelope, we use Laplace's method to approximate the integral, which also provides an explicit solution in excellent agreement with the numerical solution.

To analyze the wave kinematics, the same approximate techniques as the wave surface are performed. Several approximate expressions with different assumptions are adopted. Due to the curvature of the shear expression, the maximum horizontal wave velocity could occur below the surface. We also derived the amplification factor of the horizontal orbital velocity due to the presence of a shear current. By performing calculations with the measured data at the mouth of the Columbia River, it is observed that the maximum horizontal velocity beneath the wave crest increases by approximately 40% for the following shear.

Article III

Dispersive wave focussing on a shear current. Part 2: effect of weak non-linearity.

Zibo Zheng, Yan Li, Simen Å. Ellingsen

Water Waves (in preparation)

This article is an extension of Article I and II. Using the theory developed in Article I, we study the dispersive focusing of weakly nonlinear wave groups and their dependence on the shear profiles. The long-crested wave groups are presumed to propagate obliquely to a shear flow. Similar to Article II, the wave surface elevation and kinematics are investigated.

The results demonstrate that even a strong shear current has a trivial influence on the surface elevation of a focused wave group. However, the horizontal orbital velocity beneath the crest differs dramatically from when no shear is present. The influence of different shear currents on the velocity profiles of second-order bound waves is even stronger than those of linear waves. The horizontal velocity of superharmonic and subharmonic waves can be positive or negative, which depends on the relative direction of the wave group and shear current. Considering a narrowband wave spectrum, the velocity of subharmonic waves does not vanish as it does without shear; it reduces to a nontrivial change in the shear current instead.

4.2 Future work

Following the work in this study, several topics could merit investigation in the future. These include:

1. **Triad resonance:** The current theory can not address triad resonance. It is well known that the quartet resonance causes energy redistribution at third order, which alters the wave spectrum and surface elevation substantially. Hence, we infer that the triad resonance due to shear current might have similar effects and cause even stronger energy redistribution. This topic is also an extension of [Zakharov and Shrira \(1990\)](#).
2. **Third-order theory:** The nonlinearity of ocean waves is not necessarily weak. To describe the waves in the ocean, third-order corrections need to be included. If the triad resonance in Point 1 is solved. Developing third-order theory should be straightforward, although work intensive.
3. **Highest wave:** It has been shown by Stokes ([Lamb 1932](#), Section 250) that the highest wave in steady motion has a sharp angle of 120° at the crest. The shear current might have an impact on this phenomenon.

Bibliography

- A. J. Abdullah. Wave motion at the surface of a current which has an exponential distribution of vorticity. *Annals of the New York Academy of Sciences*, 51(3):425–441, 1949.
- T. A. A. Adcock and P. H. Taylor. The physics of anomalous (‘rogue’) ocean waves. *Reports on Progress in Physics*, 77(10):105901, 2014.
- T. A. A. Adcock, P. H. Taylor, S. Yan, Q. W. Ma, and P. A. E. M. Janssen. Did the Draupner wave occur in a crossing sea? *Proceedings of the Royal Society A: Mathematical, Physical and Engineering Sciences*, 467(2134):3004–3021, 2011.
- A. H. Akselsen and S. Å. Ellingsen. Weakly nonlinear transient waves on a shear current: Ring waves and skewed Langmuir rolls. *Journal of Fluid Mechanics*, 863:114–149, 2019.
- T. R. Akylas and C. Kakoutas. Stability of internal gravity wave modes: from triad resonance to broadband instability. *Journal of Fluid Mechanics*, 961:A22, 2023.
- M.-R. Alam. A new triad resonance between co-propagating surface and interfacial waves. *Journal of Fluid Mechanics*, 691:267–278, 2012.
- S. Y. Annenkov and V. I. Shrira. Role of non-resonant interactions in the evolution of nonlinear random water wave fields. *Journal of Fluid Mechanics*, 561:181–207, 2006.
- A. I. Baumstein. Modulation of gravity waves with shear in water. *Studies in Applied Mathematics*, 100(4):365–390, 1998.
- S. E. Belcher, A. L. M. Grant, K. E. Hanley, B. Fox-Kemper, L. Van Roekel, P. P. Sullivan, W. G. Large, A. Brown, A. Hines, D. Calvert, A. Rutgersson, H. Pettersson, J.-R. Bidlot, P. A. E. M. Janssen, and J. A. Polton. A global perspective on Langmuir turbulence in the ocean surface boundary layer. *Geophysical Research Letters*, 39(18), 2012.

- C. Bender and S. Orszag. *Advanced Mathematical Methods for Scientists and Engineers I: Asymptotic Methods and Perturbation Theory*. Springer New York, 2013.
- T. B. Benjamin and J. E. Feir. The disintegration of wave trains on deep water part 1. theory. *Journal of Fluid Mechanics*, 27(3):417–430, 1967.
- D. J. Benney. A non-linear theory for oscillations in a parallel flow. *Journal of Fluid Mechanics*, 10(2):209–236, 1961.
- C. T. Bolles, K. Speer, and M. N. J. Moore. Anomalous wave statistics induced by abrupt depth change. *Physical Review Fluids*, 4(1):011801, 2019.
- L. Brekhovskikh. *Waves in layered media*, volume 16. Elsevier, 2012.
- I. Brevik. Higher-order waves propagating on constant vorticity currents in deep water. *Coastal Engineering*, 2:237–259, 1978.
- E. A. Caponi, H. C. Yuen, F. A. Milinazzo, and P. G. Saffman. Water-wave instability induced by a drift layer. *Journal of Fluid Mechanics*, 222: 207–213, 1991.
- W. Choi, M. Chabane, and T. M. A. Taklo. Two-dimensional resonant triad interactions in a two-layer system. *Journal of Fluid Mechanics*, 907:A5, 2021.
- A. Constantin, R. I. Ivanov, and E. M. Prodanov. Nearly-Hamiltonian structure for water waves with constant vorticity. *Journal of Mathematical Fluid Mechanics*, 10(2):224–237, 2008.
- A. D. D. Craik. Resonant gravity-wave interactions in a shear flow. *Journal of Fluid Mechanics*, 34(3):531–549, 1968.
- A. D. D. Craik. A wave-interaction model for the generation of windrows. *Journal of Fluid Mechanics*, 41(4):801–821, 1970.
- A. D. D. Craik and S. Leibovich. A rational model for Langmuir circulations. *Journal of Fluid Mechanics*, 73(3):401–426, 1976.
- R. Dalrymple. Water wave models and wave forces with shear currents. Report, University of Florida, 1973.
- R. A. Dalrymple. A finite amplitude wave on a linear shear current. *Journal of Geophysical Research*, 79:4498–4504, 1974.

-
- J. F. Dalzell. A note on finite depth second-order wave–wave interactions. *Applied Ocean Research*, 21(3):105–111, 1999.
- R. Dean and R. Dalrymple. *Water Wave Mechanics for Engineers and Scientists*. World Scientific, 1991.
- E. Didenkulova, I. Didenkulova, and I. Medvedev. Freak wave events in 2005–2021: statistics and analysis of favourable wave and wind conditions. *Nat. Hazards Earth Syst. Sci.*, 23(4):1653–1663, 2023.
- M. A. Donelan and A.-K. Magnusson. The making of the Andrea wave and other rogues. *Scientific Reports*, 7(1):44124, 2017.
- P. G. Drazin and W. H. Reid. *Hydrodynamic Stability*. Cambridge Mathematical Library. Cambridge University Press, Cambridge, 2nd edition, 2004.
- T. D. Drivas and S. Wunsch. Triad resonance between gravity and vorticity waves in vertical shear. *Ocean Modelling*, 103:87–97, 2016.
- K. Dysthe and K. Trulsen. Note on breather type solutions of the nls as models for freak-waves. *Physica Scripta*, T82:48, 1999.
- K. Dysthe, H. E. Krogstad, and P. Müller. Oceanic rogue waves. *Annual Review of Fluid Mechanics*, 40:287–310, 2008.
- K. B. Dysthe, K. Trulsen, H. E. Krogstad, and H. Socquet-Juglard. Evolution of a narrow-band spectrum of random surface gravity waves. *Journal of Fluid Mechanics*, 478:1–10, 2003.
- S. Å. Ellingsen. Ship waves in the presence of uniform vorticity. *Journal of Fluid Mechanics*, 742:R2, 2014.
- S. Å. Ellingsen. Oblique waves on a vertically sheared current are rotational. *European Journal of Mechanics - B/Fluids*, 56:156–160, 2016.
- S. Å. Ellingsen and I. Brevik. How linear surface waves are affected by a current with constant vorticity. *European Journal of Physics*, 35, 2013.
- S. Å. Ellingsen and Y. Li. Approximate dispersion relations for waves on arbitrary shear flows. *Journal of Geophysical Research: Oceans*, 122(12): 9889–9905, 2017.
- F. Fedele and M. A. Tayfun. On nonlinear wave groups and crest statistics. *Journal of Fluid Mechanics*, 620:221–239, 2009.

- F. Fedele, J. Brennan, S. Ponce de León, J. Dudley, and F. Dias. Real world ocean rogue waves explained without the modulational instability. *Scientific Reports*, 6(1):27715, 2016.
- J. D. Fenton. Some results for surface gravity waves on shear flows. *IMA Journal of Applied Mathematics*, 12(1):1–20, 1973.
- J. D. Fenton. A fifth-order Stokes theory for steady waves. *Journal of Waterway, Port, Coastal, and Ocean Engineering*, 111(2):216–234, 1985.
- G. Z. Forristall. Wave crest distributions: Observations and second-order theory. *Journal of Physical Oceanography*, 30(8):1931–1943, 2000.
- M. Francius and C. Kharif. Two-dimensional stability of finite-amplitude gravity waves on water of finite depth with constant vorticity. *Journal of Fluid Mechanics*, 830:631–659, 2017.
- W. Fujimoto, T. Waseda, and A. Webb. Impact of the four-wave quasi-resonance on freak wave shapes in the ocean. *Ocean Dynamics*, 69(1):101–121, 2019.
- R. H. Gibbs and P. H. Taylor. Formation of walls of water in ‘fully’ nonlinear simulations. *Applied Ocean Research*, 27(3):142–157, 2005.
- F. I. Gonazález. A case study of wave–current–bathymetry interactions at the Columbia River entrance. *Journal of Physical Oceanography*, 14(6):1065–1078, 1984.
- F. I. González, M. R. Mulhern, E. D. Cokelet, and T. C. Kaiser. Wave and current observations at the Columbia River entrance. Report, Pacific Marine Environmental Laboratory, 1981.
- O. Gramstad and K. Trulsen. Influence of crest and group length on the occurrence of freak waves. *Journal of Fluid Mechanics*, 582:463–472, 2007.
- K. Hasselmann. On the non-linear energy transfer in a gravity-wave spectrum part 1. general theory. *Journal of Fluid Mechanics*, 12(4):481–500, 1962.
- K. Hasselmann, T. Barnett, E. Bouws, H. Carlson, D. Cartwright, K. Enke, J. Ewing, H. Gienapp, D. Hasselmann, P. Kruseman, A. Meerburg, P. Müller, D. Olbers, K. Richter, W. Sell, and H. Walden. Measurements of wind-wave growth and swell decay during the joint north sea wave project (JONSWAP). *Deut. Hydrogr. Z.*, 8:1–95, 1973.

-
- S. Hayer and O. Andersen. Freak waves: Rare realizations of a typical population or typical realizations of a rare population? 2000.
- K. L. Henderson, D. H. Peregrine, and J. W. Dold. Unsteady water wave modulations: fully nonlinear solutions and comparison with the nonlinear schrödinger equation. *Wave Motion*, 29(4):341–361, 1999.
- H.-C. Hsu, M. Francius, P. Montalvo, and C. Kharif. Gravity-capillary waves in finite depth on flows of constant vorticity. *Proceedings of the Royal Society A: Mathematical, Physical and Engineering Sciences*, 472(2195):20160363, 2016.
- P. A. E. M. Janssen. Nonlinear four-wave interactions and freak waves. *Journal of Physical Oceanography*, 33(4):863–884, 2003.
- R. E. Kelly. On the resonant interaction of neutral disturbances in two inviscid shear flows. *Journal of Fluid Mechanics*, 31(4):789–799, 1968.
- C. P. Kent and W. Choi. An explicit formulation for the evolution of nonlinear surface waves interacting with a submerged body. *International Journal for Numerical Methods in Fluids*, 55(11):1019–1038, 2007.
- C. Kharif and E. Pelinovsky. Physical mechanisms of the rogue wave phenomenon. *European Journal of Mechanics - B/Fluids*, 22(6):603–634, 2003.
- C. Kharif, E. Pelinovsky, and A. Slunyaev. *Rogue waves in the ocean*. Springer Science & Business Media, 2008.
- L. F. Kilcher and J. D. Nash. Structure and dynamics of the Columbia River tidal plume front. *Journal of Geophysical Research: Oceans*, 115(C5), 2010.
- J. T. Kirby and T.-M. Chen. Surface waves on vertically sheared flows: Approximate dispersion relations. *Journal of Geophysical Research*, 94:1013, 1989.
- M. Klahn, P. A. Madsen, and D. R. Fuhrman. On the statistical properties of surface elevation, velocities and accelerations in multi-directional irregular water waves. *Journal of Fluid Mechanics*, 910:A23, 2021.
- H. Lamb. *Hydrodynamics*. Dover Publications, New York, 6th edition, 1932.
- I. V. Lavrenov. The wave energy concentration at the Agulhas current off south africa. *Natural Hazards*, 17(2):117–127, 1998.

- C. Lawrence, K. Trulsen, and O. Gramstad. Extreme wave statistics of surface elevation and velocity field of gravity waves over a two-dimensional bathymetry. *Journal of Fluid Mechanics*, 939:A41, 2022.
- Y. Li and S. Å. Ellingsen. A framework for modeling linear surface waves on shear currents in slowly varying waters. *Journal of Geophysical Research: Oceans*, 124(4):2527–2545, 2019.
- Y. Li, S. Draycott, Y. Zheng, Z. Lin, T. A. A. Adcock, and T. S. van den Bremer. Why rogue waves occur atop abrupt depth transitions. *Journal of Fluid Mechanics*, 919:R5, 2021.
- M. Lighthill. On the critical Froude number for turbulent flow over a smooth bottom. In *Proc. Cambridge Phil. Soc.*, volume 49, pages 704–706, 1953.
- P. Liu. A chronology of freak wave encounters. *Geofizika*, 24(1), 2007.
- M. S. Longuet-Higgins. On the statistical distribution of the heights of sea waves. *Journal of Marine Research*, 11(3):245–266, 1952.
- M. S. Longuet-Higgins. The effect of non-linearities on statistical distributions in the theory of sea waves. *Journal of Fluid Mechanics*, 17(3):459–480, 1963.
- M. S. Longuet-Higgins. On the joint distribution of the periods and amplitudes of sea waves. *Journal of Geophysical Research (1896-1977)*, 80(18):2688–2694, 1975.
- M. S. Longuet-Higgins and R. W. Stewart. Radiation stress and mass transport in gravity waves, with application to ‘surf beats’. *Journal of Fluid Mechanics*, 13(4):481–504, 1962.
- L. F. McGoldrick. Resonant interactions among capillary-gravity waves. *Journal of Fluid Mechanics*, 21(2):305–331, 1965.
- J. C. McWilliams, P. P. Sullivan, and C.-H. Moeng. Langmuir turbulence in the ocean. *Journal of Fluid Mechanics*, 334:1–30, 1997.
- C. C. Mei, M. Stiassnie, and D. K.-P. Yue. *Theory and Applications of Ocean Surface Waves*. Theory and Applications of Ocean Surface Waves. 2005.
- S. Mendes and J. Kasparian. Saturation of rogue wave amplification over steep shoals. *Physical Review E*, 106(6):065101, 2022.

-
- S. Mendes and J. Kasparian. Non-homogeneous approximation for the kurtosis evolution of shoaling rogue waves. *Journal of Fluid Mechanics*, 966: A42, 2023.
- J. W. Miles. On the generation of surface waves by shear flows. *Journal of Fluid Mechanics*, 3(2):185–204, 1957.
- L. C. Morland and P. G. Saffman. Effect of wind profile on the instability of wind blowing over water. *Journal of Fluid Mechanics*, 252:383–398, 1993.
- L. C. Morland, P. G. Saffman, and H. C. Yuen. Waves generated by shear layer instabilities. *Proceedings: Mathematical and Physical Sciences*, 433 (1888):441–450, 1991.
- A. Naess and T. Moan. *Stochastic Dynamics of Marine Structures*. Cambridge University Press, Cambridge, 2012.
- M. Onorato, A. R. Osborne, M. Serio, and S. Bertone. Freak waves in random oceanic sea states. *Physical Review Letters*, 86(25):5831–5834, 2001.
- M. Onorato, A. Osborne, and M. Serio. On deviations from gaussian statistics for surface gravity waves. *arXiv: Chaotic Dynamics*, 2005.
- D. H. Peregrine. *Interaction of Water Waves and Currents*, volume 16, pages 9–117. Elsevier, 1976.
- O. M. Phillips. On the dynamics of unsteady gravity waves of finite amplitude part 1. the elementary interactions. *Journal of Fluid Mechanics*, 9 (2):193–217, 1960.
- N. Pizzo, L. Lenain, O. Rømcke, S. Å. Ellingsen, and B. K. Smeltzer. The role of Lagrangian drift in the geometry, kinematics and dynamics of surface waves. *Journal of Fluid Mechanics*, 954:R4, 2023.
- V. I. Shrira. Surface waves on shear currents: solution of the boundary-value problem. *Journal of Fluid Mechanics*, 252:565–584, 1993.
- V. I. Shrira and A. V. Slunyaev. Trapped waves on jet currents: asymptotic modal approach. *Journal of Fluid Mechanics*, 738:65–104, 2014.
- L. Skjelbreia and J. Hendrickson. Fifth order gravity wave theory. *Coastal Engineering Proceedings*, 1(7):10, 1960.
- A. Slunyaev, I. Didenkulova, and E. Pelinovsky. Rogue waters. *Contemporary Physics*, 52(6):571–590, 2011.

- B. K. Smeltzer and S. Å. Ellingsen. Surface waves on currents with arbitrary vertical shear. *Physics of Fluids*, 29(4):047102, 2017.
- H. Socquet-Juglard, K. Dysthe, K. Trulsen, H. E. Krogstad, and J. Liu. Probability distributions of surface gravity waves during spectral changes. *Journal of Fluid Mechanics*, 542:195–216, 2005.
- M. A. Srokosz. A new statistical distribution for the surface elevation of weakly nonlinear water waves. *Journal of Physical Oceanography*, 28(1):149–155, 1998.
- J. N. Steer, A. G. L. Borthwick, D. Stagonas, E. Buldakov, and T. S. v. d. Bremer. Experimental study of dispersion and modulational instability of surface gravity waves on constant vorticity currents. *Journal of Fluid Mechanics*, 884:A40, 2020.
- R. H. Stewart and J. W. Joy. Hf radio measurements of surface currents. *Deep Sea Research and Oceanographic Abstracts*, 21(12):1039–1049, 1974.
- G. G. Stokes. On the theory of oscillatory waves. *Trans. Cam. Philos. Soc.*, 8:441–455, 1847.
- P. P. Sullivan and J. C. McWilliams. Dynamics of winds and currents coupled to surface waves. *Annual Review of Fluid Mechanics*, 42(1):19–42, 2010.
- P. P. Sullivan, J. C. McWilliams, and W. K. Melville. Surface gravity wave effects in the oceanic boundary layer: large-eddy simulation with vortex force and stochastic breakers. *Journal of Fluid Mechanics*, 593:405–452, 2007.
- T. Tang, D. Barratt, H. B. Bingham, T. S. van den Bremer, and T. A. A. Adcock. The impact of removing the high-frequency spectral tail on rogue wave statistics. *Journal of Fluid Mechanics*, 953:A9, 2022.
- M. A. Tayfun. Narrow-band nonlinear sea waves. *Journal of Geophysical Research*, 85:1548, 1980.
- M. A. Tayfun and F. Fedele. Wave-height distributions and nonlinear effects. *Ocean Engineering*, 34(11):1631–1649, 2007.
- A. F. Teles Da Silva and D. H. Peregrine. Steep, steady surface waves on water of finite depth with constant vorticity. *Journal of Fluid Mechanics*, 195:281–302, 1988.

-
- R. Thomas, C. Kharif, and M. Manna. A nonlinear schrödinger equation for water waves on finite depth with constant vorticity. *Physics of Fluids*, 24(12), 2012.
- P. D. Thompson. The propagation of small surface disturbances through rotational flow. *Annals of the New York Academy of Sciences*, 51(3): 463–474, 1949.
- A. Toffoli, M. Benoit, M. Onorato, and E. M. Bitner-Gregersen. The effect of third-order nonlinearity on statistical properties of random directional waves in finite depth. *Nonlin. Processes Geophys.*, 16(1):131–139, 2009.
- A. Toffoli, T. Waseda, H. Houtani, L. Cavaleri, D. Greaves, and M. Onorato. Rogue waves in opposing currents: an experimental study on deterministic and stochastic wave trains. *Journal of Fluid Mechanics*, 769:277–297, 2015.
- K. Trulsen, H. Zeng, and O. Gramstad. Laboratory evidence of freak waves provoked by non-uniform bathymetry. *Physics of Fluids*, 24(9):097101, 2012.
- K. Trulsen, A. Raustøl, S. Jorde, and L. B. Rye. Extreme wave statistics of long-crested irregular waves over a shoal. *Journal of Fluid Mechanics*, 882:R2, 2020.
- M. J. Tucker, P. G. Challenor, and D. J. T. Carter. Numerical simulation of a random sea: a common error and its effect upon wave group statistics. *Applied Ocean Research*, 6(2):118–122, 1984.
- W. Xiao, Y. Liu, G. Wu, and D. K. P. Yue. Rogue wave occurrence and dynamics by direct simulations of nonlinear wave-field evolution. *Journal of Fluid Mechanics*, 720:357–392, 2013.
- Z. Xin, X. Li, and Y. Li. Coupled effects of wave and depth-dependent current interaction on loads on a bottom-fixed vertical slender cylinder. *Coastal Engineering*, page 104304, 2023.
- W. R. Young and C. L. Wolfe. Generation of surface waves by shear-flow instability. *Journal of Fluid Mechanics*, 739:276–307, 2014.
- V. E. Zakharov. Stability of periodic waves of finite amplitude on the surface of a deep fluid. *Journal of Applied Mechanics and Technical Physics*, 9(2):190–194, 1968.

- V. E. Zakharov and V. I. Shrira. Formation of the angular spectrum of wind waves. *Soviet physics, JETP*, 71:1091–1100, 1990.
- X. Zhang. Short surface waves on surface shear. *Journal of Fluid Mechanics*, 541:345–370, 2005.
- Y. Zheng, Z. Lin, Y. Li, T. A. A. Adcock, Y. Li, and T. S. van den Bremer. Fully nonlinear simulations of unidirectional extreme waves provoked by strong depth transitions: The effect of slope. *Physical Review Fluids*, 5(6):064804, 2020.
- Z. Zheng, Y. Li, and S. Å. Ellingsen. Statistics of weakly nonlinear waves on currents with strong vertical shear. *Physical Review Fluids*, 8(1):014801, 2023.
- S. Zippel and J. Thomson. Surface wave breaking over sheared currents: Observations from the mouth of the Columbia River. *Journal of Geophysical Research: Oceans*, 122, 2017.

Research articles in full text




Article I

**Statistics of weakly nonlinear waves on currents with
strong vertical shear**

Zibo Zheng, Yan Li, Simen Å. Ellingsen

*Published in: Physical Review Fluids, Volume 8, Issue 1,
Page 014801*

Statistics of weakly nonlinear waves on currents with strong vertical shear

Zibo Zheng ^{1,*}, Yan Li ^{1,2,†} and Simen Å. Ellingsen ^{1,‡}

¹*Department of Energy and Process Engineering, Norwegian University of Science and Technology, N-7491 Trondheim, Norway*

²*Department of Mathematics, University of Bergen, N-5020 Bergen, Norway*



(Received 28 March 2022; accepted 14 December 2022; published 13 January 2023)

We investigate how the presence of a vertically sheared current affects wave statistics, including the probability of rogue waves, and apply it to a real-world case using measured spectral and shear current data from the mouth of the Columbia River. A theory for weakly nonlinear waves valid to second order in wave steepness is derived and used to analyze statistical properties of surface waves; the theory extends the classic theory by Longuet-Higgins [*J. Fluid Mech.* **12**, 321 (1962)] to allow for an arbitrary depth-dependent background flow, $U(z)$, with U the horizontal velocity along the main direction of wave propagation and z the vertical axis. Numerical statistics are collected from a large number of realizations of random, irregular sea-states following a JONSWAP spectrum, on linear and exponential model currents of varying strengths. A number of statistical quantities are presented and compared to a range of theoretical expressions from the literature; in particular the distribution of wave surface elevation, surface maxima, and crest height; the exceedance probability including the probability of rogue waves; the maximum crest height among N_s waves, and the skewness of the surface elevation distribution. We find that compared to no-shear conditions, opposing vertical shear [$U'(z) > 0$] leads to increased wave height and increased skewness of the nonlinear-wave elevation distribution, while a following shear [$U'(z) < 0$] has opposite effects. With the wave spectrum and velocity profile measured in the Columbia River estuary by Zippel and Thomson [*J. Geophys. Res.: Oceans* **122**, 3311 (2017)] our second-order theory predicts that the probability of rogue waves is significantly reduced and enhanced during ebb and flood, respectively, adding support to the notion that shear currents need to be accounted for in wave modeling and prediction.

DOI: [10.1103/PhysRevFluids.8.014801](https://doi.org/10.1103/PhysRevFluids.8.014801)

I. INTRODUCTION

Waves in the ocean are almost invariably affected by interaction with their surroundings, ambient currents in particular. While large-scale ocean currents may be approximately depth-independent, this is often not the case for smaller-scale currents such as those driven by wind shear, or currents in the near-shore environment including river deltas and tidal currents. Of particular interest is the role of these environmental factors on the occurrence probability of extremely large waves [1–3], known also as rogue, giant, or freak waves, defined as waves whose amplitude far exceeds that of their surrounding wave field. To this end, many formation mechanisms of rogue waves have been proposed, including (but not limited to) dispersive focusing of linear waves [1], nonlinear effects

*zibo.zheng@ntnu.no

†Corresponding author: yan.li@uib.no

‡simen.a.ellingsen@ntnu.no

such as the modulational instability [4] and quartet resonances [5] as well as refraction by currents [6] and bathymetry [7,8], and nonlinear interaction between surface waves and depth transitions [9,10]. In this paper, our main attention is paid to the effect of a background depth-varying current on the statistics of weakly nonlinear waves, rogue wave events in particular.

To obtain a proper statistical description of rogue wave events, a theory for second-order interaction of waves in a random sea has been widely used in both analytical [11–18] and numerical studies [19,20]. In contrast to linear waves in a random sea for which the wave elevation can be represented as a Gaussian random process [21], second-order nonlinear waves can lead to considerable deviations from Gaussian wave statistics due to the steepened crests and flattened troughs caused by second-order (bound) waves. To describe the altered statistics, analytical models for wave crest and elevation distributions have been proposed for deep-water random waves, see, e.g., Refs. [13,15,17]. These generally agree well with both laboratory and field measurements for narrowband and broadband wave fields (see, e.g., Refs. [17,20,22–24]) with moderate steepness. In more nonlinear sea states discrepancies arise from third and higher order nonlinear effects, e.g., the well-known Benjamin-Feir instability [4] and the resonant wave quartets [5]. Hence, a second-order theory such as the one we present herein, is limited to the cases where higher-order corrections are comparatively small.

Many studies have suggested several different ways by which the probability of rogue waves is increased in the presence of currents with horizontal, but not vertical, spatial variation (cf. Refs. [25,26]). A current whose magnitude and direction varies slowly in space relative to the rapidly varying wave phase has mostly been considered as a (local) Doppler shift on the wave dispersion relation and as a medium of refraction in the conservation of wave action [6,27]. Due to this, White and Fornberg [6] attribute the enhanced probability of larger wave events in currents to the local refraction by currents. Many varieties of the third-order nonlinear Schrödinger equations have been developed for slowly (horizontally) varying currents, see, e.g., Refs. [28–30]. An opposing current has been found to lead to strengthened modulational instability [7,31], and Shrira and Slunyaev [26] found that trapped waves by a jet current can also lead to an enhanced formation probability of rogue waves, while Hjelmervik and Trulsen [30] found that a wave impinging on an opposing jet has increased significant wave height, but decreased kurtosis, and viceversa.

The aforementioned works have focused on a current whose velocity profile does not have significant gradients in the vertical direction. Among the studies of waves in a horizontally uniform and depth varying current, a majority have examined waves propagating along or against currents which vary linearly with depth, which in two dimensions permits the use of a velocity potential [32], considerably simplifying the analytical treatment [29,33–37]. The assumption of a linearly varying current also results in significant simplification of the continuity and Euler momentum equations in three dimensions, based on which a second-order theory for three-dimensional waves was developed by Akselsen and Ellingsen [38]. A uniform vorticity plays a significant role in both the sideband instability and modulational growth rate for weakly nonlinear unidirectional Stokes waves [34,39]. A positive vorticity, which in the earth-fixed reference system corresponds to an opposing current getting weaker with increasing depth—i.e., $U(z) < 0$ and $U'(z) < 0$ with $U(z)$ the current oriented along the wave propagation direction, z the vertical coordinate, and a prime denotes the derivative—can remove the modulational instability altogether. The effect was demonstrated experimentally by Steer et al. [40] and Pizzo et al. [41] (the definition of positive/negative shear in Ref. [40] is different from ours due to a different choice of the coordinate system). Francius and Kharif [42] have extended [34] to two-dimensional Stokes waves where new quartet and quintet instabilities have been discovered arising from the presence of a uniform vorticity, while Abrashkin and Pelinovsky [43] derived a nonlinear Schrödinger equation for arbitrary, weak vertical shear in a Lagrangian framework, generalized in Ref. [41].

Realistic natural currents have nonzero curvature in the depth direction which leads to additional effects on wave properties. A number of works, e.g., Refs. [44–48], have demonstrated the importance of the depth-varying curvature of a current profile in the wave action equation. Effects of the curvature are wave-number- and depth-dependent, leading to considerable deviations of the

direction and speed of the propagation of wave energy from the cases where the curvature has been neglected [48]. Experimental studies, e.g., Refs. [49–51], have confirmed the importance of curvature in wave modeling. Cummins and Swan [49] carried out an experimental study of irregular waves propagating in an arbitrarily depth varying current and the wave spectra measured showed significant differences from those in a uniform and magnitude-equivalent current. It was concluded by Waseda *et al.* [50] from experiments that the variability of the ambient current affected the third-order resonant interaction of wave quartets more than its mean profile did. In field observations, ocean currents are found to have considerable effect on the significant wave height [52], estimation of Stokes drift and particle trajectories [53], and the dissipation of waves through breaking [54].

The objective of the paper is twofold. First, we present a new framework to allow for the interaction of weakly nonlinear surface gravity waves and a vertically sheared current, generalizing the work of Longuet-Higgins [11]. Second, we implement the new theory numerically to study how a current profile's shear and curvature affect wave statistics, e.g., wave crest distribution and skewness of the surface elevation of random waves.

We highlight that the new framework presented in this paper does not rely on assumptions of weak vertical shear (such as Stewart and Joy [55], Skop [56], Kirby and Chen [57], Zakharov and Shrira [58]) or weak curvature (or “near-potentiality,” e.g., Shrira [59] and Ellingsen and Li [60]). Although these simplifying assumptions may be applicable to most realistic situations in the open ocean, their validity should not be taken for granted, and must be properly ascertained [60]. Indeed, the shear of a current can be strong in oceanic and coastal waters. For example, a wind-driven shear current in the top few centimetres can have very strong shear (e.g., Refs. [61,62]) and the surface current typically takes values $\sim 3\%$ of the wind speed [63]. Estuarine tidal flow has been found to be very strongly sheared, for instance the mouth of the Columbia River which we use as example herein [54,64]. We therefore choose to use the numerical direct integration method (DIM) proposed by Li and Ellingsen [47] to calculate the linear wave surface and velocity fields, being equally applicable to any horizontally uniform depth-dependent current profile regardless of its magnitude, shear, and curvature. As detailed in Li and Ellingsen [47], the computational cost of the DIM is comparable to that using analytical approximations which involve integration over the water column [55–57,60], and unlike the aforementioned approximations, it provides an error estimate at little extra cost. The computer code used to generate the results presented in this paper is included as Supplemental Material online [65].

This paper is laid out as follows. A second-order theory based on a perturbation expansion, the direct integration method for linear waves [47], and double Fourier integrals for the second-order bound waves is presented in Sec. II. Using the assumption of narrow-banded waves the shear current-modified wave statistics (e.g., skewness and the exceedance probability of wave crest) are derived in Sec. III. With the numerical implementation of the theory detailed in Sec. IV, weakly nonlinear waves in a random sea are examined in Sec. V, for which the linear wave amplitude and phase used for random wave realizations are assumed to follow a Rayleigh distribution and a uniform distribution, respectively, following Tucker *et al.* [66].

II. THEORETICAL DESCRIPTION AND METHODOLOGY

A. Problem statement

We consider three-dimensional surface gravity waves atop a background flow in deep water. Incompressible and inviscid fluids are assumed and the surface tension has been neglected for simplicity. The background flow propagates in the horizontal plane and varies with depth (i.e., vertically sheared). Its three-dimensional velocity vector is described by $\mathbf{U}_3^*(z^*) = (\mathbf{U}^*(z^*), 0)$, with \mathbf{U}^* the velocity vector in the horizontal plane, z^* the upward axis, and a vanishing vertical component. Dimensional variables are marked with an asterisk. A Cartesian coordinate system is chosen and the still water surface in the absence of waves and flow is located at $z^* = 0$. The surface

elevation due to the background flow in the absence of surface waves is described by $z^* = \eta^*$, which is assumed known and whose spatial and temporal variations are comparably negligible to the wave perturbed fields. Neglecting the influence of surface waves on the background flow field, the system of surface waves in a background flow can be described by the continuity and Euler momentum equations as follows (see, e.g., Ref. [27]):

$$\nabla_3^* \cdot \mathbf{V}_3^* = 0, \quad (1)$$

$$\partial_{t^*} \mathbf{V}_3^* + (\mathbf{V}_3^* \cdot \nabla_3^*) \mathbf{U}_3^* + (\mathbf{U}_3^* \cdot \nabla_3^*) \mathbf{V}_3^* + \nabla_3^* (P^*/\rho + gz^*) = -(\mathbf{V}_3^* \cdot \nabla_3^*) \mathbf{V}_3^*, \quad (2)$$

for $-\infty < z^* < \zeta^* + \eta^*$. Here $\nabla_3^* = (\nabla^*, \partial_{z^*})$ denotes the gradient operator in three dimensions and $\nabla^* = (\partial_{x^*}, \partial_{y^*})$ the gradient in the horizontal plane; $\mathbf{V}_3^* = (\mathbf{u}^*, w^*)$ denotes the velocity field due to surface waves in the presence of the background flow, with \mathbf{u}^* and w^* the velocity vector in the horizontal plane and vertical component, respectively, \mathbf{x}^* the position vector in the horizontal plane, and t^* is time; P^* denotes the total pressure; ρ and g denote the fluid density and gravitational acceleration, respectively; $\zeta^*(\mathbf{x}^*, t^*)$ denotes the surface elevation due to additional surface waves in the presence of the background flow, \mathbf{U}_3^* .

We choose the characteristic length L_c^* and velocity u_c^* to nondimensionalize the variables. In all cases we consider in Sec. IV, a wave frequency spectrum $S^*(\omega^*)$ is assumed which has a clear peak at a frequency ω_p^* . Therefore, we form the characteristic length, $L_c^* = g/\omega_p^{*2}$, and, characteristic velocity, $u_c^* = g/\omega_p^*$ using g and ω_p^* for convenience while our specific choice does not affect the generality of the theory derived in Secs. II and III. Explicitly,

$$(x^*, y^*, z^*) = (x, y, z)L_c^*, \quad t^* = \frac{L_c^*}{u_c^*} t, \quad \mathcal{V}^* = u_c^* \mathcal{V}. \quad (3a)$$

Here, \mathcal{V} represents any velocity component, and we define the wave-induced nondimensional pressure as

$$P = (P^* + \rho gz^*)/(\rho u_c^{*2}). \quad (4)$$

The dimensionless continuity and Euler momentum equations become

$$\nabla_3 \cdot \mathbf{V}_3 = 0, \quad (5)$$

$$\partial_t \mathbf{V}_3 + (\mathbf{V}_3 \cdot \nabla_3) \mathbf{U}_3 + (\mathbf{U}_3 \cdot \nabla_3) \mathbf{V}_3 + \nabla_3 P = -(\mathbf{V}_3 \cdot \nabla_3) \mathbf{V}_3, \quad (6)$$

for $-\infty < z < \zeta + \eta$.

The governing equations (5) and (6) should be solved subject to the dynamic and kinematic boundary conditions at the surface, respectively,

$$P - (\zeta + \eta) = 0 \quad \text{and} \quad w = \partial_t \zeta + (\mathbf{u} + \mathbf{U}) \cdot \nabla \zeta \quad \text{for } z = \zeta + \eta, \quad (7)$$

and the deepwater seabed condition

$$(\mathbf{u}, w) = 0 \quad \text{for } z \rightarrow -\infty. \quad (8)$$

B. Perturbation expansion and linear wave fields

We seek the solution for unknown velocity (\mathbf{V}) and elevation (ζ) of the boundary value problem described by Eqs. (5)–(8) in a form of power series in wave steepness denoted by ϵ ; i.e., a so-called Stokes expansion. To leading order, they are given by

$$[\zeta, \mathbf{u}, w, P] = \epsilon [\zeta^{(1)}, \mathbf{u}^{(1)}, w^{(1)}, P^{(1)}] + \epsilon^2 [\zeta^{(2)}, \mathbf{u}^{(2)}, w^{(2)}, P^{(2)}], \quad (9)$$

where the terms are kept up to second order in wave steepness and the superscript “(j)” denotes the jth order in wave steepness. Inserting the perturbed solutions (9) into the boundary value problem

described by Eqs. (5)–(8) and collecting the terms at the same order lead to the various boundary value problems at different orders in wave steepness.

Linear surface elevation due to irregular surface waves can be described by

$$\zeta^{(1)}(\mathbf{x}, t) = \mathcal{R} \left[\frac{1}{4\pi^2} \int |\hat{\zeta}(\mathbf{k})| e^{i\psi(\mathbf{k}, \mathbf{x}, t)} d\mathbf{k} \right], \quad (10)$$

where \mathcal{R} denotes the real part, \mathbf{k} denotes a wave-number vector in the horizontal plane, $\hat{\zeta}(\mathbf{k})$ denotes the linear wave elevation transformed in the Fourier \mathbf{k} plane, $\psi(\mathbf{k}, \mathbf{x}, t) = \mathbf{k} \cdot \mathbf{x} - \omega(\mathbf{k})t + \theta(\mathbf{k})$ denotes the rapidly varying phase with $\theta(\mathbf{k})$ the initial phase (angle) of the complex elevation $\hat{\zeta}(\mathbf{k})$ at the origin, $\omega(\mathbf{k})$ denotes the angular frequency of wave \mathbf{k} . Integration is over the whole \mathbf{k} plane. Without the detailed derivations, this paper employs the DIM developed by Li and Ellingsen [47], which provides a shear-modified dispersion relation $\omega = \omega(\mathbf{k})$. The dispersion relation is solved numerically together with the linear wave fields $\mathbf{u}^{(1)}$, $w^{(1)}$, and $P^{(1)}$.

The linear velocity and pressure in the physical plane can be obtained through an inverse Fourier transform as follows:

$$\begin{bmatrix} \mathbf{u}^{(1)}(\mathbf{x}, z, t) \\ w^{(1)}(\mathbf{x}, z, t) \\ P^{(1)}(\mathbf{x}, z, t) \end{bmatrix} = \mathcal{R} \left\{ \frac{1}{4\pi^2} \int \begin{bmatrix} \hat{\mathbf{u}}^{(1)}(\mathbf{k}, z) \\ \hat{w}^{(1)}(\mathbf{k}, z) \\ \hat{P}^{(1)}(\mathbf{k}, z) \end{bmatrix} e^{i\psi(\mathbf{k}, \mathbf{x}, t)} d\mathbf{k} \right\}. \quad (11)$$

Arbitrary linear wave fields can then be constructed by adding monochromatic components together, in the manner of Fourier transformation. We will not consider changes in mean water level herein and set $\eta = 0$ henceforth.

C. Second-order equations of motions

Inserting the solution for unknown velocity (\mathbf{V}) and surface elevation (ζ) in a form of power series given by Eq. (9) into the boundary value problem described by Eqs. (5)–(8), collecting the terms at second order in wave steepness, and eliminating the horizontal velocity ($\mathbf{u}^{(2)}$) and pressure ($P^{(2)}$) at second order leads to the following equations:

$$(\partial_t + \mathbf{U} \cdot \nabla) \nabla_3^2 w^{(2)} - \mathbf{U}'' \cdot \nabla w^{(2)} = \mathcal{N}^{(2)}(\mathbf{x}, z, t), \quad (12a)$$

for $-\infty < z < \zeta$,

$$(\partial_t + \mathbf{U} \cdot \nabla)^2 \partial_z w^{(2)} - \mathbf{U}' \cdot (\partial_t + \mathbf{U} \cdot \nabla) \nabla w^{(2)} - \nabla^2 w^{(2)} = \mathcal{F}^{(2)}(\mathbf{x}, z, t) \quad \text{for } z = 0, \quad (12b)$$

$$w^{(2)} = 0 \quad \text{for } z \rightarrow -\infty, \quad (12c)$$

where $\mathbf{U}'' = \partial_{zz}\mathbf{U}$, the forcing terms, $\mathcal{N}^{(2)}$ and $\mathcal{F}^{(2)}$, on the right-hand side of Eqs. (12a) and (12b) are functions of linear wave fields and are given by

$$\mathcal{N}^{(2)} = \nabla \cdot [(\mathbf{V}^{(1)} \cdot \nabla_3) \mathbf{u}^{(1)}]' - \nabla^2 [(\mathbf{V}^{(1)} \cdot \nabla_3) w^{(1)}], \quad (13a)$$

$$\begin{aligned} \mathcal{F}^{(2)} = & -\nabla^2 (\mathbf{u}^{(1)} \cdot \nabla \zeta^{(1)}) - [\nabla^2 (\partial_t + \mathbf{U} \cdot \nabla) P^{(1)}]' - \nabla^2 w^{(1)'} \zeta - \zeta^{(1)} \nabla^2 (\mathbf{U}' \cdot \nabla) P^{(1)} \\ & + (\partial_t + \mathbf{U} \cdot \nabla) \nabla \cdot [(\mathbf{V}^{(1)} \cdot \nabla_3) \mathbf{u}^{(1)}], \end{aligned} \quad (13b)$$

with notation $(\dots)' \equiv \partial_z(\dots)$. Inserting the linear solution from Eq. (11), the forcing term is then

$$\mathcal{N}^{(2)} = \mathcal{R} \left[\frac{1}{16\pi^4} \iint \hat{\mathcal{N}}^{(2)}(\mathbf{k}_1, \mathbf{k}_2, \mathbf{x}, z, t) d\mathbf{k}_1 d\mathbf{k}_2 \right], \quad (14a)$$

$$\mathcal{F}^{(2)} = \mathcal{R} \left[\frac{1}{16\pi^4} \iint \hat{\mathcal{F}}^{(2)}(\mathbf{k}_1, \mathbf{k}_2, \mathbf{x}, z, t) d\mathbf{k}_1 d\mathbf{k}_2 \right], \quad (14b)$$

where \mathbf{k}_1 and \mathbf{k}_2 denote the wave vector of two different linear wave trains; the forcing terms in the Fourier space are decomposed into the two types of second-order wave interactions as (see, e.g., Refs. [11,67])

$$\hat{\mathcal{N}}^{(2)} = \hat{\mathcal{N}}_+^{(2)}(\mathbf{k}_1, \mathbf{k}_2, z)e^{i(\psi_1+\psi_2)} + \hat{\mathcal{N}}_-^{(2)}(\mathbf{k}_1, \mathbf{k}_2, z)e^{i(\psi_1-\psi_2)}, \quad (14c)$$

$$\hat{\mathcal{F}}^{(2)} = \hat{\mathcal{F}}_+^{(2)}(\mathbf{k}_1, \mathbf{k}_2, z)e^{i(\psi_1+\psi_2)} + \hat{\mathcal{F}}_-^{(2)}(\mathbf{k}_1, \mathbf{k}_2, z)e^{i(\psi_1-\psi_2)}, \quad (14d)$$

where the subscripts “+” or “−” denote the components for the superharmonics and subharmonics, respectively; the wave phases are denoted with shorthand: $\psi_j = \psi(\mathbf{k}_j, \mathbf{x}, t)$; and the lengthy expressions of $\hat{\mathcal{N}}_\pm$ and $\hat{\mathcal{F}}_\pm$ are given in Appendix B.

With the linear velocity fields solved for by using the DIM [47], the second-order equations (12a)–(12c) for the vertical velocity $w^{(2)}$ can be solved numerically in Fourier space. Due to the interaction of different wave components and the main harmonic components of the forcing terms (i.e., $\mathcal{N}^{(2)}$ and $\mathcal{F}^{(2)}$) in the Fourier plane, the second-order vertical velocity

$$w^{(2)}(\mathbf{x}, z, t) = \mathcal{R} \left[\frac{1}{16\pi^4} \iint \hat{w}^{(2)}(\mathbf{k}_1, \mathbf{k}_2, \mathbf{x}, z, t) d\mathbf{k}_1 d\mathbf{k}_2 \right]. \quad (15)$$

We can also decompose $\hat{w}^{(2)}$ in terms corresponding to the two types of second-order wave interactions as

$$\hat{w}^{(2)}(\mathbf{k}_1, \mathbf{k}_2, z, \mathbf{x}, t) = \hat{w}_+^{(2)}(\mathbf{k}_1, \mathbf{k}_2, z)e^{i(\psi_1+\psi_2)} + \hat{w}_-^{(2)}(\mathbf{k}_1, \mathbf{k}_2, z)e^{i(\psi_1-\psi_2)}. \quad (16)$$

Each component on the right-hand side of Eq. (16) for $\hat{w}^{(2)}$ can be solved for numerically from the boundary value problem as follows:

$$\hat{w}_\pm^{(2)''} - \left(|\mathbf{k}_\pm|^2 + \frac{\mathbf{k}_\pm \cdot \mathbf{U}''}{\mathbf{k}_\pm \cdot \mathbf{U} - \omega_\pm} \right) \hat{w}_\pm^{(2)} = \frac{\hat{\mathcal{N}}_\pm^{(2)}}{\mathbf{k}_\pm \cdot \mathbf{U} - \omega_\pm}, \quad (17a)$$

for $-\infty < z < 0$, where $\mathbf{k}_\pm = \mathbf{k}_1 \pm \mathbf{k}_2$, $\omega_\pm = \omega(\mathbf{k}_1) \pm \omega(\mathbf{k}_2)$, and boundary conditions

$$-(\mathbf{k}_\pm \cdot \mathbf{U} - \omega_\pm)^2 \partial_z \hat{w}_\pm^{(2)} + [\mathbf{k}_\pm \cdot \mathbf{U}'(\mathbf{k}_\pm \cdot \mathbf{U} - \omega_\pm) + |\mathbf{k}_\pm|^2] \hat{w}_\pm^{(2)} = \hat{\mathcal{F}}_\pm^{(2)}(\mathbf{k}_\pm, z) \text{ for } z = \eta, \quad (17b)$$

$$\hat{w}_\pm^{(2)} = 0 \text{ for } z \rightarrow -\infty. \quad (17c)$$

In our problem setting the waves obtained from the second-order boundary value problems (17a), (17b), and (17c) are bound since they do not satisfy the linear dispersion relation and can only propagate together with their linear free contents. Moreover, with the linear free waves obtained, the second-order ordinary equation (17a) with two boundary conditions (17b) and (17c) can be solved for numerically with a finite difference method where a central Euler approximation to the second-order derivative, $\hat{w}_\pm^{(2)''}$, was used in this paper. Especially for directionally spread irregular waves in a random sea, we remark that the numerical estimation of double Fourier integrals in a form as Eqs. (14a) and (14b) is computationally expensive for statistical analysis. Nevertheless, the framework developed here can be easily reformulated such that a pseudospectral method for the second-order interaction of waves in a vertically sheared current can be used, following papers, e.g., Refs. [68,69] for a high-order spectral method and Ref. [70] for a semianalytical approach. In doing so, it allows for reducing the computational operations of $\mathcal{O}(N_g^2)$ to $\mathcal{O}(N_g \ln N_g)$, with N_g the total number of discrete points chosen for the grid of a computational domain.

The second-order wave surface elevation $\zeta^{(2)}$ can be obtained from the following kinematic boundary condition

$$(\partial_t + \mathbf{U} \cdot \nabla) \zeta^{(2)} = w^{(2)} + \zeta^{(1)} w^{(1)'} - \frac{1}{2} \mathbf{U}' \cdot \nabla (\zeta^{(1)})^2 - \mathbf{u}^{(1)} \cdot \nabla \zeta^{(1)}, \quad (18)$$

which leads to the surface elevation $\zeta^{(2)}$ given by

$$\zeta^{(2)}(\mathbf{x}, t) = \mathcal{R} \left[\frac{1}{16\pi^2} \iint \hat{\zeta}^{(2)}(\mathbf{k}_1, \mathbf{k}_2; \mathbf{x}, t) d\mathbf{k}_1 d\mathbf{k}_2 \right] \text{ with} \quad (19a)$$

$$\hat{\zeta}^{(2)} = \hat{\zeta}_+^{(2)}(\mathbf{k}_1, \mathbf{k}_2) e^{i(\psi_1 + \psi_2)} + \hat{\zeta}_-^{(2)}(\mathbf{k}_1, \mathbf{k}_2) e^{i(\psi_1 - \psi_2)}, \quad (19b)$$

where the elevation $\hat{\zeta}_\pm^{(2)}$ is obtained from Eq. (18) in the Fourier plane through substituting the vertical velocity $w^{(2)}$ and the linear wave fields $\mathbf{u}^{(1)}$ and $\zeta^{(1)}$. It is noteworthy that for $\mathbf{k}_1 = \mathbf{k}_2$ the superharmonics ($\hat{\zeta}_+^{(2)}$) reduce to the well-known second-order Stokes waves. The subharmonics ($\hat{\zeta}_-^{(2)}$) become a constant, which refers to a mean water level and is ignored in our simulation.

D. Notation in the frequency domain

The theory in Sec. II so far was formulated in reciprocal horizontal (\mathbf{k}) space. Often it is more convenient in practice to use a frequency domain formulation, for instance when working with power spectra, from time series from wave buoys, say. In the presence of a vertically sheared current the dispersion relation $\omega = \omega(\mathbf{k})$ is anisotropic in any reference system, i.e., ω is always a function of the direction of \mathbf{k} , not only its modulus. This introduces subtleties in interpreting nondirectional wave frequency data in the presence of a sheared current as wavelength cannot be inferred from frequency alone. We herein work in two dimensions, i.e., waves propagating with known direction either along or against the current, thus eschewing this potential complication.

The linear and quadratic-order elevations are denoted

$$\zeta^{(1)}(\mathbf{x}, t) = \mathcal{R} \left(\int a(\omega) e^{i\psi} d\omega \right), \quad (20a)$$

$$\zeta^{(2)}(\mathbf{x}, t) = \mathcal{R} \left\{ \iint a_1 a_2 [\hat{A}_{12}^+ e^{i(\psi_1 + \psi_2)} + \hat{A}_{12}^- e^{i(\psi_1 - \psi_2)}] d\omega_1 d\omega_2 \right\}. \quad (20b)$$

where $a(\omega)$ denotes the linear (real) amplitude of a wave with frequency ω and complex phase $\psi(\omega) = \mathbf{k} \cdot \mathbf{x} - \omega t + \theta(\omega)$, where we solve the dispersion relation $\omega = \omega(\mathbf{k})$ for the wave vector with a given frequency using the DIM method as noted. The following notations are used: $a_n = a(\omega_n)$, $\psi_n = \psi(\omega_n)$, $\hat{A}_{12}^\pm = \hat{A}^\pm(\omega_1, \omega_2)$ with

$$\hat{A}^\pm(\omega_1, \omega_2) = \frac{|\hat{\zeta}_\pm^{(2)}(\omega_1, \omega_2)|}{a_1 a_2}, \quad (20c)$$

where $\hat{\zeta}_\pm^{(2)}$ was given by Eq. (19) with the difference that it is expressed here in the frequency domain instead.

III. WAVES OF A NARROW BANDWIDTH

In this section we present the skewness and probability density function of the surface displacement and wave crests in the special case where the bandwidth of the wave spectrum is narrow. We now use the frequency-domain formulation of Sec. II D. Consider an ensemble of waves described in the form of Eq. (20) where the amplitude $a(\omega)$ becomes an independent random variable denoted by $\tilde{a}(\omega)$ which follows a Rayleigh distribution based on a spectrum $S(\omega)$ and where the phase θ becomes another independent random variable, $\tilde{\theta}$, which is uniformly distributed in the range $[0, 2\pi)$. Therefore, $\zeta(\mathbf{x}, t) \rightarrow \tilde{\zeta}(\tilde{a}(\omega), \tilde{\theta}(\omega))$. The j th spectral moment m_j is defined as

$$m_j = \int \omega^j S(\omega) d\omega; \quad j \in \{0, 1, 2, \dots\}. \quad (21)$$

Assuming zero mean water level as before, the standard deviation, σ , and skewness, λ_3 , of the surface elevation are

$$\sigma = \sqrt{\langle \tilde{\zeta}^2 \rangle}, \quad (22a)$$

$$\text{and } \lambda_3 = \langle \tilde{\zeta}^3 \rangle / \sigma^3, \quad (22b)$$

where $\langle \dots \rangle$ denotes the expectation value of random variables. Assuming the energy spectrum $S(\omega)$ to have a narrow bandwidth [$\nu = \sqrt{1 - m_2^2/(m_0 m_4)} \ll 1$], we follow the detailed derivations of Fedele and Tayfun [23] using the elevations (20), and obtain to $\mathcal{O}(\epsilon)$

$$\sigma^2 = m_0, \quad (23a)$$

$$\text{and } \lambda_3 = 6\sigma \hat{A}_{mm}^+, \quad (23b)$$

where $\hat{A}_{mm}^+ = \hat{A}(\omega_m, \omega_m)$ denotes the second-order superharmonic amplitude of the spectral mean wave, with ω_m the spectral mean frequency given by

$$\omega_m = m_1/m_0. \quad (24)$$

The skewness given by Eq. (23b) agrees with Fedele and Tayfun [23], Srokosz and Longuet-Higgins [71], and Li *et al.* [10] for waves in the absence of a shear current, which is clear when noting that the superharmonic amplitude \hat{A}_{mm}^+ can be written as $k_m/2 \equiv \omega_m^2/(2g)$ in the case for second-order deepwater Stokes waves (see, e.g., Ref. [11]). It is different from Fedele and Tayfun [23] to the extent that it does not account for the effect of bandwidth as it is not so straightforward due to a shear current. Nevertheless, it allows us to take into account the effect of a shear current to some extent. Especially, if all linear waves follow the same power energy spectrum with a narrow bandwidth, i.e., m_j are identical for all cases, then the spectral mean given by Eq. (24) is identical regardless of a shear current. A shear current affects the skewness given by Eq. (23b) through the second-order superharmonic amplitude of the spectral mean wave, compared with the cases in the absence.

Following Longuet-Higgins [12], we obtain that the normalized surface displacements follow the distribution

$$p_\zeta(\tilde{\zeta}) = \frac{1}{\sqrt{2\pi}} e^{-\tilde{\zeta}^2/2} \left[1 + \frac{\lambda_3}{6} \tilde{\zeta} (\tilde{\zeta}^2 - 3) \right]. \quad (25)$$

For linear waves, where $\lambda_3 = 0$, expression (25) becomes a Gaussian distribution. Different from Longuet-Higgins [12], the probability density function given by Eq. (25) can account for the effect of a shear current because the skewness λ_3 is modified according to Eq. (23b) which considers the effect of a shear current.

Similarly, following Forristall [17], the ‘‘exceedance probability,’’ i.e., the probability that a randomly chosen wave crest X_c exceeds the value $\tilde{\zeta}_c$, is found as

$$P(X_c > \tilde{\zeta}_c) = \exp \left[-\frac{1}{8(\hat{A}_{mm}^+ \sigma)^2} \left(\sqrt{1 + \frac{16\tilde{\zeta}_c}{H_s} \hat{A}_{mm}^+ \sigma} - 1 \right)^2 \right], \quad (26)$$

where H_s is the significant wave height. The exceedance probability given by Eq. (26) agrees with Eq. (2.12) by Li *et al.* [10] with the same chosen notations whereas the main difference lies in that the effect of a shear current enters here via the superharmonic amplitude of the spectral mean wave, \hat{A}_{mm}^+ . In the limit of infinitesimal wave, i.e., $m_0 \rightarrow 0^+$, the exceedance probability of wave crest becomes

$$P(X_c > \tilde{\zeta}_c) = \exp \left(-8 \frac{\tilde{\zeta}_c^2}{H_s^2} \right), \quad (27)$$

which is the Rayleigh distribution as expected. For second-order deepwater Stokes waves in the absence of a shear current which admits $\hat{A}_{mm}^+ = k_m/2 \equiv \omega_m^2/(2g)$, the exceedance probability given by Eq. (26) is identical to Eq. (4) in Forristall [17]. We will refer repeatedly to Eqs. (25) and (26) in Sec. VB.

IV. NUMERICAL SETUP

In our simulations, we generate two-dimensional (long-crested or unidirectional) waves from realistic spectra. Doing so implies that the possible triad resonant interactions in three dimensions considered in previous papers, e.g., Refs. [38,58,72] are assumed negligible in the simulations. We choose the characteristic velocity, $u_c^* = g/\omega_p^*$, as defined in Sec. II A. Here, ω_p^* is the peak frequency of the spectrum; although $\omega_p = 1$ by definition, we find it instructive to retain it in some equations below.

We begin by defining the terms following and opposing shear for two-dimensional flow, i.e., where all waves propagate parallel or antiparallel to the mean current. We will assume that waves travel along the positive x axis. We then define

- (1) Following shear: $U'(z) < 0$,
- (2) Opposing shear: $U'(z) > 0$.

Following (opposing) shear corresponds to the situation where the flow increases (decreases) in the direction of propagation with increasing depth.

Note carefully the distinction between following (opposing) shear and following (opposing) current. When seen in an Earth-fixed reference system, currents in nature are often strongest near the surface and decrease to zero at larger depths, such as in the Columbia River mouth current we regard in Sec. V E. In such a case a “following surface current” $U(z) > 0$ would correspond to opposing shear and vice versa. For clarity of comparison between cases we shall work in a surface-following frame and, therefore, assume $U(0) = 0$, in which case following shear implies positive $U(z)$ for a monotonically varying U . Doing so allows us to focus only on the effects due to the profile shear and curvature of a current.

A. Realization of random seas states for linear waves

We follow Tayfun [13] and Tucker et al. [66] for the realization of random sea states, which assumes Rayleigh distributed amplitude of linear waves and uniformly distributed wave phases in the range of $[0, 2\pi)$. The energy spectrum we choose for computation is JONSWAP spectrum [73] with a peak enhancement (or peakedness) parameter of $\gamma = 3.3$ and moderately narrow bandwidth [74,75], which is shown in Fig. 1(a).

The JONSWAP spectrum is given by (recall that $\omega_p = 1$)

$$S_J(\omega) = \frac{\tilde{\alpha}_J}{\omega^5} \exp[-1.25\omega^{-4}] \gamma^{b(\omega)}, \quad (28)$$

where the peak enhancement factor γ appears with an exponent

$$b(\omega) = \exp\left[-\frac{(\omega - 1)^2}{2\sigma_J^2}\right], \quad (29)$$

and

$$\sigma_J = \begin{cases} 0.07, & \omega \leq 1, \\ 0.09, & \omega > 1. \end{cases} \quad (30)$$

The parameter $\tilde{\alpha}_J$ is chosen such that the JONSWAP spectrum is fixed for all numerical cases, i.e., independent of a current profile. The frequency is truncated at $0.01\omega_p$ and $2.6\omega_p$. The bandwidth

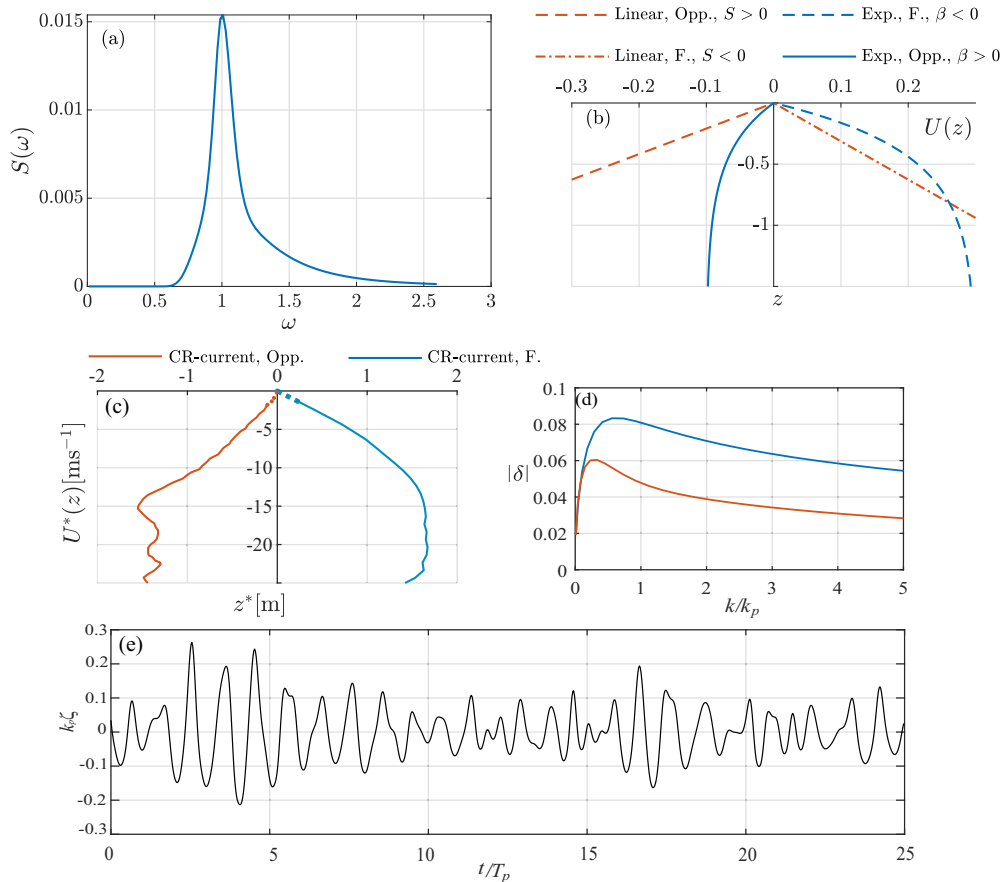


FIG. 1. (a) JONSWAP power energy spectrum of linear waves with nondimensional peak frequency $\omega_p = 1$ and bulk steepness $\epsilon = 0.14$; (b) examples of linear and exponential (“Exp.”) shear profiles where both opposing (“Opp.”) and following (“F.”) shear are shown; (c) two tidal current profiles from Zippel and Thomson [54] measured at the mouth of the Columbia River (“CR”), during ebb tide (following shear, “F.”), and flood (mostly opposing shear, “Opp.”), respectively. Note that in an Earth-fixed coordinate system (see Fig. 3 of Ref. [54]) these correspond to opposing and following surface currents, respectively. Dashed lines are extrapolations from $z = 1.35$ m to the surface; (d) wave-averaged shear $|\delta(k)|$ for the two profiles in panel (c); (e) extract of the time series of wave surface elevation for illustration, here without current.

parameter is defined as

$$v = \sqrt{1 - \frac{m_2^2}{m_0 m_4}} \quad (31)$$

and here $v = 0.5284$. For another widely used bandwidth parameter $v_L = \sqrt{m_0 m_2 / m_1^2 - 1}$ proposed by Longuet-Higgins [76], the value becomes 0.2689. We choose bulk steepness $\epsilon = \frac{1}{2} H_s = 0.14$ in all cases. As noted, the peak frequency ($\omega_p = 1$), significant wave height (H_s), and the moments (m_j) of the JONSWAP spectrum are fixed for all cases, regardless of the profile of a shear current. However, the spectrum peak wave number $k_p \equiv k(\omega_p) = k(1) \neq 1$ in the presence of a current, since the linear dispersion relation $k(\omega)$ depends on $U(z)$, as explained in Secs. II and III.

Once the input spectrum is determined, the amplitudes a_i of a total of N_s linear elementary waves are generated with a prescribed significant wave height, with

$$\sum_{i=1}^{N_s} \frac{\tilde{a}_i^2}{2} = \int_{\omega} S(\omega) d\omega \quad \text{and} \quad \zeta^{(1)}(x, t) = \sum_{i=1}^{N_s} \tilde{a}_i \cos(k_i x - \omega_i t + \tilde{\theta}_i), \quad (32)$$

where the energy spectrum is discretized with unequal frequency intervals and an identical area of N_s energy bins [i.e., constant $S(\omega_i) d\omega_i$]. For a train of random waves, we assume the amplitude \tilde{a}_i follows a Rayleigh distribution and the phase $\tilde{\theta}$ a uniform distribution in the range $[0, 2\pi)$ similar to Sec. III and Tayfun [15]. The wave numbers k_i are found numerically from ω_i using the DIM algorithm as described. We especially computed the temporal evolution of the linear surface elevation at $x = 0$ and then, the second-order correction of the wave surface are calculated from Eqs. (19a) and (19b).

We also make a flow diagram of numerical implementations, which is shown in Appendix A. In our simulations, 128 elementary waves are generated from the relevant input wave spectra and ran from $0 \leq t \leq 5638$. Two thousand realizations were simulated to assure that the skewness of the wave surface elevation was converged.

B. Current profiles and cases considered

We consider three different current profiles with different parameters, which are typical of the open ocean, including an exponential profile, a linearly sheared current, and one that was measured at the mouth of the Columbia River from Zippel and Thomson [54], as shown in Figs. 1(b) and 1(c).

1. Model profiles

The exponential and linear profile of shear current are parameterized as

$$\mathbf{U}_{\text{exp}}(z) = \beta[\exp(\alpha z) - 1]\mathbf{e}_x, \quad (33a)$$

$$\text{and } \mathbf{U}_{\text{lin}} = Sz\mathbf{e}_x, \quad (33b)$$

respectively, where \mathbf{e}_x is a unit vector along the positive x axis, the subscripts ‘‘exp’’ and ‘‘L’’ denote the exponential and linear profile, respectively, α ($\alpha > 0$), β , and S are dimensionless parameters that define the magnitude and shear strength of a current profile relative to the peak wave parameters. Note that we choose a reference system following the free surface so that $\mathbf{U}(0) = 0$. This eschews arbitrary Doppler shift terms which would clutter the formalism, reduces the number of free parameters, and makes results from different profiles immediately comparable. The choice also emphasizes that it is the shear $U'(z)$ and curvature $U''(z)$ which cause statistics to be altered, not the strength of the current itself. The surface shear is obtained from Eq. (33),

$$\mathbf{U}'_{\text{exp}}(0) = \alpha\beta\mathbf{e}_x, \quad (34a)$$

$$\text{and } \mathbf{U}'_{\text{lin}}(0) = S\mathbf{e}_x, \quad (34b)$$

which denote the profile shear of an exponential and linearly sheared current at still water surface, respectively.

Recall that following (opposing) shear correspond to $U'(z) < 0$ (> 0). We wish our model current to have strong, but not unreasonable vertical shear. To determine how strongly the current shear affects the dispersion of a wave of wave number k^* or frequency ω^* (whichever is known), the proper parameter to consider is the wave-weighted depth-averaged shear [60], respectively,

$$\delta = \frac{1}{c_0^*} \int_{-\infty}^0 U^{*'}(z^*) e^{2k^* z^*} dz^* = \sqrt{k} \int_{-\infty}^0 U'(z) e^{2kz} dz, \quad (35)$$

nondimensionlized as explained in Sec. II A, and $c_0^* = \sqrt{g/k^*}$. Inserting $U'(z) = \alpha\beta \exp(2\alpha z)$ gives

$$|\delta| = \frac{|\alpha\beta|\sqrt{k}}{\alpha + 2k}, \quad (36)$$

whose maximum value is found at $k = \alpha/2$ and in either case, $|\delta|_{\max} = |\alpha\beta|/\sqrt{8}$. In the following sections we use $\alpha = 2.5$ and $|\beta| \leq 0.3$ giving $|\delta|_{\max} \lesssim 0.17$.

2. Profile from the mouth of the Columbia River

The profiles of tidal currents in the mouth of the Columbia River have been used as a test-case in a wide array of studies of wave-shear current interactions (e.g., Refs. [46,47,54,77–81]) due to the availability of high quality current profile measurements [54,64] and strong vertical shear. Herein we use the profiles measured by Zippel and Thomson [54] using an acoustic Doppler current profiler (ADCP) mounted on a drifter. The currents were measured between 1.35 m and 25 m depth, but we require profiles ranging all the way to the undisturbed surface level. What the profile might look like in the top 1.35 m is not obvious; the shear strength can drop sharply closer to the surface [82], but could also increase all the way to the top centimetres [62]. We use a polynomial extrapolation as shown in Fig. 1(c); we show in Appendix D that two other common approaches produce no discernible difference in the resulting skewness. The current profiles reported in Zippel and Thomson [54] and shown in Fig. 8(a) are fitted with a seventh-order polynomial to the surface. The wave-averaged dimensionless shear δ of Eq. (35) for the two profiles in Fig. 1(c) are seen in Fig. 1(d), peaking near 0.095 for the following current.

Note that the currents taken from Zippel and Thomson [54] are not extreme for the location—the shear current used in, e.g., Li *et al.* [83] taken from the measurements during the RISE project [64] peaks at a value $\delta \approx 0.19$, more than our strongest exponential model current. For comparison with the results of Zippel and Thomson [54] for ebb and flow respectively, we choose the more conservative profiles in the latter.

We remark that Zakharov and Shrira [58] proposed a set of analytical theory for second-order wave-shear current problem with the assumptions $U' < 0$ and $U_{\max}/c \ll 1$. Here, U_{\max} and c refer to the maximum velocity of shear current and phase velocity of surface wave, respectively. From Fig. 1(c) the parameter U_{\max}/c of Columbia River current for peak wave could reach 0.2. Hence, the theory by Zakharov and Shrira [58] is not expected to be quantitatively accurate for the Columbia River current cases considered herein.

V. RESULTS

We present second order statistical quantities for waves on model shear currents, generalizing a number of classical results. The example for time series of wave surface elevation is shown in Fig. 1(e). All the statistical quantities are based on very long time series.

A. The distribution of wave surface elevation

In this section we examine the effects of subsurface shear on the distribution of surface elevation to second order in steepness. We compare the case of no current to cases with following and opposing shear. We also show comparisons of the same case with shear between the broadband and narrow-band theory presented in Secs. II and III, respectively. A moderately narrowband spectrum is considered, with the linear wave field amplitudes chosen from a Gaussian distribution with zero mean and variance σ^2 .

Figure 2 plots the numerically calculated PDFs of wave surface elevation in the presence of a model current [Eq. (33a)] varying exponentially with depth, comparing our numerical results based on the broad-band theory presented in Sec. II, together with different theoretical predictions: a Gaussian distribution and theoretical predictions based on a narrow-band assumption presented

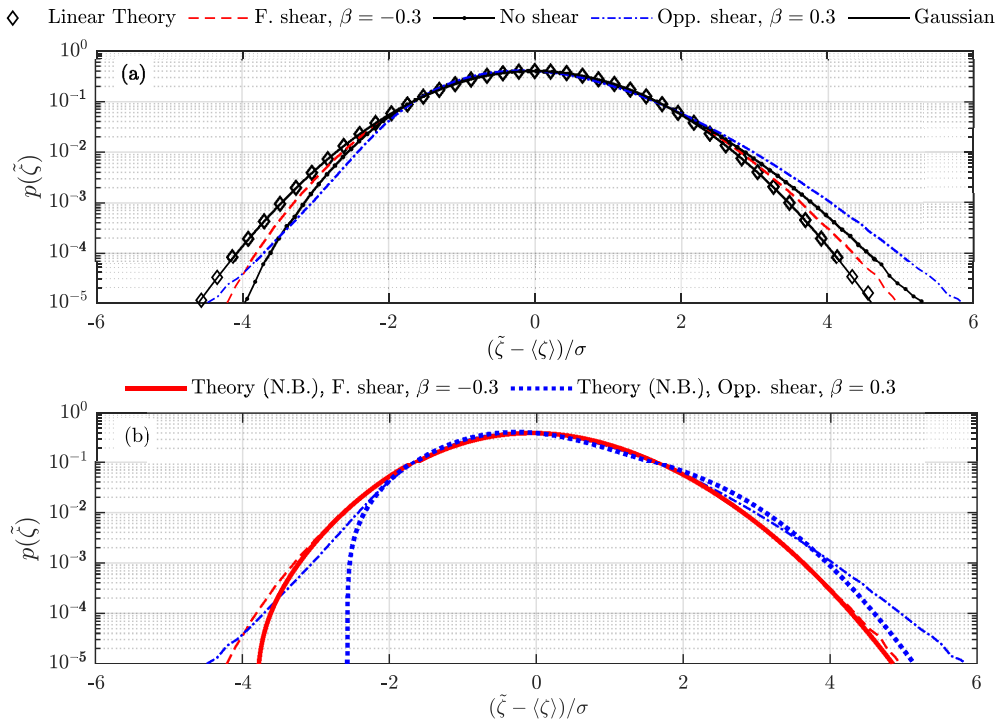


FIG. 2. Probability density function (PDF) of wave surface elevation for a moderately narrowband Gaussian input spectrum assuming the exponential current profile (33a) with β the magnitude of the shear at a still water surface. Numerical results for $\beta = -0.3$ (following shear, “F. shear”) and $\beta = 0.3$ (opposing shear: “Opp. shear”) are compared to (a) the linear prediction and the case without current, and (b) the narrow-band (N.B.) theory based on Eq. (25).

in Sec. III. We first discuss the results shown by Fig. 2(a). When both second-order corrections and shear are omitted, the numerically calculated PDF (diamond symbols) should coincide with the Gaussian input distribution (zero mean, variance σ^2) which indeed it does. The probability of amplitudes greater than about two standard deviations from the mean are decreased for negative values (deep troughs) and increased for positive (high crests), conforming with the known properties of second-order Stokes waves: the wave crests get higher and wave troughs get flatter.

The presence of opposing shear $U'(z) > 0$ enhances the wave crests and flatten the wave troughs compared to no current, while following shear current has the opposite effects. The effect on second-order statistics from the shear is considerable in the range of larger wave crests ($> 2\sigma$) but modest for wave troughs (negative elevation) in this case.

A comparison of the probability density function of surface elevation for the cases in the presence of shear is shown in Fig. 2(b) comparing the numerical results based on the full theory of Sec. II and the narrow-band approximation in Sec. III. It is seen that the narrow-band assumption agrees with the broad-band theory up to three and two standard deviations for the cases with following (“F. shear”) and opposing shear (“Opp. shear”), respectively; for following shear the approximation would be good enough for most practical purposes, except extreme statistics. The narrow-band approximation underestimates the probability of the most extreme events in both cases, but to very varying degrees as the figure shows.

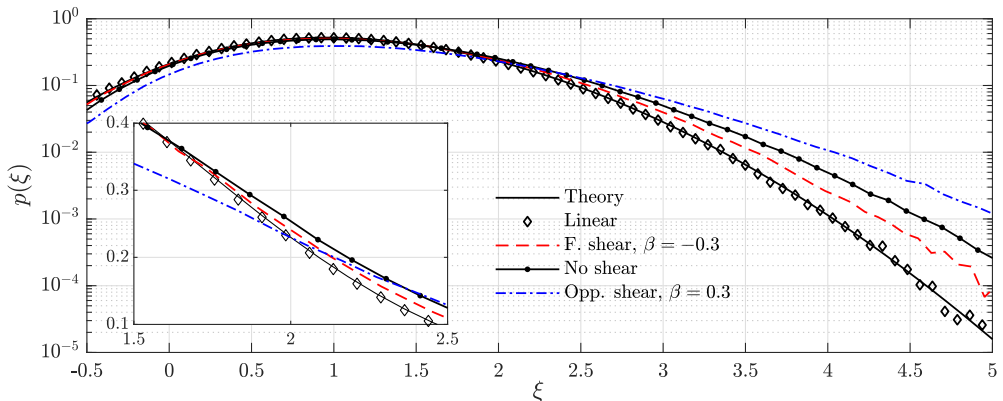


FIG. 3. Probability density function of the dimensionless maxima ($\xi = \zeta_m/\sigma$) of the wave elevation. The theoretical estimates (“Theory”) are based on Eq. (37) and the other cases shown are the same as Fig. 2(a). The inset shows a zoom of a subrange of ξ values where graphs cross.

B. The distribution of wave maxima and crest height

The crest height is conventionally defined as the highest surface elevation reached inside discrete time intervals. Within each time interval, the surface elevation is above the mean-surface level, $\zeta > 0$, i.e., delimited by consecutive zero crossings $\zeta(t) = 0$ so that $\zeta'(t) > 0$ (< 0) at the beginning (end). This contrasts, in general, with a *surface elevation maximum* ζ_m , which is any point where $\zeta'(t) = 0$ and $\zeta''(t) < 0$. Surface elevation maxima can be negative for a broadband spectrum, whereas for a sufficiently narrow spectrum, the two are positive and coincide: every maximum is also a wave crest.

As discussed by Goda [84, Chapter 2], when the spectrum is not narrow there is no universal and unique definition of wave height in a time series. The most common definition based on zero-crossings described above is theoretically somewhat unsatisfactory in a broadband setting; a more theoretically coherent method proposed by Janssen [5,85] based on the envelope of ζ is also in use [86]. For theoretical derivations the envelope procedure becomes more cumbersome for weakly nonlinear waves, requiring expressions for third and fourth statistical moments to adequately describe a generic wave distribution. In the following we use the customary definition using zero-crossing, as described above, bearing in mind that the identification of individual waves, and hence its distribution of maxima, will carry some dependence on the spectral shape which vanishes in the narrow-band limit.

For a narrow frequency spectrum according to linear theory, the dimensionless wave crest heights ζ_c , normalized by significant wave height H_s , is distributed according to the Rayleigh probability function as given by Eq. (27). It is difficult, however, to determine theoretically the probability distribution of crest heights if the waves have a broad frequency spectrum. Hence, Cartwright and Longuet-Higgins [87] made a compromise by calculating the distribution of surface elevation maxima denoted by ζ_m , adapting the theory of Rice [88] from in electrical signal processing to an ocean waves setting. Their result based on linear theory for a broadband spectrum is

$$p(\xi) = \frac{1}{\sqrt{2\pi}} \nu \exp\left(-\frac{\xi^2}{2\nu^2}\right) + \frac{\xi\sqrt{1-\nu^2}}{2} \exp\left(-\frac{1}{2}\xi^2\right) \left[1 + \operatorname{erf}\left(\frac{\xi\sqrt{1-\nu^2}}{\sqrt{2}\nu}\right)\right], \quad (37)$$

where $\xi = \zeta_m/\sigma$ denotes the normalized maxima, the bandwidth parameter ν is defined in Eq. (31), m_j is the j th moment of the energy spectrum given by Eq. (21), and erf is the error function.

Figure 3 shows the PDF of the surface elevation maxima for linear and nonlinear results. We also plot the theoretical estimates with Eq. (37), which is given by solid line in the figure. When

nonlinear effects and shear are both omitted, the numerically calculated PDF (diamond symbols) should coincide with Eq. (37), which indeed it does as the figure shows. The second-order results show increased probability of large wave maxima in all cases. Notice that negative-valued surface maxima occurs for a broadband spectrum, corresponding to nonzero $p(\xi)$ for $\xi < 0$. The probability of negative maxima increases monotonically with bandwidth parameter ν .

The most prominent nonlinear effect in Fig. 3 is for opposing shear, where probability for large maxima above approximately two standard deviations is enhanced in our simulation, whereas maxima below this threshold are made less probable. The current with following shear has the opposite influence. This phenomenon is consistent with the PDF of wave surface elevation studied in Sec. V A.

There exists a few commonly used expressions for crest height distribution obtained by empirical fitting, theoretical considerations, or parametrization [17,23,89–93]. One example we use in this section is the distribution derived by Tayfun [14] for a narrow-band spectrum, which corresponds to our narrow-band equation (26) in the limiting case of no current, i.e., $k_m^* \rightarrow k_{m0}^* = \omega_m^{*2}/g$ (shear-free dispersion relation in nondimensional units). To the best of our knowledge, theoretical expressions for wave crest distribution with a broad-band frequency spectrum have not been reported.

Figure 4 shows the numerical PDF and exceedance probability of the scaled crest height compared to the Rayleigh and Tayfun distributions. Notice in Fig. 4(a) that for very low crests $\tilde{\zeta}_c \lesssim 0.1H_s$ the probability density of wave crest height deviates noticeably from the Rayleigh curve, consistent with Fig. 3. The reason is that finite bandwidth allows negative maxima (hence a finite probability density at zero crest height), whereas the narrow-band Rayleigh distribution only allows positive maxima. The physical significance of this difference is perhaps not so high being primarily a result of the definition of a crest, referring somewhat arbitrarily to the mean water level. The tail of our numerical results without shear still agrees well with those produced by the Rayleigh distribution [23], perhaps surprising in light of the linear theory for broadband waves due to Cartwright and Longuet-Higgins [87]. This can be explained by noting that in the context of their theory our spectrum is still relatively narrow, since the bandwidth parameter $\nu \approx 0.53$ as defined in Eq. (31) is considerably smaller than unity.

It can be observed in Figs. 4(b) and 4(c) that, when nonlinear second-order corrections are accounted for, the tail of the simulated curve for the case with no shear clearly exceeds the Rayleigh distribution values, yet remain lower than the Tayfun distribution curve. This observation was also made by Fedele and Tayfun [23] who considered broadband waves without current; They showed that in that case the Tayfun distribution is an upper bound for the wave crest distribution to second order in steepness.

With the additional presence of a shear current and broader spectrum, crest distributions can clearly exceed that of Tayfun. The numerical results show substantial differences between the three currents considered, consistent with the general trend observed before: opposing shear makes high crests more probable and viceversa. The gray dashed vertical line in Fig. 4 refers to the conventional criterion for rogue waves, which is $\tilde{\zeta}_c/H_s = 1.25$ [94]. Compared with the no-shear current case, the opposing shear current leads to significant enhancement in the occurrence probability of rogue wave, as shown in Fig. 4(e). The presence of following shear current has the opposite influence. The exceedance probability increases monotonously as a function of the shear strength β , which is shown in Figs. 4(b) and 4(c).

We note in passing, however, that whereas the probability of *unusually high* (rogue) waves is decreased on following shear, the significant wave height itself will often be increased. A typical situation where this occurs is when the shear current, measured in a land-fixed reference system, has its greatest velocity at the surface. In this case the current itself is opposing in an earth-fixed frame of reference, so waves generated elsewhere will steepen as they encounter the current. Thus, the expectation in many real scenarios would be that following shear makes for rougher seas overall, whereas with opposing shear, while calmer on the whole, have an increased probability of *surprisingly* high crests. This point was discussed in depth by Hjelmervik and Trulsen [30].

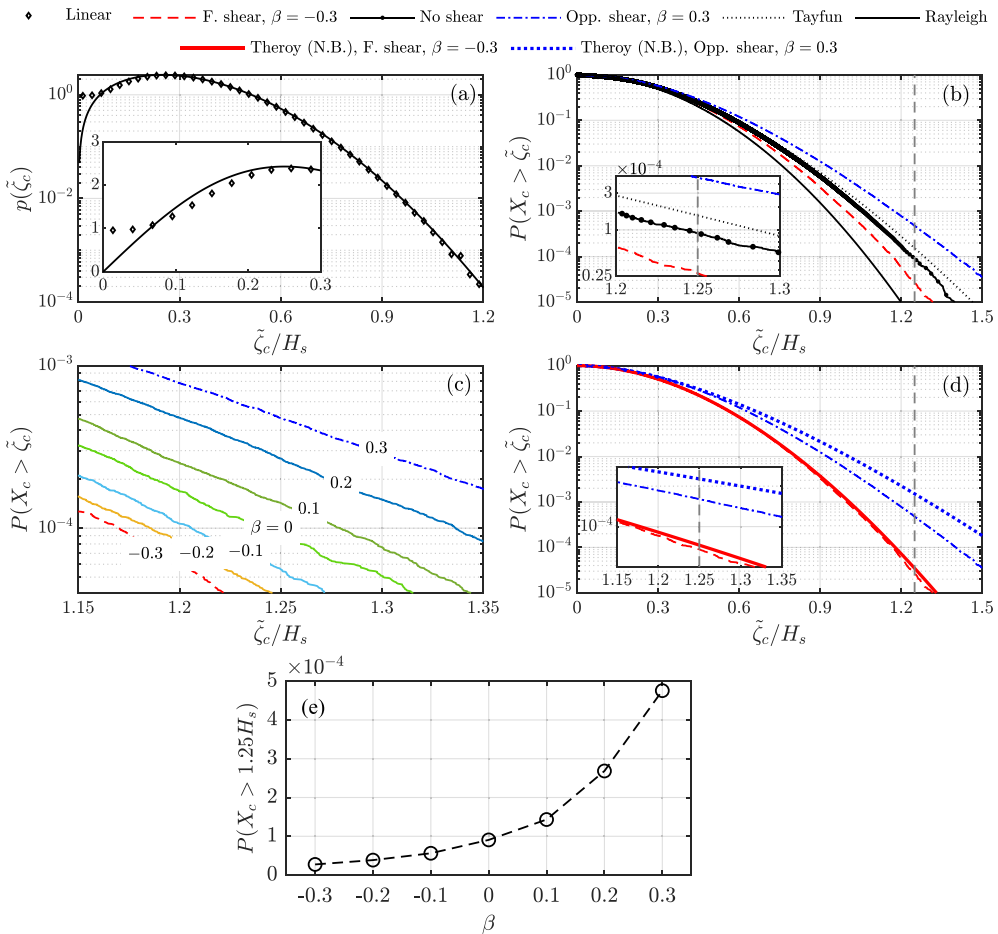


FIG. 4. Numerically calculated probability density function (a) and exceedance probability (b, c, d) for wave crests. An exponential shear profile, Eq. (33a), was assumed. (a) Linear waves based on numerical simulations and the Rayleigh probability density function; (b), (c) nonlinear wave fields for varying shear strength; (d) the broad-band and narrow-band results for cases with shear based on the theory in Secs. II and III, respectively. We used Eq. (26) with $\beta = 0$ for the Tayfun distribution. (e) Occurrence probability of rogue waves for all the exponential shear cases in panel (c).

Figure 4(d) compares the exceedance probability of wave crest between the narrow-band predictions and numerical results for the cases with a shear current, the former of which are obtained by using Eq. (26). We observe that the narrow-band assumption leads to a small and large overestimate of the occurrence probability of wave crest for the case with a following and opposing shear current, respectively. The differences for the following current are nearly negligible, as being consistent with Fig. 2(b), but are much more pronounced for the opposing shear case. Figure 4(d) suggests a similar conclusion as Fedele and Tayfun [23] who state that the narrow-band assumption would produce an upper bound of the exceedance probability of wave crests. Since the effect of current shear on waves depend on both the shift in wavelength as reflected from the linear dispersion relation and on the amplitude of the second-order superharmonic bound waves, the overall effect of a current on waves of a broad-band spectrum will in general differ in a nontrivial way from a narrow one which only depends on the amplitude of the spectral mean wave, \hat{A}_{nm}^+ . As a result, the assumption

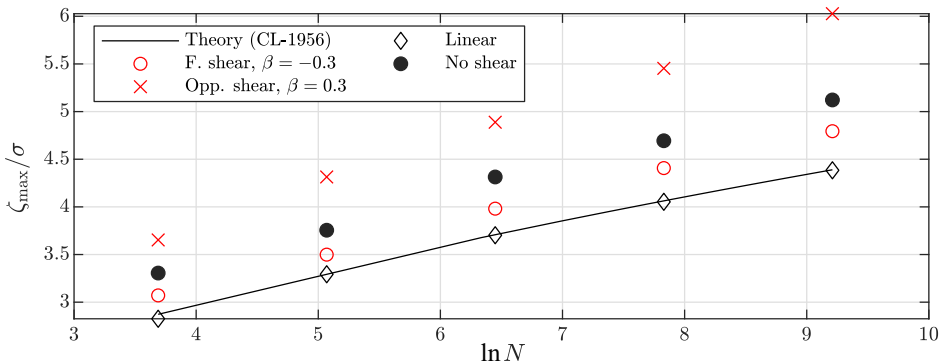


FIG. 5. The average of crest height of scenes containing the largest N waves. In the figure, the theoretical predictions (the black solid line) are based on Eq. (38) for linear waves.

of narrow bandwidth seems to lead to larger overestimate for opposing shear compared to the case of a following shear.

C. The distribution of maximum wave crest

Consider next the distribution of the height of the highest wave crest among a randomly chosen sequence of N consecutive waves, where a “wave” in this context is a time interval wherein the surface elevation contains one maximum and one minimum. A long time ago Longuet-Higgins [21] derived an expression for maximum wave crest distribution based on linear waves with a narrow band frequency spectrum. Cartwright and Longuet-Higgins [87] extended the theory to allow for a broadband spectrum, still in the linear wave regime. More recently, the Gumbel distribution was used to solve this problem up to second order [75,93,95]; for a linear narrow-band process, the expressions in these references are the same. In this section we use the expression from Cartwright and Longuet-Higgins [87] for comparison:

$$\frac{\zeta_{\max}}{\sigma} = \sqrt{2 \ln[(1 - \nu^2)^{\frac{1}{2}} N]} + \gamma_E / \sqrt{2 \ln[(1 - \nu^2)^{\frac{1}{2}} N]}, \quad (38)$$

where ζ_{\max} is the maximum crest height from a continuous wave train, $\gamma_E \approx 0.5772$ is Euler’s constant.

Figure 5 gives the comparison of largest crest height between our numerical results and Eq. (38). Each point is obtained as follows: a time series containing 2×10^6 waves is divided into 160 segments. From each segment a sequence of N consecutive waves is chosen randomly from which the highest crest is found, then the average is taken over all the highest crests and plotted in the figure. Figure 5(a) shows that, once again, our simulated results of linear wave fields fit well with the theoretical solution.

Compared with linear results, second order corrections make a considerable contribution to largest-crest heights. The largest crest heights rise by around 10% to 20%. A similar phenomenon was observed by Socquet-Juglard *et al.* [75], who used a narrow-band frequency spectrum and found the largest crest heights of a nonlinear wave field increased by about 20% compared with linear wave fields. Moreover, it is clear that the additional presence of subsurface shear also has noticeable influence on largest crest heights. The opposing and following shear current increase or decrease the largest crest heights by about 18% or 8%, respectively for the case with $\beta = 0.3$ and $\beta = -0.3$, compared with the case with no shear current. Note that the comment at the end of the previous section still applies: the current will often change a free wave surface in such a way that in absolute terms, the crest heights are actually increased by opposing shear, which typically corresponds to a following current in the earth-fixed frame of reference, and vice versa.

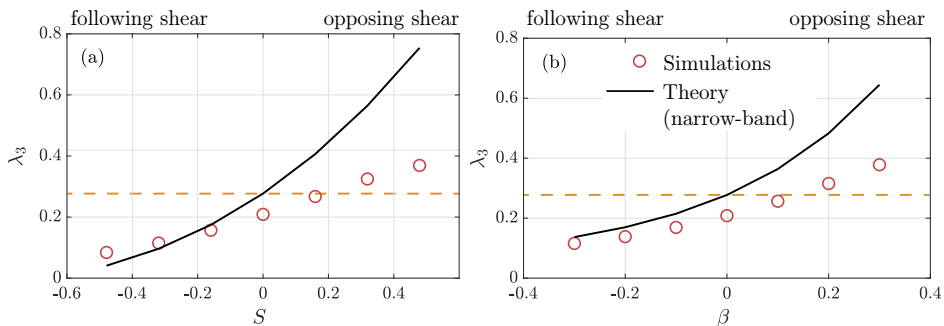


FIG. 6. Skewness of the wave surface elevation for the cases with a linear shear current (a) and exponential shear current (b). The narrow-band theoretical predictions in solid black lines are based on Eq. (23b). The dashed line is the no-shear case, for reference.

D. Skewness

In this section, we discuss the influence of a shear current on skewness, which is a measure of the wave spectrum’s asymmetry. Unlike skewness, kurtosis is not expected to be well approximated by second-order theory, and therefore not included in this paper.

Skewness of second-order waves can be expressed as a function of wave steepness, which is given by Eq. (23) in the limiting case of a narrow-band wave spectrum. The skewness should generally depend on both the bandwidth parameter (ν) and spectrum shape, as has been shown by Srokosz and Longuet-Higgins [71].

We consider two types of shear currents, as given in Eqs. (33a) and (33b). From the point of view of the waves, which can “feel” the current only down to about half a wavelength’s depth, the significant difference is that a linear current has the same shear at all depths, affecting the wave dispersion for all wavelengths, whereas the exponential profile is felt strongly by the short waves with $k \gtrsim \alpha k_{p,0}$ and hardly at all for long waves $k \ll \alpha k_{p,0}$.

Figures 6(a) and 6(b) show the skewness of linear and exponential shear current cases, respectively, calculated according to its definition given by Eq. (22b). The theoretical predictions in solid blue lines are based on Eq. (23b) with the assumption of narrow-band waves in both the absence (i.e., $S = 0$ and $\beta = 0$ in Figs. 6(a) and 6(b), respectively) and presence of a shear current. For both linear shear and exponential shear cases the skewness increases monotonically with S and β , respectively. In the range of shear strengths examined in Fig. 6, the skewness always remains positive. The strongest shear current enhances the skewness by about 86% compared with the cases in the absence of a shear current. The narrow-band assumption for the cases with an exponential shear current always leads to an overestimate of the skewness, compared with the numerical simulations due to the theory in Sec. II applicable to arbitrary bandwidth. In contrast, it may lead to underestimated values for the linear shear and following current cases in the regime where $S \leq -0.2$. The inaccuracy introduced by the narrow-band assumption is obvious, which may arise because the JONSWAP spectrum chosen is not very narrow and the strong profile shear can lead to a considerable change in the wavelength of all waves prescribed on the JONSWAP spectrum.

E. The mouth of the Columbia River

As a real-life example we consider the real measured data described in Sec. IV B 2 to demonstrate and quantify the significant misprediction of wave statistics that would result from neglecting the current’s vertical shear. The currents considered, adapted from Fig. 3 of Zippel and Thomson [54] are shown in Fig. 8(a), using the same color coding as in said figure. The surface current was subtracted and the profiles extended to the surface as explained in section IV B 2. As input wave

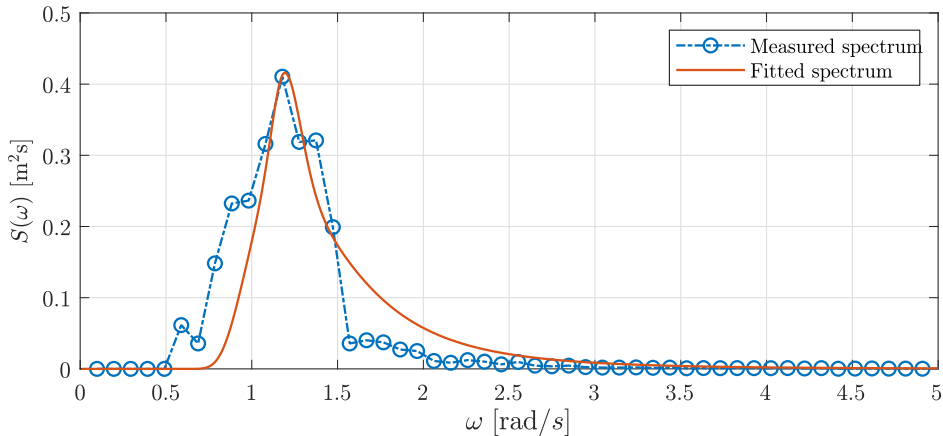


FIG. 7. Power energy spectrum for the Columbia River wave data.

spectrum we fit a JONSWAP spectrum with bandwidth parameter $\nu = 0.6618$ to a representative example among the many wave spectra measured by Zippel and Thomson [54], shown in Fig. 7. The fit is not excellent, but sufficient to provide a representative example.

Figure 1(d) shows the weak-shear parameter $\delta(\omega)$ when ω is the given parameter; we argue in Appendix E that the appropriate value in this case is $\delta_\omega(\omega) = 2\delta(\omega^2/g)$ where $\delta(k)$ is defined in Eq. (35).

1. Skewness

The skewness of simulated results with Columbia River current data are given in Fig. 8(b), where k_p is the dimensionless peak wave number which depends on the shear current as aforementioned. We chose to use k_p as a representation of the shear strength as it expresses the amount by which the shear changes the wavelength of the wave with peak frequency.

Failure to take into account the presence of shear causes overprediction of skewness by $\approx 24\%$ or underprediction by $\approx 13\%$ during ebb and flood, respectively, as is shown in Fig. 8. Absolute numbers provided by a second-order theory like ours carry significant uncertainty, particularly when

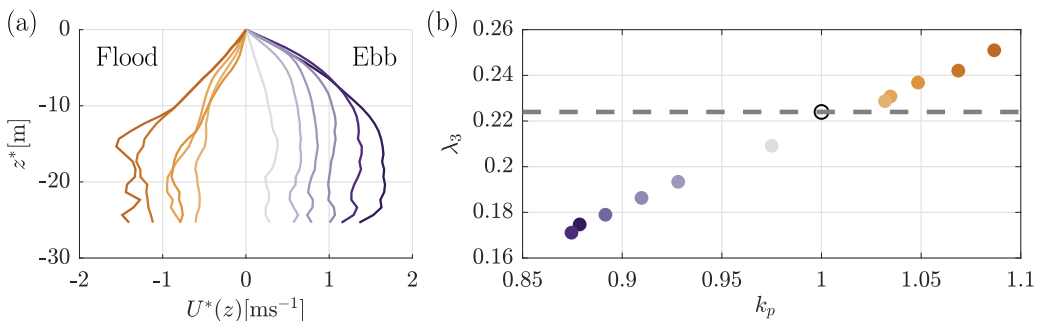


FIG. 8. Skewness of wave surface elevation with Columbia River current and wave spectrum data. (a) Considered current profiles, reproduced with kind permission from Fig. 3 of Ref. [54] with the same color coding, shifted to the surface level and with surface current subtracted. (b) Numerically obtained skewness for the measured wave spectrum of Ref. [54] on the currents in panel (a), with corresponding color coding; the ascissa is the shear-shifted peak wave number with $k_p = 1$ corresponding to zero shear (open circle).

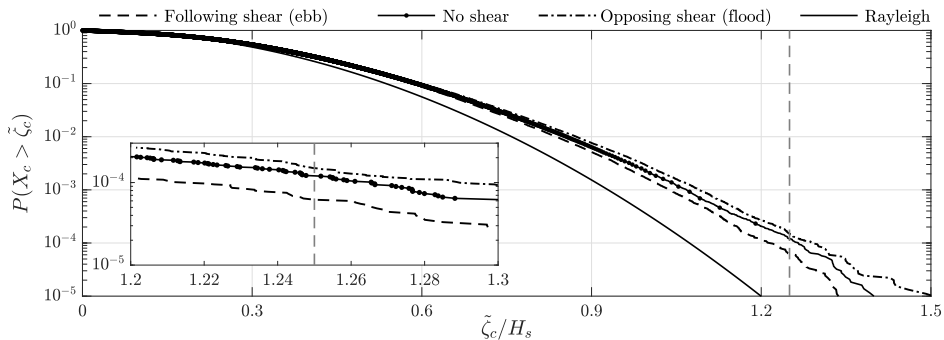


FIG. 9. Exceedance probability of simulated results with the current measured by Zippel and Thomson [54] in the Columbia River (CR) shown in Fig. 1(c), equal to the strongest currents in either direction in Fig. 8(a). The profiles of the following and opposing CR-current are shown in Fig. 1(c).

the spectrum is not narrow, but show a clear and consistent trend. Held together with Zippel and Thomson’s conclusion that wave steepness can be mispredicted by $\pm 20\%$ in these waters in the same conditions if shear is not accounted for [54], there is compelling evidence that shear can be highly significant to the estimation of wave statistics from measured spectra.

2. Rogue wave probability

We also carried out simulations with data from Columbia River using both the wave spectrum and shear profiles measured in this location by Zippel and Thomson [54]. As usual, rogue wave probability is defined as the probability of crests exceeding $1.25H_s$.

As observed for the model currents in Fig. 4, opposing shear enhances the crest heights of large waves while following shear weakens them, leading to increased and decreased exceedance probability, respectively, which is shown in Fig. 9. The rogue wave probability on opposing shear (i.e., a following surface current during ebb) is increased by 36% while on following shear (opposing surface current, during flow) it is decreased by 45%; from 1.12×10^{-4} to 6.20×10^{-5} and 1.52×10^{-4} , respectively. Given that our theory is second order only, these numbers are not quantitatively accurate, but show clearly that shear currents must be accounted for in prediction and modeling of extreme waves.

Note carefully that the rogue wave probability is the probability of *surprisingly* high waves, as discussed by Hjelmerik and Trulsen [30]. Although rogue waves are more than twice as probable on the wave-following flow current than the wave-opposing ebb current, the significant wave height itself is typically much greater in the former case (more than twice as high in the conditions measured in Ref. [54], for instance), making for rougher conditions overall. The effect of shear is to reduce the prevalence of very large waves during ebb, a beneficial effect with respect to sealoads and maritime safety.

VI. CONCLUSIONS

In this paper, we develop the second-order (deterministic) theory using perturbation expansion, which is extended from Longuet-Higgins [11] to allow for a depth-dependent background flow whose profile shear can be strong. The new theory can be used to investigate the wave-current interaction and applicable to waves of an arbitrary bandwidth. The linear wave field is solved with the DIM method proposed by Li and Ellingsen [47]. We derived a boundary value problem for the second-order waves, which can be solved numerically. With the additional assumption of narrow-band waves, a second-order accurate statistical model is derived for the skewness,

probability density function of surface elevation, and the probability distribution of wave crest, which have accounted for the presence of a depth-dependent background flow.

We carried out numerical simulations for the analysis of wave statistics and examined effects of a shear current. We used a JONSWAP spectrum and several different shear currents as input to generate linear random waves. The second-order waves are solved for numerically based our newly derived theory. The measured wave spectrum and currents from Columbia River by Zippel and Thomson [54] were also used in our simulations.

For linear wave fields the probability distribution of wave surface elevation and wave maxima and average maximum wave crest all coincide with theoretical expressions well as expected. The nonlinear wave fields show similar properties compared with well-known second-order Stokes waves. The wave crests are higher and troughs are flatter than linear wave fields. As a result, the positive tails of the probability density function for wave surface elevation and wave maxima from nonlinear wave fields are longer than linear wave fields while the negative tails of surface elevation are shorter. Also, the largest wave crests in nonlinear wave fields are substantially greater. We found that the opposing shear currents can strengthen such “nonlinear properties” while the following shear currents can weaken them.

We also found that the additional assumption of narrow-band waves leads to in general negligible and pronounced differences for the following- and opposing-shear case, respectively, when comparing the second-order statistical model with the more general deterministic theory which is applicable to waves with an arbitrary bandwidth.

ACKNOWLEDGMENTS

Z.B.Z. acknowledges the support from China Scholarship Council through Project No. 201906060137. Y.L. is supported by the Research Council of Norway (RCN) through the FRIPRO mobility Project No. 287389. S.Å.E. is supported by the European Research Council Consolidator Grant No. 101045299 (*WaTurSheD*), and RCN Grant No. 325114 (*iMod*). We thank Dr. Seth Zippel and Professor Jim Thomson for the use of the data collected from the Data Assimilation and Remote Sensing for Littoral Applications (DARLA) project and the Rivers and Inlets (RIVET) program (see, e.g., Ref. [54] for details). See Supplemental Material [65] for the computer code (MATLAB) used to generate our data. We thank the anonymous referees for their valuable suggestions and comments which have improved the quality of the paper.

APPENDIX A: FLOW DIAGRAM OF NUMERICAL IMPLEMENTATIONS

A flow diagram of the numerical implementation used to generate statistics is shown in Fig. 10.

APPENDIX B: THE FORCING TERMS OF THE RAYLEIGH EQUATION

With the linear wave fields given by Eqs. (11a), (11b), and (11c), the nonlinear forcing terms in Eq. (14c) are expressed as

$$\hat{\mathcal{N}}_{\pm}^{(2)} = [\mathbf{k}_{\pm} \cdot \partial_z \mathbf{N}_{h,\pm} + k_{\pm}^2 N_{Rz,+}] \cos \psi_{\pm}, \quad (\text{B1a})$$

$$\hat{\mathcal{F}}_{\pm}^{(2)} = [k_{\pm}^2 N_{F1,\pm} - N_{F2,\pm} + N_{F3,\pm} - N_{F4,\pm} - (\mathbf{U} \cdot \mathbf{k}_{\pm} - \omega_{\pm}) \mathbf{k}_{\pm} \cdot \mathbf{N}_{h,+}] \sin \psi_{\pm}, \quad (\text{B1b})$$

with $\psi_{\pm} = \psi_1 \pm \psi_2$, $\mathbf{N}_{h,i} = [N_{Rx,i}, N_{Ry,i}]$,

$$\begin{bmatrix} N_{Rx,\pm} \\ N_{Ry,\pm} \\ N_{Rz,\pm} \end{bmatrix} = \frac{1}{2} \begin{bmatrix} -(k_{1x} \hat{u}_1^{(1)} \hat{u}_2^{(1)} \pm k_{2x} \hat{u}_2^{(1)} \hat{u}_1^{(1)} + k_{1y} \hat{u}_1^{(1)} \hat{v}_2^{(1)} \pm k_{2y} \hat{u}_2^{(1)} \hat{v}_1^{(1)} \mp \hat{u}_1^{(1)'} \hat{w}_2^{(1)} - \hat{u}_2^{(1)'} \hat{w}_1^{(1)}) \\ -(k_{1x} \hat{v}_1^{(1)} \hat{u}_2^{(1)} \pm k_{2x} \hat{v}_2^{(1)} \hat{u}_1^{(1)} + k_{1y} \hat{v}_1^{(1)} \hat{v}_2^{(1)} \pm k_{2y} \hat{v}_2^{(1)} \hat{v}_1^{(1)} \mp \hat{v}_1^{(1)'} \hat{w}_2^{(1)} - \hat{v}_2^{(1)'} \hat{w}_1^{(1)}) \\ k_{x1} \hat{w}_1^{(1)} \hat{u}_2^{(1)} + k_{x2} \hat{w}_2^{(1)} \hat{u}_1^{(1)} + k_{y1} \hat{w}_1^{(1)} \hat{v}_2^{(1)} + k_{y2} \hat{w}_2^{(1)} \hat{v}_1^{(1)} \mp \hat{w}_1^{(1)'} \hat{w}_2^{(1)} \mp \hat{w}_1^{(1)} \hat{w}_2^{(1)'} \end{bmatrix}, \quad (\text{B2a})$$

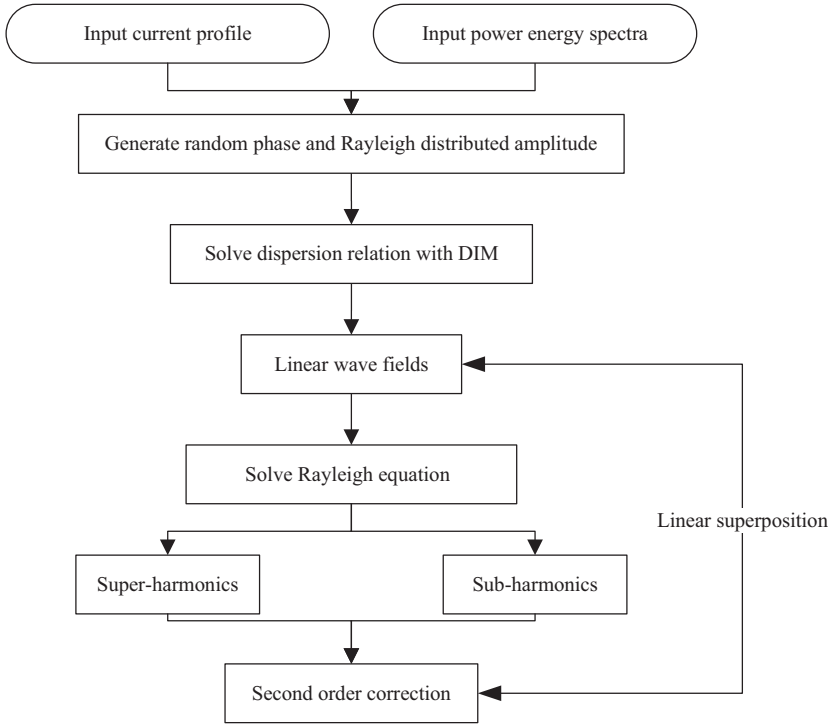


FIG. 10. Numerical procedures of the simulation.

and

$$N_{F1\pm} = -\frac{1}{2}(k_{1x}\hat{u}_2^{(1)}\hat{\zeta}_1^{(1)} + k_{1y}\hat{v}_2^{(1)}\hat{\zeta}_1^{(1)} \pm k_{2x}\hat{u}_1^{(1)}\hat{\zeta}_2^{(1)} \pm k_{2y}\hat{v}_1^{(1)}\hat{\zeta}_2^{(1)}), \quad (\text{B3a})$$

$$N_{F2\pm} = \frac{1}{2}(\mathbf{k}_1^2(\mathbf{k}_1 \cdot \mathbf{U} - \omega_1)\hat{\zeta}_2^{(1)}\hat{P}_1^{(1)'} \pm \mathbf{k}_2^2(\mathbf{k}_2 \cdot \mathbf{U} - \omega_2)\hat{\zeta}_1^{(1)}\hat{P}_2^{(1)'}), \quad (\text{B3b})$$

$$N_{F3\pm} = -\frac{1}{2}(\mathbf{k}_1^2\hat{\zeta}_2^{(1)}\hat{w}_1^{(1)'} \pm \mathbf{k}_2^2\hat{\zeta}_1^{(1)}\hat{w}_2^{(1)'}), \quad (\text{B3c})$$

$$N_{F4\pm} = \frac{1}{2}(\mathbf{k}_1^2\mathbf{k}_1 \cdot \mathbf{U}'\hat{P}_1^{(1)}\hat{\zeta}_2^{(1)} \pm \mathbf{k}_2^2\mathbf{k}_2 \cdot \mathbf{U}'\hat{P}_2^{(1)}\hat{\zeta}_1^{(1)}), \quad (\text{B3d})$$

where $\mathbf{k}_1 = [k_{1x}, k_{1y}]$ and $\mathbf{k}_2 = [k_{2x}, k_{2y}]$

APPENDIX C: ANALYTICAL SOLUTION FOR LINEARLY SHEARED CURRENT

We assume the shear profile is given by $\mathbf{U} = (S_0z, 0)$. The linear solution can be easily solved, which is expressed as [32,38]

$$\hat{w}^{(1)}(\mathbf{k}, z) = \hat{w}_0^{(1)}(\mathbf{k})e^{kz}, \quad (\text{C1a})$$

$$\hat{\mathbf{u}}^{(1)}(\mathbf{k}, z) = i \frac{k^2 \mathbf{U}' + [(\mathbf{U} \cdot \mathbf{k} - \omega)k - k_x S_0] \mathbf{k}}{(\mathbf{U} \cdot \mathbf{k} - \omega)k^2} \hat{w}_0^{(1)} e^{kz}, \quad (\text{C1b})$$

$$\hat{P}^{(1)}(\mathbf{k}, z) = -i \frac{(\mathbf{U} \cdot \mathbf{k} - \omega)k - k_x S_0}{k^2} \hat{w}_0^{(1)} e^{kz}, \quad (\text{C1c})$$

$$\hat{w}_0^{(1)}(\mathbf{k}) = -i \hat{\zeta}^{(1)}(\mathbf{k}) \omega, \quad (\text{C1d})$$

where $\mathbf{k} = (k_x, k_y)$, $k = \sqrt{k_x^2 + k_y^2}$ and the subscript “0” denotes the evaluation at a undisturbed surface $z = 0$. The dispersion relation for linear waves in a linearly sheared current is given by [32,38]

$$\omega = -\frac{S_0 k_x}{2k} \pm \sqrt{k + \frac{S_0^2 k_x^2}{4k^2}}, \quad (\text{C2})$$

where “+” and “-” denotes the waves propagating “downstream” and “upstream” relative to the current, respectively.

Substituting the linear solution into the forcing terms of second-order equations (17), we obtain an inhomogeneous boundary value problem for the second-order vertical velocity $w^{(2)}$. The general solution to this boundary value problem in Fourier space has the form

$$\hat{w}_{\pm}^{(2)}(\mathbf{k}_1, \mathbf{k}_2, z) = B_{1\pm}(\mathbf{k}_1, \mathbf{k}_2)e^{k_{\pm}z} + \hat{w}_{\text{cross}}(\mathbf{k}_1, \mathbf{k}_2, z), \quad (\text{C3})$$

where the deepwater boundary condition was used, the first term on the right-hand side of the equation is due to the forcing at a still water surface and the homogeneous Rayleigh equation, and \hat{w}_{cross} is a particular solution of the inhomogeneous Rayleigh equation given by [38]

$$\hat{w}_{\text{cross}}(\mathbf{k}_1, \mathbf{k}_2, z) = -\frac{i}{2k_{\pm}} \frac{\hat{w}_{0,1}^{(1)} \hat{w}_{0,2}^{(1)}}{k_{\pm x} S_0} \frac{k_{1x} k_{2y} - k_{1y} k_{2x}}{k_1 k_2} e^{(k_1 + k_2)z} \sum_{i,j=1}^3 \left[\frac{\pm b_{ij}}{(\xi_i - z)^{j-1}} \tilde{E}_j[k_{\pm}(\xi_i - z)] \right], \quad (\text{C4})$$

with $\hat{w}_{0,j}^{(1)} = \hat{w}_0^{(1)}(\mathbf{k}_j)$ for $j = 1$ and $j = 2$,

$$b_{ij} = \sum_{m=j}^3 \frac{-a_{im}}{(\xi_i - \xi_3)^{m-j+1}}, \quad i = 1, 2; \quad b_{31} = -b_{11} - b_{21}; \quad b_{32} = b_{33} = 0, \quad (\text{C5a})$$

$$\xi_1 = \frac{\omega_1}{k_{1x} S_0}, \quad \xi_2 = \frac{\omega_2}{k_{2x} S_0}, \quad \xi_3 = \frac{\omega_{\pm}}{k_x S_0}, \quad (\text{C5b})$$

$$\tilde{E}_j(\mu) = e^{\mu} \mu^{j-1} \int_{\mu}^{\infty} \frac{e^{-\tau}}{\tau^j} d\tau. \quad (\text{C5c})$$

Assuming $\xi_1 \neq \xi_2$, the coefficients in Eq. (C5) are expressed as

$$a_{i1} = (-1)^i \left[k_1 k_2 - \mathbf{k}_1 \cdot \mathbf{k}_2 - \frac{k_1 + k_2}{\xi_1 - \xi_2} \frac{k_{1x} k_{2y} - k_{1y} k_{2x}}{k_1 k_2} \tan \theta_m \right] \tan \theta_i, \quad (\text{C6a})$$

$$a_{i2} = (-1)^i \left[\frac{1}{k_i} \left[k_1 k_2 - \mathbf{k}_1 \cdot \mathbf{k}_2 - \frac{k_i}{\xi_1 - \xi_2} \frac{k_{1x} k_{2y} - k_{1y} k_{2x}}{k_1 k_2} \tan \theta_m \right] \right] \tan \theta_i, \quad (\text{C6b})$$

$$a_{i3} = (-1)^i \frac{k_m}{k_i} \tan \theta_i, \quad (\text{C6c})$$

where $i, m \in \{1, 2\}$ so that $i \neq m$ and $\tan \theta_i = k_{iy}/k_{ix}$. The undetermined coefficients $B_{1\pm}$ is solved by inserting Eq. (C3) into the combined boundary condition (17b). Then, the surface elevation is obtained from Eq. (19).

APPENDIX D: EFFECTS OF CURRENT CONTINUATION ON SKEWNESS

We here compare three alternative, physically reasonable ways in which profiles measured using ADCP can be extended from the shallowest measurement point— $z = -1.35$ m for the Columbia River measurements we use [64]—up to the surface. These are: extrapolation using a polynomial fit, shifting the profile upwards so that the shallowest measurement point is set to surface level (used, *inter alia*, in Refs. [83,96]), and the highly conservative approach of continuing the current profile

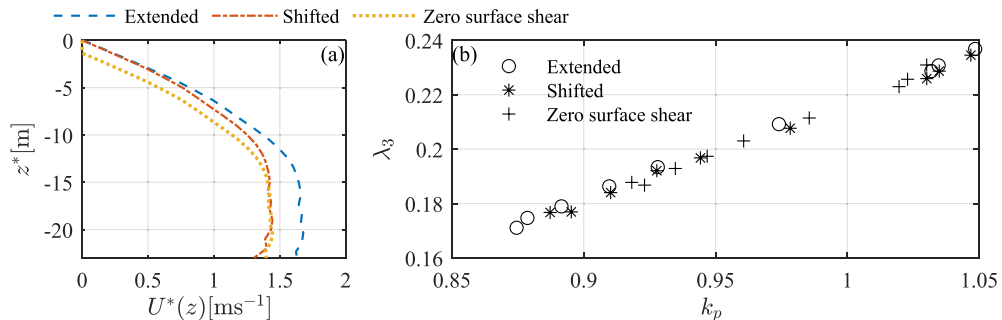


FIG. 11. Skewness of wave surface elevation for different profiles. (a) Comparison of shear profiles with three approaches. (b) Numerically obtained skewness: “o,” extended profiles; “*,” shifted profiles; “+,” zero surface shear profiles. Case chosen is same with Fig. 8 except that two strongest opposing shears are excluded here.

to the surface with zero shear. These are referred as extended profile, shifted profile and zero surface shear profile, respectively and are shown in Fig. 11(a).

We compare wave skewness in these three case, the results are given in Fig. 11. Again, the k_p in Fig. 11(b) is the dimensionless peak wave number as in Fig. 8, where $k_p = 1$ corresponds to the case without shear current whereas the modifications to the dispersion relation due to shear shifts the value. Values $k_p > 1$ correspond to adverse shear and vice versa. A plot of the calculated skewness for the different cases shows that the difference in skewness is hardly discernible.

APPENDIX E: DIMENSIONLESS WEAK-SHEAR PARAMETER FOR GIVEN ω

Let the depth-averaged shear be small, of order a small parameter $\delta \ll 1$. Assuming the wave number k given, Stewart and Joy [55] derived the approximate dispersion relation $\omega(k)$ which may be written [60]

$$\omega^*(k^*) \approx \sqrt{gk^*} [1 - \delta(k^*)] + \mathcal{O}(\delta^2), \quad (\text{E1})$$

with the small-shear parameter $\delta(k^*)$ defined in Eq. (35). It was shown [60] that a sufficient criterion for the Stewart and Joy approximation to be good is that $\delta_\omega \ll 1$.

Conversely (i.e., for given ω^*) the presence of shear modifies k slightly, and we write

$$k^* = k_0^* [1 + \delta_\omega(\omega^*)] + \mathcal{O}(\delta_\omega^2), \quad (\text{E2})$$

with $k_0^* = (\omega^*)^2/g$, and clearly $\delta_\omega \sim \delta$. We seek to find δ_ω . Inserting Eq. (E2) into Eq. (E1) via Eq. (35) and noting that $\sqrt{gk_0^*} = \omega^*$,

$$\omega^* = \omega^* \sqrt{1 + \delta_\omega} [1 - \delta(k_0^*)] + \mathcal{O}(\delta^2) = \omega^* [1 + \frac{1}{2}\delta_\omega - \delta(k_0^*)] + \mathcal{O}(\delta^2). \quad (\text{E3})$$

Internal consistency thus demands

$$\delta_\omega(\omega^*) = 2\delta(k_0^*). \quad (\text{E4})$$

-
- [1] C. Kharif, E. Pelinovsky, and A. Slunyaev, *Rogue Waves in the Ocean* (Springer Science & Business Media, Cham, 2008).
 [2] L. Cavaleri, S. Abdalla, A. Benetazzo, L. Bertotti, J. R. Bidlot, Breivik, S. Carniel, R. E. Jensen, J. Portilla-Yandun, W. E. Rogers, A. Roland, A. Sanchez-Arcilla, J. M. Smith, J. Staneva, Y. Toledo, G. P. van

- Vledder, and A. J. van der Westhuysen, Wave modelling in coastal and inner seas, *Prog. Oceanogr.* **167**, 164 (2018).
- [3] J. M. Dudley, G. Genty, A. Mussot, A. Chabchoub, and F. Dias, Rogue waves and analogies in optics and oceanography, *Nat. Rev. Phys.* **1**, 675 (2019).
- [4] T. B. Benjamin and J. E. Feir, The disintegration of wave trains on deep water: Part 1. Theory, *J. Fluid Mech.* **27**, 417 (1967).
- [5] P. A. E. M. Janssen, Nonlinear four-wave interactions and freak waves, *J. Phys. Oceanogr.* **33**, 863 (2003).
- [6] B. White and B. Fornberg, On the chance of freak waves at sea, *J. Fluid Mech.* **355**, 113 (1998).
- [7] T. Janssen and T. Herbers, Nonlinear wave statistics in a focal zone, *J. Phys. Oceanogr.* **39**, 1948 (2009).
- [8] J. Gao, X. Ma, G. Dong, H. Chen, Q. Liu, and J. Zang, Investigation on the effects of Bragg reflection on harbor oscillations, *Coast. Eng.* **170**, 103977 (2021).
- [9] K. Trulsen, A. Raustøl, S. Jorde, and L. Rye, Extreme wave statistics of long-crested irregular waves over a shoal, *J. Fluid Mech.* **882**, R2 (2020).
- [10] Y. Li, S. Draycott, Y. Zheng, Z. Lin, T. Adcock, and T. van den Bremer, Why rogue waves occur atop abrupt depth transitions, *J. Fluid Mech.* **919**, R5 (2021).
- [11] M. S. Longuet-Higgins, Resonant interactions between two trains of gravity waves, *J. Fluid Mech.* **12**, 321 (1962).
- [12] M. S. Longuet-Higgins, The effect of nonlinearities on statistical distributions in the theory of sea waves, *J. Fluid Mech.* **17**, 459 (1963).
- [13] M. A. Tayfun, Narrow-band nonlinear sea waves, *J. Geophys. Res.* **85**, 1548 (1980).
- [14] M. A. Tayfun, Effects of spectrum band width on the distribution of wave heights and periods, *Ocean Eng.* **10**, 107 (1983).
- [15] M. A. Tayfun, On narrow-band representation of ocean waves: 1. theory, *J. Geophys. Res.: Oceans* **91**, 7743 (1986).
- [16] J. Dalzell, A note on finite depth second-order wave-wave interactions, *Appl. Ocean Res.* **21**, 105 (1999).
- [17] G. Z. Forristall, Wave crest distributions: Observations and second-order theory, *J. Phys. Oceanogr.* **30**, 1931 (2000).
- [18] F. Arena and F. Fedele, A family of narrow-band nonlinear stochastic processes for the mechanics of sea waves, *Eur. J. Mech. B Fluids* **21**, 125 (2002).
- [19] A. A. Toffoli, M. Onorato, A. V. Babanin, E. Bitner-Gregersen, A. R. Osborne, and J. Monbaliu, Second-order theory and setup in surface gravity waves: A comparison with experimental data, *J. Phys. Oceanogr.* **37**, 2726 (2007).
- [20] A. Toffoli, M. Onorato, E. Bitner-Gregersen, A. R. Osborne, and A. V. Babanin, Surface gravity waves from direct numerical simulations of the Euler equations: A comparison with second-order theory, *Ocean Eng.* **35**, 367 (2008).
- [21] M. S. Longuet-Higgins, On the statistical distribution of the height of sea waves, *J. Marine Res.* **11**, 245 (1952).
- [22] P. Petrova, Z. Cherneva, and C. G. Soares, Distribution of crest heights in sea states with abnormal waves, *Appl. Ocean Res.* **28**, 235 (2006).
- [23] F. Fedele and M. A. Tayfun, On nonlinear wave groups and crest statistics, *J. Fluid Mech.* **620**, 221 (2009).
- [24] F. Fedele, J. Herterich, A. Tayfun, and F. Dias, Large nearshore storm waves off the Irish coast, *Sci. Rep.* **9**, 15406 (2019).
- [25] V. I. Shrira and A. V. Slunyaev, Trapped waves on jet currents: Asymptotic modal approach, *J. Fluid Mech.* **738**, 65 (2014).
- [26] V. I. Shrira and A. V. Slunyaev, Nonlinear dynamics of trapped waves on jet currents and rogue waves, *Phys. Rev. E* **89**, 041002(R) (2014).
- [27] D. H. Peregrine, Interaction of water waves and currents, *Adv. Appl. Mech.* **16**, 9 (1976).
- [28] J. R. Stocker and D. H. Peregrine, The current-modified nonlinear Schrödinger equation, *J. Fluid Mech.* **399**, 335 (1999).
- [29] C. W. Curtis, J. D. Carter, and H. Kalisch, Particle paths in nonlinear Schrödinger models in the presence of linear shear currents, *J. Fluid Mech.* **855**, 322 (2018).

- [30] K. B. Hjelmervik and K. Trulsen, Freak wave statistics on collinear currents, *J. Fluid Mech.* **637**, 267 (2009).
- [31] M. Onorato, D. Proment, and A. Toffoli, Triggering Rogue Waves in Opposing Currents, *Phys. Rev. Lett.* **107**, 184502 (2011).
- [32] S. Å. Ellingsen, Oblique waves on a vertically sheared current are rotational, *Eur. J. Mech. B Fluids* **56**, 156 (2016).
- [33] R. A. Dalrymple, A finite amplitude wave on a linear shear current, *J. Geophys. Res.* **79**, 4498 (1974).
- [34] R. Thomas, C. Kharif, and M. Manna, A nonlinear Schrödinger equation for water waves on finite depth with constant vorticity, *Phys. Fluids* **24**, 127102 (2012).
- [35] J. Touboul and C. Kharif, Effect of vorticity on the generation of rogue waves due to dispersive focusing, *Nat. Hazards* **84**, 585 (2016).
- [36] B. Liao, G. Dong, Y. Ma, and J. L. Gao, Linear-shear-current modified Schrödinger equation for gravity waves in finite water depth, *Phys. Rev. E* **96**, 043111 (2017).
- [37] H. C. Hsu, C. Kharif, M. Abid, and Y. Y. Chen, A nonlinear Schrödinger equation for gravity-capillary water waves on arbitrary depth with constant vorticity. Part 1, *J. Fluid Mech.* **854**, 146 (2018).
- [38] A. H. Akselsen and S. Å. Ellingsen, Weakly nonlinear transient waves on a shear current: Ring waves and skewed Langmuir rolls, *J. Fluid Mech.* **863**, 114 (2019).
- [39] A. I. Baumstein, Modulation of gravity waves with shear in water, *Stud. Appl. Math.* **100**, 365 (1998).
- [40] J. N. Steer, A. G. Borthwick, D. Stagonas, E. Buldakov, and T. S. van den Bremer, Experimental study of dispersion and modulational instability of surface gravity waves on constant vorticity currents, *J. Fluid Mech.* **884**, A40 (2020).
- [41] N. Pizzo, L. Lenain, O. Rømcke, S. Å. Ellingsen, and B. K. Smeltzer, The role of Lagrangian drift in the geometry, kinematics, and dynamics of surface waves, *J. Fluid Mech.* **954**, R4 (2023).
- [42] M. Francius and C. Kharif, Two-dimensional stability of finite-amplitude gravity waves on water of finite depth with constant vorticity, *J. Fluid Mech.* **830**, 631 (2017).
- [43] A. Abrashkin and E. Pelinovsky, Lagrange form of the nonlinear Schrödinger equation for low-vorticity waves in deep water, *Nonlin. Processes Geophys.* **24**, 255 (2017).
- [44] A. G. Voronovich, Propagation of internal and surface gravity waves in the approximation of geometrical optics, *Izv. Atmos. Ocean. Phys.* **12**, 850 (1976).
- [45] B. Quinn, Y. Toledo, and V. Shrira, Explicit wave action conservation for water waves on vertically sheared flows, *Ocean Model.* **112**, 33 (2017).
- [46] S. Banihashemi, J. T. Kirby, and Z. Dong, Approximation of wave action flux velocity in strongly sheared mean flows, *Ocean Model.* **116**, 33 (2017).
- [47] Y. Li and S. Å. Ellingsen, A framework for modeling linear surface waves on shear currents in slowly varying waters, *J. Geophys. Res.: Oceans* **124**, 2527 (2019).
- [48] S. Banihashemi and J. T. Kirby, Approximation of wave action conservation in vertically sheared mean flows, *Ocean Model.* **143**, 101460 (2019).
- [49] I. Cummins and C. Swan, Vorticity effects in combined waves and currents, in *Proceedings of the twenty-fourth international conference on Coastal Engineering*, edited by B. L. Edge, pp. 113–127 (1994).
- [50] T. Waseda, T. Kinoshita, L. Cavaleri, and A. Toffoli, Third-order resonant wave interactions under the influence of background current fields, *J. Fluid Mech.* **784**, 51 (2015).
- [51] B. K. Smeltzer, E. Æsøy, and S. A. Ellingsen, Observation of surface wave patterns modified by subsurface shear currents, *J. Fluid Mech.* **873**, 508 (2019).
- [52] F. Ardhuin, Small-scale open ocean currents have large effects on wind wave heights, *J. Geophys. Res.: Oceans* **122**, 4500 (2017).
- [53] F. Ardhuin, L. Marié, N. Rasclé, P. Forget, and A. Roland, Observation and estimation of Lagrangian, Stokes, and Eulerian currents induced by wind and waves at the sea surface, *J. Phys. Oceanogr.* **39**, 2820 (2009).
- [54] S. Zippel and J. Thomson, Surface wave breaking over sheared currents: Observations from the mouth of the Columbia River, *J. Geophys. Res.: Oceans* **122**, 3311 (2017).

- [55] R. H. Stewart and J. W. Joy, HF radio measurements of surface currents, *Deep-Sea Res. Oceanogr. Abstr.* **21**, 1039 (1974).
- [56] R. A. Skop, Approximate dispersion relation for wave-current interactions, *J. Waterw. Port, Coast. Ocean Eng.* **113**, 187 (1987).
- [57] J. T. Kirby and T. Chen, Surface waves on vertically sheared flows: Approximate dispersion relations, *J. Geophys. Res. Oceans* **94**, 1013 (1989).
- [58] V. Zakharov and V. Shrira, Formation of the angular spectrum of wind waves, *Zh. Eksp. Teor. Fiz* **98**, 1941 (1990)[*J. Exp. Theor. Phys.* **71**, 1091 (1990)].
- [59] V. I. Shrira, Surface waves on shear currents: Solution of the boundary-value problem, *J. Fluid Mech.* **252**, 565 (1993).
- [60] S. Å. Ellingsen and Y. Li, Approximate dispersion relations for waves on arbitrary shear flows, *J. Geophys. Res.: Oceans* **122**, 9889 (2017).
- [61] N. J. Laxague, B. K. Haus, D. G. Ortiz-Suslow, C. J. Smith, G. Novelli, H. Dai, T. Özgökmen, and H. C. Graber, Passive optical sensing of the near-surface wind-driven current profile, *J. Atmos. Ocean. Technol.* **34**, 1097 (2017).
- [62] N. J. Laxague, T. M. Özgökmen, B. K. Haus, G. Novelli, A. Shcherbina, P. Sutherland, C. M. Guigand, B. Lund, S. Mehta, M. Alday *et al.*, Observations of near-surface current shear help describe oceanic oil and plastic transport, *Geophys. Res. Lett.* **45**, 245 (2018).
- [63] J. Wu, Sea-surface drift currents induced by wind and waves, *J. Phys. Oceanogr.* **13**, 1441 (1983).
- [64] L. F. Kilcher and J. D. Nash, Structure and dynamics of the Columbia River tidal plume front, *J. Geophys. Res.: Oceans* **115**, C05S90(2010).
- [65] See Supplemental Material at <http://link.aps.org/supplemental/10.1103/PhysRevFluids.8.014801> for the computer code used to generate the results presented in this paper.
- [66] M. J. Tucker, P. G. Challenor, and D. J. T. Carter, Numerical simulation of a random sea: A common error and its effect upon wave group statistics, *Appl. Ocean Res.* **6**, 118 (1984).
- [67] K. Hasselmann, On the nonlinear energy transfer in a gravity-wave spectrum: Part 1. General theory, *J. Fluid Mech.* **12**, 481 (1962).
- [68] D. G. Dommermuth and D. K. P. Yue, A high-order spectral method for the study of nonlinear gravity waves, *J. Fluid Mech.* **184**, 267 (1987).
- [69] B. J. West, K. A. Brueckner, R. S. Janda, D. M. Milder, and R. L. Milton, A new numerical method for surface hydrodynamics, *J. Geophys. Res.: Oceans* **92**, 11803 (1987).
- [70] Y. Li and X. Li, Weakly nonlinear broadband and multi-directional surface waves on an arbitrary depth: A framework, Stokes drift, and particle trajectories, *Phys. Fluids* **33**, 076609 (2021).
- [71] M. A. Srokosz and M. S. Longuet-Higgins, On the skewness of sea-surface elevation, *J. Fluid Mech.* **164**, 487 (1986).
- [72] A. D. D. Craik, Resonant gravity-wave interactions in a shear flow, *J. Fluid Mech.* **34**, 531 (1968).
- [73] K. F. Hasselmann, T. P. Barnett, E. Bouws, H. Carlson, D. E. Cartwright, K. Eake, J. Euring, A. Gicnapp, D. Hasselmann, and P. Kruseman, Measurements of wind wave growth and swell decay during the Joint North Sea Wave Project (JONSWAP), *Dtsch. Hydrogr. Z.* **8**, 1 (1973).
- [74] K. Dysthe, H. Socquet-Juglard, K. Trulsen, H. E. Krogstad, and J. Liu, “Freak” waves and large-scale simulations of surface gravity waves, in *Proceedings of the 14th ‘Aha Huliko’ a Hawaiian Winter Workshop* (University of Hawaii, 2005).
- [75] H. Socquet-Juglard, K. Dysthe, K. Trulsen, H. E. Krogstad, and J. Liu, Probability distributions of surface gravity waves during spectral changes, *J. Fluid Mech.* **542**, 195 (2005).
- [76] M. S. Longuet-Higgins, On the joint distribution of the periods and amplitudes of sea waves, *J. Geophys. Res.* **80**, 2688 (1975).
- [77] Z. Dong and J. T. Kirby, Theoretical and numerical study of wave-current interaction in strongly-sheared flows, *Coast. Eng. Proc.* **1**, 2 (2012).
- [78] E. P. Elias, G. Gelfenbaum, and A. J. Van der Westhuysen, Validation of a coupled wave-flow model in a high-energy setting: The mouth of the Columbia River, *J. Geophys. Res. Oceans* **117** (2012).
- [79] P. Maxwell, B. K. Smeltzer, and S. Å. Ellingsen, The error in predicted phase velocity of surface waves atop a shear current with uncertainty, *Water Waves* **2**, 79 (2020).

- [80] J. Campana, E. Terrill, and T. De Paolo, Observations of surface current and current shear using X-band radar, in *Proceedings of the 11th IEEE/OES Conference on Current, Waves and Turbulence Measurement (CWTM)* (IEEE, 2015), pp. 1–5.
- [81] B. Lund, B. K. Haus, J. Horstmann, H. C. Graber, R. Carrasco, N. J. Laxague, G. Novelli, C. M. Guigand, and T. M. Özgökmen, Near-surface current mapping by shipboard marine X-band radar: A validation, *J. Atmos. Ocean. Technol.* **35**, 1077 (2018).
- [82] V. Kudryavtsev, V. Shrira, V. Dulov, and V. Malinovsky, On the vertical structure of wind-driven sea currents, *J. Phys. Oceanogr.* **38**, 2121 (2008).
- [83] Y. Li, B. K. Smeltzer, and S. Å. Ellingsen, Transient wave resistance upon a real shear current, *Eur. J. Mech. B Fluids* **73**, 180 (2019).
- [84] Y. Goda, *Random Seas and Design of Maritime Structures*, 3rd ed. (World Scientific, Singapore, 2010), Vol. 33.
- [85] P. A. E. M. Janssen, On a random time series analysis valid for arbitrary spectral shape, *J. Fluid Mech.* **759**, 236 (2014).
- [86] F. Barbariol, J.-R. Bidlot, L. Cavaleri, M. Sclavo, J. Thomson, and A. Benetazzo, Maximum wave heights from global model reanalysis, *Prog. Oceanogr.* **175**, 139 (2019).
- [87] D. E. Cartwright and Longuet-Higgins, The statistical distribution of the maxima of a random function, *Proc. R. Soc. London A* **237**, 212 (1956).
- [88] S. O. Rice, Mathematical analysis of random noise, *Bell Syst. Tech. J.* **23**, 282 (1944).
- [89] R. E. Haring, A. R. Osborne, and L. P. Spencer, Extreme wave parameters based on continental shelf storm wave records, in *Proceedings of the 15th Coastal Engineering Conference* (1976), pp. 151–170.
- [90] D. L. Kriebel and T. H. Dawson, Nonlinearity in wave crest statistics, in *Proceedings of the 2nd International Conference on Wave Measurement and Analysis* (1993), pp. 61–75.
- [91] N. E. Huang, L. F. Bliven, S. R. Long, and C.-C. Tung, An analytical model for oceanic whitecap coverage, *J. Phys. Oceanogr.* **16**, 1597 (1986).
- [92] D. Kriebel and T. Dawson, Nonlinear effects on wave groups in random seas, *J. Offshore Mech. Arct. Eng.* **113**, 142 (1991).
- [93] M. Prevosto, H. Krogstad, and A. Robin, Probability distributions for maximum wave and crest heights, *Coast. Eng.* **40**, 329 (2000).
- [94] K. Dysthe, H. E. Krogstad, and P. Muller, Oceanic rogue waves, *Annu. Rev. Fluid Mech.* **40**, 287 (2008).
- [95] H. E. Krogstad, J. Liu, H. Socquet-Juglard, K. B. Dysthe, and K. Trulsen, Spatial extreme value analysis of nonlinear simulations of random surface waves, in *Proceedings of the 23rd International Conference on Offshore Mechanics and Arctic Engineering* (ASME, 2004), Vol. 2, pp. 285–295, paper no. OMAE2004-51336, <https://doi.org/10.1115/OMAE2004-51336>.
- [96] B. K. Smeltzer and S. Å. Ellingsen, Surface waves on currents with arbitrary vertical shear, *Phys. Fluids* **29**, 047102 (2017).

Article II

**Dispersive wave focusing on a shear current. Part 1:
Linear approximations**

Simen Å. Ellingsen, Zibo Zheng, Malek Abid, Christian
Kharif, Yan Li

Submitted to: Water Waves

1 Dispersive wave focusing on a shear current.

2 Part 1: Linear approximations

3 Simen Å. Ellingsen^{1*†}, Zibo Zheng^{1†}, Malek Abid², Christian
4 Kharif² and Yan Li³

5 ¹Department of Energy and Process Engineering, Norwegian
6 University of Science and Technology, Trondheim, 7491, Norway.

7 ² Institut de Recherche sur les Phénomènes Hors Equilibre,
8 Aix-Marseille Université, Marseille, 13384, France.

9 ³Department of Mathematics, University of Bergen, Bergen,
10 5007, Norway.

11 *Corresponding author(s). E-mail(s): simen.a.ellingsen@ntnu.no;

12 †SÅE and ZZ are to be considered joint first authors.

13 **Abstract**

14 We consider the evolution and kinematics during dispersive focusing,
15 for a group of waves propagating atop currents varying with depth.
16 Our analysis assumes long-crested linear waves propagating at arbitrary
17 angles relative to the current. Although low steepness is assumed,
18 the linear model is often a reasonable approximation for understanding
19 rogue waves. A number of analytical approximate relations are derived
20 assuming different sub-surface current profiles, including linearly varying
21 current, exponentially varying current, and currents of arbitrary depth
22 profile which are weakly sheared following the approximation of Stewart
23 & Joy (*Deep Sea Res. Abs.* **21**, 1974). The orbital velocities are likewise
24 studied. While shear currents have modest influence on the motion
25 of the envelope of the wave group, they significantly change wave kinematics.
26 Horizontal orbital velocities are either amplified or suppressed
27 depending on whether the shear is opposing or following, respectively.
28 To illustrate these phenomena we consider a real-world example using
29 velocity profiles and wave spectra measured in the Columbia River
30 estuary. Near the surface at the point where focusing occurs, horizontal
31 orbital velocities are respectively increased and decreased by
32 factors of **1.4** and **0.7** for focusing groups propagating on following and

2 *Wave focusing on a shear current*

33 opposing shear (respectively upstream and downstream in the earth-
34 fixed reference system). The implications for the forces a focusing wave
35 group can exert on vessels and installations are profound, emphasizing
36 the importance of considering current profiles in maritime operations.

37 **Keywords:** Wave-shear current interaction, Focused wave group, Wave
38 kinematics

39 **1 Introduction**

40 Rogue waves, characterized as enormous and abrupt waves appearing on the
41 sea's surface, pose a significant threat to maritime activities. These waves
42 which are defined by being far higher than the waves around them, can emerge
43 without warning, occurring both in deep and shallow waters, and they result
44 from various physical mechanisms that concentrate the energy of water waves
45 into a small area. Their occurrence has led to numerous fatalities, injuries, and
46 extensive damages to ships and maritime structures. Among the mechanisms
47 responsible for their formation are dispersive focusing, refraction influenced
48 by variable currents and bottom topography, modulational instability, con-
49 structive wave interference enhanced by second-order interactions, cross-sea
50 interactions, and soliton interactions. For a comprehensive review of these
51 mechanisms, refer to the works by Kharif & Pelinovsky [1], Dysthe *et al.* [2],
52 and Onorato *et al.* [3].

53 The main objective of this paper is to analyze the effect of depth-dependent
54 underlying currents on the dispersive focusing of water waves in deep water.
55 Extreme wave events resulting from dispersive focusing or spatiotemporal
56 focusing phenomena can be described as follows: when initially shorter wave
57 packets are positioned in front of longer wave packets with higher group vel-
58 ocities, the longer waves eventually catch up and overtake the shorter waves
59 during the dispersive evolution process. At a fixed location (known as the focus
60 point) and time, the superposition of all these waves leads to the formation
61 of a large-amplitude wave. Subsequently, the longer waves move ahead of the
62 shorter waves, resulting in a decrease in the amplitude of the wave train. In
63 the absence of vorticity, giant waves created by dispersive focusing have been
64 frequently studied experimentally [4–7] and theoretically [8, 9], but studies in
65 the presence of a shear current are very scarce. Kharif *et al.* [10] investigated
66 the effect of a constant vorticity underlying current on the dispersive focus-
67 ing of a one-dimensional nonlinear wave group propagating in shallow water.
68 Their findings revealed that the presence of constant vorticity increases the
69 maximum amplification factor of the surface elevation as the shear intensity
70 of the current increases. The duration of extreme wave events follows a similar
71 behavior. In narrowband assumption Xin *et al.* [11] report the different effects
72 of following and opposing shear current on both the extreme and fatigue loads
73 on fixed-bottom offshore slender structures in extreme wave events. The work

74 has shed light on the shear-current modified wave kinematics in the design of
 75 offshore structures, which will be explored further in this work as explained
 76 below.

77 This study is the first part of an investigation of waves focusing dispersively
 78 on vertically sheared currents. The, in some respects, simplest case is treated in
 79 this first part, where the theory is linearised with respect to wave steepness; a
 80 second-order theory is found in part two [12]. Although nonlinear wave effects
 81 are significant for rogue wave situations, a linear approximation has been found
 82 to give reasonable results [13]. Our focus is on investigating the behavior of
 83 focusing wave groups propagating obliquely to the current direction, as well
 84 as wave groups traveling in the same direction as the current, in deep water
 85 (see Figure 1). By analyzing the impact of these depth-dependent underlying
 86 currents on the dispersive focusing of water waves, we aim to enhance our
 87 understanding of the formation and characteristics of rogue waves, contributing
 88 to improved safety measures for maritime activities as highlighted in [11].

89 We consider a range of vertically sheared currents, and of wave shapes
 90 at focus, deriving a series of closed-form approximate results. The currents
 91 we consider include the linear and exponential depth dependence — cases for
 92 which closed-form solutions exist for the linear velocity field — and arbitrary
 93 current profiles which satisfy the weak-shear approximation (fundamentally
 94 that required for the celebrated approximation of Stewart & Joy [14]). Wave
 95 groups focusing to a δ -function singularity, and a narrowband Gaussian packet,
 96 are considered. The approximate formulae derived are, we propose, useful for
 97 their relative simplicity and analytical tractability, for instance for the creation
 98 of focusing waves on sheared currents in numerical and laboratory experiments
 99 (see, e.g., [15]).

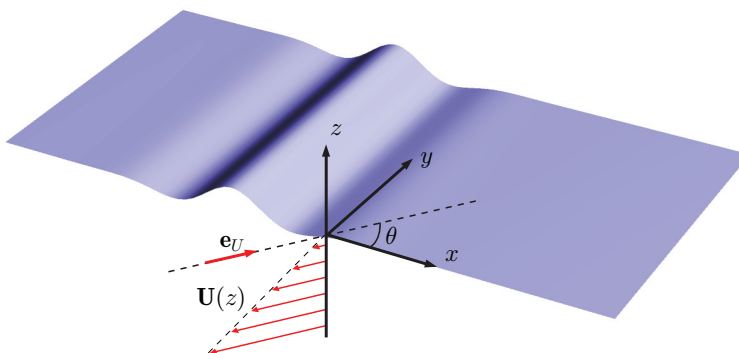


Fig. 1 Geometry: a quasi-2D wave propagating along the x axis. A sub-surface shear current makes an angle θ with the direction of wave propagation. Here $\mathbf{U}(z) = Sz\mathbf{e}_U$. Currents with opposing and following shear are denoted by $\theta \in [0, \pi/2)$ and $(\pi/2, \pi]$, respectively.

100 A main conclusion of our work, illustrated and quantified through many
 101 examples, is the following: within a linear framework, the presence of shear has
 102 modest effect on the focusing and defocusing of the wave-group envelope, but

103 a large effect on the wave kinematics. The component of the orbital velocities
104 near the surface at the point of focus can be strongly enhanced.

105 **2 Theoretical background**

106 In this section we review the necessary background theory and phrase it in the
107 formalism we use herein. While not in a strict sense novel, the reexamination
108 of the basics sheds important light on the mechanisms in play which we will
109 refer extensively to in later sections. After defining the problem and geometry,
110 the linear initial-value solution is provided in a suitable form, and standard
111 current profiles and highly useful approximations are briefly recapitulated.

112 **2.1 Problem definition**

113 We consider a body of water with a free surface which, when undisturbed, is at
114 $z = 0$, and sustaining a shear current which depends arbitrarily on depth. The
115 depth is infinite (some results are generalised to allow finite depth in Appendix
116 A), and we ignore the effects of surface tension. The geometry is sketched in
117 figure 1. The background current has the form

$$\mathbf{U}(z) = \{U_x(z), U_y(z)\} = U(z)\mathbf{e}_U; \quad (1)$$

$$\mathbf{e}_U = \{\cos \theta, \sin \theta\}, \quad (2)$$

118 where \mathbf{e}_U is a unit vector in the xy plane. Without loss of generality we choose
119 the coordinate system which follows the surface of the water so that $U(0) = 0$.
120 As well as simplifying the formalism this choice emphasizes that the effects
121 studies are due to shear rather than surface current. A nonzero surface current
122 is easily worked back into solutions by adding a Doppler shift to frequencies.
123 The angle between wave propagation and current is θ and we shall assume
124 without loss of generality that the wave propagates along the x axis so that
125 $\mathbf{k} \cdot \mathbf{U} = kU_x = kU(z) \cos \theta$. In derivations we shall often retain a general wave
126 vector $\mathbf{k} = \{k_x, 0\}$. We allow k_x to take both signs in derivations, eventually
127 arriving at expressions for waves propagating only in the positive x direction,
128 whereupon we may consider only positive wave numbers. We assume long-
129 crested waves, so the surface elevation is $\zeta(\mathbf{r}, t) = \zeta(x, t)$ where $\mathbf{r} = (x, y)$.
130 We assume here that the current does not change direction with depth, but
131 generalisation to a z -dependent θ is straightforward.

132 As is well known (e.g. [16]), the surface elevation and dispersion relation
133 depend only on \mathbf{U} in the combination $\mathbf{k} \cdot \mathbf{U} = kU_x$, whereas U_y has no influence
134 on ζ . The angle θ thus only plays the role of varying U_x through values between
135 $-U$ and U . We shall see in section 4 that the same is not the case for the
136 velocity field beneath the waves.

137 In this paper we linearise equations and boundary conditions with respect
138 to ζ and its derivatives, as well as orbital velocities — a companion paper
139 considers weakly nonlinear extensions.

140 2.2 Linear initial-value problem, and solution

141 We will solve initial value problems in this set-up, a simpler, long-crested
 142 version of the theory presented in [17]. The general linear solution can be writ-
 143 ten in Fourier form with the 3D formulae in Ref. [17] assuming translational
 144 symmetry in the y direction, as

$$\zeta(\mathbf{r}, t) = \int_{-\infty}^{\infty} \frac{dk_x}{2\pi} \left[b_+(k_x) e^{-i\omega_+(k_x)t} + b_-(k_x) e^{-i\omega_-(k_x)t} \right] e^{ik_x x} \quad (3)$$

145 where $\omega_{\pm}(\mathbf{k})$ are the two solutions of the linear dispersion relation for a general
 146 wave vector \mathbf{k} , and $b_{\pm}(\mathbf{k}) = b_{\pm}(k_x)$ are spectral weights determined by initial
 147 conditions.

148 In the reference system following the surface current (i.e., $U(0) = 0$), the
 149 dispersion relation always has one positive and one negative solution, corre-
 150 sponding to waves propagating in direction \mathbf{k} and $-\mathbf{k}$, respectively, implying
 151 that $\omega_+ \geq 0$ and $\omega_- \leq 0$.

152 Our initial condition is that the shape of the packet is prescribed at focus,
 153 $t = 0$, and propagates only in the positive x direction. Let the Fourier transform
 154 of ζ at focus be

$$\zeta(x, 0) = \int_{-\infty}^{\infty} \frac{dk_x}{2\pi} \tilde{\zeta}_0(k_x) e^{ik_x x}; \quad \tilde{\zeta}_0(k_x) = \int_{-\infty}^{\infty} dx \zeta(x, 0) e^{-ik_x x}, \quad (4)$$

155 which with the general linear solution (3) implies

$$b_+(k_x) + b_-(k_x) = \tilde{\zeta}_0(k_x). \quad (5)$$

156 In order to obtain the appropriate initial shape with only plane waves prop-
 157 agating in the $+x$ direction, we couple the kernel $\exp(ik_x x)$ to $\exp(-i\omega_- t)$
 158 when $k_x < 0$ and to $\exp(-i\omega_+ t)$ when $k_x > 0$:

$$b_{\pm}(k_x) = \tilde{\zeta}_0(k_x) \Theta(\pm k_x), \quad (6)$$

159 where Θ is the Heaviside unit step function, explicitly

$$\tilde{\zeta}_0(k_x, t) = \tilde{\zeta}_0(k_x) \left[e^{-i\omega_-(k_x)t} \Theta(-k_x) + e^{-i\omega_+(k_x)t} \Theta(k_x) \right]. \quad (7)$$

160 Substituting $k_x \rightarrow -k_x$ for the b_- term and noticing the well-known symmetry

$$\omega_-(-k_x) = -\omega_+(k_x), \quad (8)$$

161 the solution may be written

$$\zeta(x, t) = \int_0^{\infty} \frac{dk}{2\pi} \left[\tilde{\zeta}_0(-k) e^{-i\psi} + \tilde{\zeta}_0(k) e^{i\psi} \right], \quad (9)$$

6 *Wave focusing on a shear current*

162 where we now simplify the notation, $k_x \rightarrow k$ and $\omega_+(k_x) \rightarrow \omega(k)$ is the positive-
163 valued frequency. As shorthand, we define the wave phase

$$\psi = \psi(x, t; k) \equiv kx - \omega(k)t, \quad (10)$$

164 frequently written without arguments for succinctness. Since (9) is real-valued,
165 it follows that $\tilde{\zeta}_0(-k) = \tilde{\zeta}_0^*(k)$, so we finally write

$$\zeta(x, t) = 2 \operatorname{Re} \int_0^\infty \frac{dk}{2\pi} \tilde{\zeta}_0(k) e^{i\psi}. \quad (11)$$

166 In the following we shall use this form and therefore assume $k_x = k > 0$, with
167 the exception of derivations where it is sometimes necessary to return to the
168 more fundamental form.

169 In particular, if the shape at $t = 0$ is symmetrical around $x = 0$, $\tilde{\zeta}_0(k)$ is
170 real, hence

$$\zeta(x, t) = 2 \int_0^\infty \frac{dk}{2\pi} \tilde{\zeta}_0(k) \cos \psi(x, t; k). \quad (12)$$

171 **2.3 Vertically sheared currents**

172 We here introduce the classic linear and exponential shear profiles used
173 as canonical examples, and approximate linear theories for arbitrary shear.
174 Known results are briefly reviewed and framed in the formalism we use herein.

175 **2.3.1 Current with constant shear**

176 First we quote well-known results for the simple, linearly depth-dependent
177 current

$$\mathbf{U}(z) = Sz\mathbf{e}_U = Sz\{\cos \theta, \sin \theta\} \quad (13)$$

178 with S the constant shear.

179 Due to the symmetry (8) it is sufficient to consider the positive-valued $\omega(k)$
180 assuming positive k , which we write in the form

$$\omega_\sigma(k) = kc_\sigma(k) = \sqrt{g\mathcal{X}} - \sigma \quad (14)$$

181 where the shear-modified wave number is

$$\mathcal{X}(k) = k + \sigma^2/g, \quad (15)$$

182 and

$$\sigma \equiv \frac{1}{2}S \cos \theta. \quad (16)$$

183 The group velocity is

$$c_{g\sigma}(k) = \frac{1}{2} \sqrt{\frac{g}{\mathcal{X}}}. \quad (17)$$

184 Note for future reference that $c_{g\sigma}(k)$ is symmetrical under $\sigma \rightarrow -\sigma$ while c_σ
185 is not.

186 In the spirit of [17, 18] we may define a Froude-shear number for the linear-
187 shear current based on velocity S/k and length $1/k$,

$$\text{FS}_{\text{lin.}} = \frac{S}{2\sqrt{gk}} \quad (18)$$

188 so that the shear-modified wave number is $\varkappa = k(1 + \text{FS}_{\text{lin.}}^2 \cos^2 \theta)$. This is
189 particularly instructive in narrow-band cases (e.g., long groups with Gaussian
190 envelope) where there is a dominating carrier wave number; see sections 3.4
191 and 4.1 for further details. Here and henceforth a subscript ‘lin.’ indicates the
192 subscribed quantity pertains to the linear current.

193 2.3.2 Current with exponential shear

194 We will frequently make use of the model current with exponential depth
195 profile, which we define

$$\mathbf{U}_{\text{exp}}(z) = U_0(e^{\alpha z} - 1)\mathbf{e}_U = \{U_{x0}, U_{y0}\}(e^{\alpha z} - 1), \quad (19)$$

196 where $\alpha > 0$ is a shear strength and U_{x0} a current strength. This model has
197 been considered for the purposes of wave-current interactions for a very long
198 time, thanks to its similarity to a wind-driven shear-layer (Ekman current)
199 [19].

200 An explicit, exact solution to the linear problem with the exponential cur-
201 rent can be found in terms of hypergeometric functions, which we review in
202 section 4.4. The dispersion relation in this case is, however, implicit but easily
203 calculated numerically.

204 The exponential profile is a particularly useful model in combination with
205 the weak-shear approximation (see section 2.4.1), an approximation which is
206 excellent in the vast majority of oceanographic and coastal flows. Near-surface
207 flows, such as wind-driven Ekman layers or estuarine plumes, are typically
208 reasonably approximated by an exponential, and in this case the linearised
209 weak-shear theory yields a wealth of explicit analytical results, a number of
210 which we derive in this article.

211 2.4 Weak-shear and weak-curvature theory

212 We will summarise the results of theories for dispersion relations and flow fields
213 for an arbitrary current $\mathbf{U}(z)$ satisfying criteria of weak shear and weak cur-
214 vature, respectively. We emphasize that although the former approximation is
215 termed ‘weak shear’ due to the formal requirements for it to be asymptotically
216 accurate, in fact in an oceanic setting the shear can be very strong as in the
217 case of the Columbia River Estuary considered in section 4.5.1, and still give
218 results accurate to within a few percent or less.

219 The weak-shear approximation is in practice that underlying the celebrated
220 approximation of Stewart & Joy [14], typically sufficient in practice while in

8 *Wave focusing on a shear current*

221 cases of extremely strong shear (as effectively felt by a wave of the wave-
 222 length in question), the strong-shear-weak-curvature expressions [20] could be
 223 necessary.

224 As discussed in Ref. [20], a suitable measure of the effective strength of
 225 the current shear is a dimensionless depth-integrated shear, or “directional
 226 shear-Froude number”, $\delta(\mathbf{k})$, defined as

$$\delta(\mathbf{k}) \equiv \frac{1}{c_0(k)} \int_{-\infty}^0 dz U'_x(z) e^{2kz} \equiv \text{FS}_{\text{gen.}} \cos \theta. \quad (20)$$

227 with $c_0(k) = \sqrt{g/k}$ as usual. We use the symbol δ as well as FS to make contact
 228 with previously published theory [17, 18, 20], despite the slight redundancy.
 229 The x component of \mathbf{U} is taken, being the component aligned with the waves,
 230 $\mathbf{k} \cdot \mathbf{U} = kU_x$.

231 That the parameter $\delta(\mathbf{k})$ is a direct generalisation of the shear-Froude num-
 232 ber (18) for linear shear based on the along-wave (here: x) current component,
 233 is easily seen by inserting $U_x(z) = Sz \cos \theta = 2\sigma z$ which gives $\delta(\mathbf{k}) = \delta_{\text{lin.}}(\mathbf{k})$
 234 with

$$\delta_{\text{lin.}}(\mathbf{k}) = 2\sigma \sqrt{\frac{k}{g}} \int_{-\infty}^0 dz e^{2kz} = \frac{\sigma}{\sqrt{gk}} = \text{FS}_{\text{lin.}} \cos \theta. \quad (21)$$

235 For ease of comparison to the linear-shear case above, it is also instructive
 236 for us to define the shear-induced Doppler shift for a wave propagating at an
 237 angle θ :

$$\sigma_\delta(k) = \omega_0(k) \delta(\mathbf{k}) = k \int_{-\infty}^0 dz U'_x(z) e^{2kz} \quad (22)$$

238 a generalisation of σ for the linear current in Eq. (16). We defined $\omega_0 = \sqrt{gk}$.

239 2.4.1 Weak shear

240 A sufficient criterion for the approximate theory of Stewart & Joy [14] and its
 241 generalisations [21, 22] to be accurate is $\delta(\mathbf{k}) \ll 1$ for all k which contribute
 242 significantly (we follow the convention of [23] that \ll and \gg refer to the
 243 absolute values of the quantities compared). The results in references [14, 22]
 244 were derived assuming weak current, $U \ll c$, yet it is shown in ref. [20] that
 245 the true condition of validity is that the shear is weak. (This was suspected by
 246 Kirby & Chen [22] and in fact obliquely discussed already by Skop [21]). After
 247 a partial integration of the original form of the much-used approximation due
 248 to Stewart & Joy [14], it can be written

$$\omega(k) \approx \sqrt{gk} - \sigma_\delta(k) = \omega_0(k)[1 - \delta(\mathbf{k})]. \quad (23)$$

249 We mention in passing that although (20) performs excellently for most typical
 250 ocean and coastal currents concentrated in the near-surface region (e.g. [20,

251 24]), such as the exponential current profile, it does not perform particularly
 252 well for the linear shear case even when shear is moderate [24]; for currents
 253 which are close to linear, the strong-shear approximation in the next section
 254 should be used.

255 Further formulae in the weak-shear approximation will be quoted or derived
 256 later, as they are needed. Explicit expressions for the exponential current in
 257 the context of surface motion are found in section 3.2.1, and weak-shear theory
 258 for the kinematics and orbital velocities may be found in Section 4.2.

259 2.4.2 Strong shear, weak curvature

260 A similar theory allowing $U(z)$ to have arbitrarily strong shear, but weak
 261 curvature, was developed by Ellingsen & Li [20]; the explicit limitation on
 262 curvature may be found therein. Now $\delta(\mathbf{k})$ can be arbitrarily large compared
 263 to unity. The approximate dispersion relation derived in [20] (equation 18) is

$$\omega(k) \approx \omega_0(k)(\sqrt{1 + \delta^2} - \delta) = \sqrt{gk + \sigma_\delta^2} - \sigma_\delta. \quad (24)$$

264 Ellingsen & Li finds no practical situations where (24) performs significantly
 265 worse than (23), and it fares far better when δ is not small compared to unity.
 266 Notice that when the linear current (13) is inserted, one finds $\sigma_\delta(k) = \sigma$
 267 as defined in (16) and the dispersion relation (14) is regained exactly. The
 268 formalism thus bears a close similarity to that with constant shear, in section
 269 2.3.1. Moreover, $\delta \ll 1$ returns the weak-shear dispersion relation (23) to
 270 leading order.

271 The close resemblance in form to the constant shear case makes it natural
 272 to define a generalised function analogous to Eq. (15),

$$\varkappa_\delta(k) = k + \sigma_\delta(k)^2/g. \quad (25)$$

273 whereby (24) can be written $\omega(k) \approx \omega_\delta(k) = \sqrt{g\varkappa_\delta(k)} - \sigma_\delta(k)$.

274 3 Surface motion

275 In this section we derive and analyse a number of potentially useful results for
 276 the moving free surface of a focusing wave groups, including explicit approx-
 277 imate expressions for general and special cases. We assume throughout in
 278 Section 3 that the surface elevation at focus, $\zeta(x, 0)$, is symmetric in x for
 279 simplicity.

280 For purposes of analytical treatment, there are two challenges to contend
 281 with when a vertical shear current is present: the dispersion relation is not
 282 in general given in closed form, and the waves are described by Fourier inte-
 283 grals with no closed-form solutions. We consider in the following a number of
 284 special cases and/or simplifying assumptions which allow useful, closed-form
 285 expressions to be derived.

3.1 General dispersion considerations

We briefly argue why the dispersion relation predicts that vertical shear of $U(z)$ has little effect on the group envelope, but can greatly affect the phase velocity and hence the wave kinematics. We focus now on the simplest case of a linear shear current (13) which is sufficient to illustrate the overall effect of shear.

If now σ is not small compared to \sqrt{k} , the phase velocity in equation (14) depends strongly on θ ; for $\cos\theta > 0$ (opposing shear) the two terms in (14) tend to cancel each other while for $\cos\theta < 0$ (following shear) they add to each other, giving a phase velocity which can be far higher. In contrast, the group velocity is identical under $\theta \rightarrow -\theta$ since $c_{g\sigma}$ depends on $|\cos\theta|$ only.

Bearing in mind that the envelope of a focusing group of waves is governed by the group velocity and its k derivative, the evolution of the group as a whole is largely independent of whether propagation is upstream or downstream. The kinematics of the wave patterns within the focusing group, however, are related to the phase velocity which can be very different depending on the direction θ . To wit, the ratio between phase velocity for opposite directions $\theta = 0$ and $\theta = \pi$ is

$$\frac{c(\theta = \pi)}{c(\theta = 0)} = \frac{\sqrt{1 + \text{FS}_{\text{lin.}}^2} + \text{FS}_{\text{lin.}}}{\sqrt{1 + \text{FS}_{\text{lin.}}^2} - \text{FS}_{\text{lin.}}} = \left(\sqrt{1 + \text{FS}_{\text{lin.}}^2} + \text{FS}_{\text{lin.}} \right)^2 \quad (26)$$

which very significant indeed when $\text{FS}_{\text{lin.}} \sim \mathcal{O}(1)$. In section 4 we study the closely related amplification of horizontal velocities at focus depending on θ .

The situation becomes particularly pointed for strong shear, $\sigma \gg 1$, in which case the phase and group velocities in equations (14) and (17) are

$$c_{\sigma}(k) = \frac{1}{k}(|\sigma| - \sigma) + \frac{g}{2|\sigma|} + \dots \quad (27a)$$

$$c_{g\sigma}(k) = \frac{g}{2|\sigma|} + \dots \quad (27b)$$

For $\cos\theta > 0$ the group and phase velocities become asymptotically equal and the wave becomes nondispersive, whereas for $\cos\theta < 0$ phase velocity can be many times greater than group velocity.

The effect is illustrated in Fig. 2 where we plot $\eta(x, t)$ at a series of equidistant times as the wave group focuses and defocuses. A short Gaussian packet with carrier wave number k_0 and length L is chosen for improved illustration, as defined and discussed in section 3.4. We plot time in units of $T_{\text{ref}} = \sqrt{L/g}$. The surface elevation $\zeta(x, t)$ was evaluated numerically from Eq. (12). The shear S is constant and made strong for clarity of illustration, $\text{FS}_{\text{lin.}} \cos\theta$ takes the values $-\frac{1}{2}, 0$ and $\frac{1}{2}$ at $k = k_0$. When $\theta = 0$ focusing is characterised by a wave group which slowly varying phase as the group passes through focus. When $\theta = \pi$ on the other hand, crests and troughs move so rapidly that they

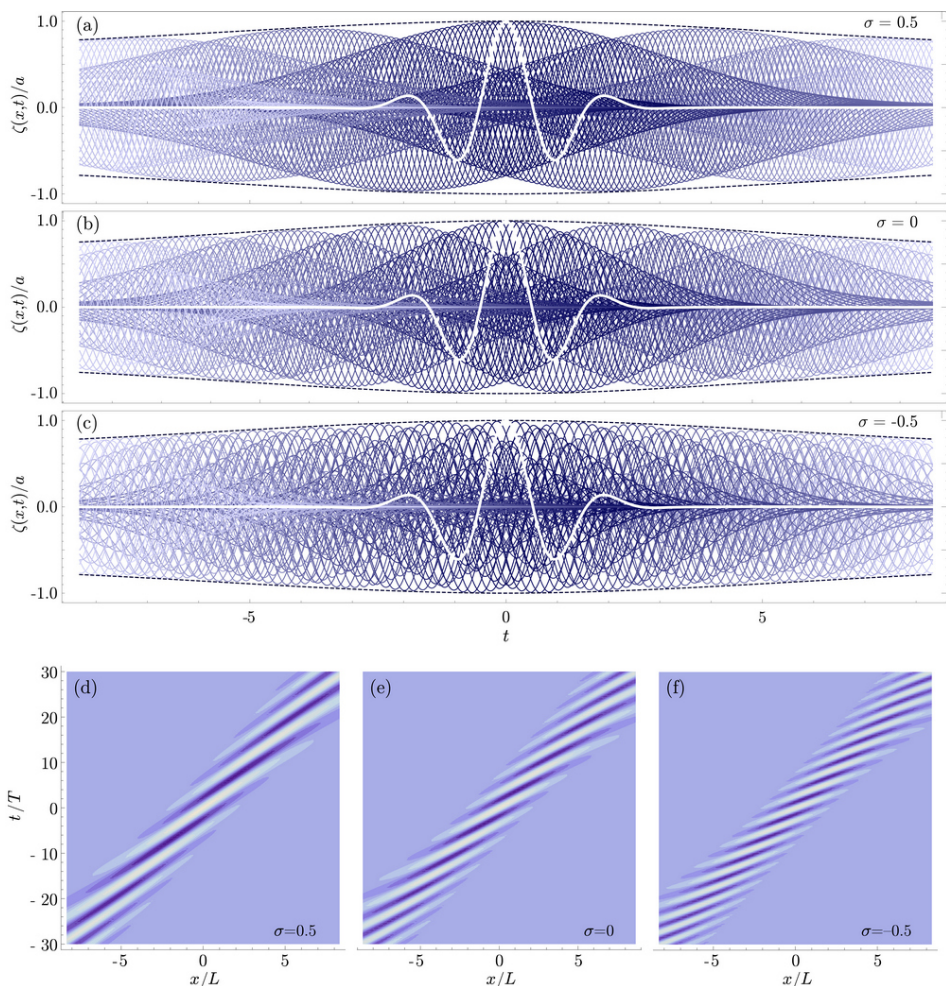


Fig. 2 Illustration of the different kinematic behaviour for waves focusing into a short group, $k_0L = 3$ with a Gaussian envelope of standard deviation L in deep water for opposing, zero and following linear shear. (a,b,c): $\zeta(x,t)/a$ for t from -30 to 30 in steps of 0.25 with graphs growing progressively lighter in colour for increasing $|t|$, and the $t = 0$ (focused) wave group drawn as thicker white lines. The dashed lines are plots of the maximum group height, $\pm L(L^4 + B_0^2 t_g(x)^2)^{-1/4}$, using Eqs. (56), (54) and $t_g(x) = x/c_g(k_0)$. (d,e,f): same, with ζ as shades from darkest to lightest ($\zeta/a = -1$ and $\zeta/a = 1$, respectively), varying in space and time.

320 appear almost chaotic at this time resolution. (An illustration of the shallow
321 water case is given in A.3.)

322 Another case suitable for illustration is the wave which takes the form of
323 a Gaussian soliton at focus,

$$\zeta(x, 0) = ae^{-x^2/2L^2}; \quad \tilde{\zeta}_0(k) = \sqrt{2\pi}aLe^{-\frac{1}{2}k^2L^2}. \quad (28)$$

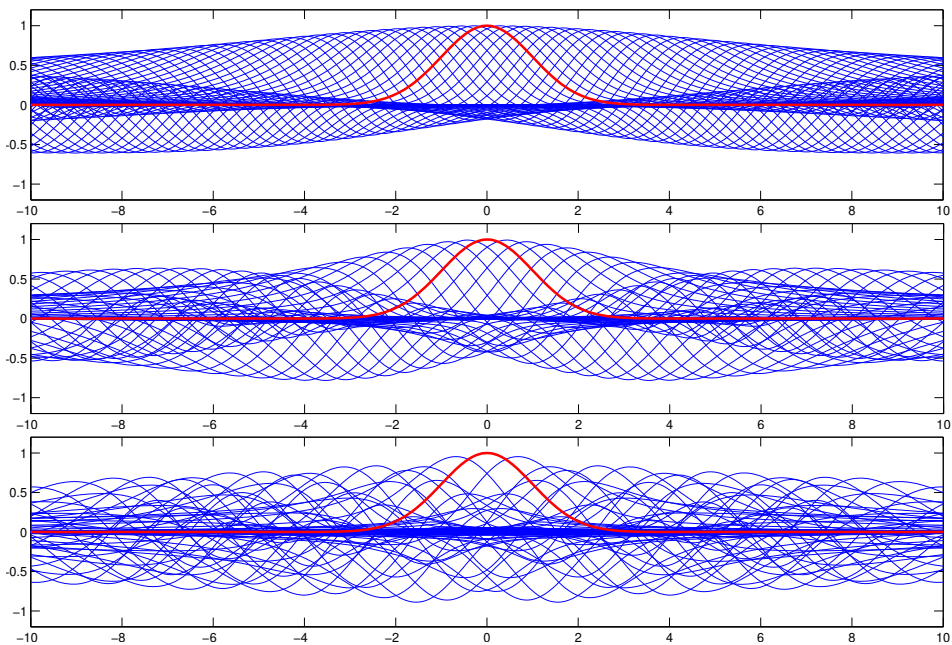


Fig. 3 Illustration of the different kinematic behaviour for waves focusing into a Gaussian soliton of nondimensional width 1 in deep water. The solid graphs show $\zeta(x, t)/a$ for t/T_{ref} from -20 to 20 in steps of 0.5 . Here $T_{\text{ref}}\sigma = 1, 0$ and -1 (top to bottom). The abscissa is x/L , and $\zeta(x, 0)/a$ is shown with thicker, red line.

324 the width of the Gaussian focused shape. The shape is considered by [25],
 325 where an explicit solution is found in the shallow-water case without shear.
 326 The surface elevation according to Eq. (12) is

$$\zeta(x, t) = \sqrt{\frac{2}{\pi}} aL \operatorname{Re} \left[\int_0^{\infty} dk e^{-\frac{1}{2}k^2 L^2 + ikx - i\omega(k)t} \right]. \quad (29)$$

327 The time evolution of a group focusing into a Gaussian soliton with constant
 328 shear in deep water is shown in Fig. 3. The behaviour is once again that the
 329 wave group focusing on following shear ($\cos\theta = -1$) and that on opposing
 330 shear ($\cos\theta = 1$), while sharing the same averaged envelope, behave quite dif-
 331 ferently in a kinematic sense, the former appearing as a single soliton rising
 332 slowly to its maximum and declines again, whereas the latter draws a hec-
 333 tic picture of crests and troughs rapidly replacing each other as the focus is
 334 approached.

325 3.2 Stationary phase approximations

336 Before considering particular cases we derive a general expression for the sta-
 337 tionary phase approximation of the shape of the wave packet sufficiently far
 338 from focus. Assume therefore that $x, t \gg 1$. Formally we write $\psi = t(k\xi - \omega(k))$

339 where

$$\xi \equiv x/t, \quad (30)$$

340 and we assume ξ is moderately large, in the order of $c_g(k)$, then take the
341 asymptotic solution as $|t| \rightarrow \infty$ [23].

342 Equation (12) is rapidly oscillating and dominated by its stationary points
343 when $|t| \rightarrow \infty$. We presume for simplicity that only one such exists, which is the
344 case for for gravity waves except very special and extreme cases; should several
345 stationary points exist, the procedure is simply repeated for each one. Equation
346 (12) has its stationary point at $k = k_{\text{sp}}$ which solves $\psi'(k_{\text{sp}}) = 0$ where a prime
347 here denotes differentiation w.r.t. k . This implies $c_g(k_{\text{sp}}) = \xi$ with $c_g(k_{\text{sp}})$ being
348 the stationary-point group velocity. In general the stationary point must be
349 found numerically, for example with the Direct Integration Method [26] which
350 we will employ later.

351 Now let a subscript ‘sp’ indicate the quantity is evaluated at $k = k_{\text{sp}}$. To
352 connect with formalism in following sections (equation (54) in particular), we
353 define

$$A_{\text{sp}} = \left. \frac{d\omega}{dk} \right|_{k=k_{\text{sp}}} ; \quad B_{\text{sp}}(\xi) = \left. \frac{d^2\omega}{dk^2} \right|_{k=k_{\text{sp}}} . \quad (31)$$

354 Clearly, $A_{\text{sp}} = \omega'_{\text{sp}} = c_g(k_{\text{sp}}) = \xi$, and $\psi''_{\text{sp}} = -\omega''_{\text{sp}}t = -B_{\text{sp}}(\xi)t$ (note that B_{sp}
355 is a function of ξ because k_{sp} is). With the stationary phase approximation
356 (e.g., §6.5 of [23])

$$\begin{aligned} \zeta(x, t) &= \text{Re} \left\{ \frac{1}{\pi} \int_0^\infty dk \tilde{\zeta}_0(k) e^{i\psi(x, t; k)} \right\} \\ &\approx \sqrt{\frac{2}{\pi |B_{\text{sp}}(\xi)t|}} \text{Re} \left\{ \tilde{\zeta}_0(k_{\text{sp}}) \exp \left[i(\psi_{\text{sp}} + \frac{\pi}{4} \text{Sg}(x)) \right] \right\} \Theta(\xi \geq c_{g, \text{min}}), \quad (32) \end{aligned}$$

357 where ‘Sg’ denotes the sign function, Θ is the unit step function, and $c_{g, \text{min}}$ is
358 the smallest value $c_g(k)$ can take. In particular, solutions only exist for $\xi > 0$
359 (bear in mind the assumption $\xi/c_g \sim 1$).

360 In all cases in the following, $\text{Sg}[\psi''_{\text{sp}}] = \text{Sg}(x) = \text{Sg}(t)$ when a stationary
361 point exists, which we therefore assume henceforth.

362 3.2.1 Stationary phase approximation, exponential shear

363 Consider next the case of an exponential current, equation (19). The weak-
364 shear approximation is sure to be accurate in any direction θ if $\delta(\mathbf{k}) \ll 1$
365 where, from equation (20), $\delta(\mathbf{k}) = \delta_\alpha(\mathbf{k})$ with w

$$\delta_\alpha(\mathbf{k}) = \frac{U_{x0}}{c_0(k)} \frac{\alpha}{\alpha + 2k}. \quad (33)$$

366 We might equally refer to δ_α as the Froude-shear number for the exponential
367 case (notation $\text{FS}_{\text{exp}} \cos \theta = \delta_\alpha$, although we will use δ_α in the following).

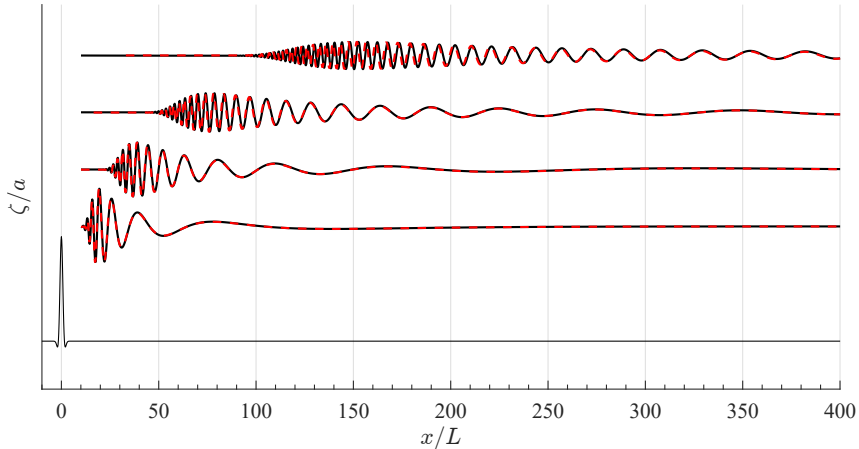


Fig. 4 Wave surface elevation on an exponential shear current (19) with $U_0/\sqrt{gL} = 0.2$, $\alpha L = 2.5$ and $\theta = 0$. The red dashed line is the stationary phase approximation (32) with the weak exponential shear approximation using equations (35b), (36) and (37). The black solid line is the numerical solution using the Direct Integration Method [26]. The initial wave surface is a Gaussian group $\zeta(x, 0) = a \exp(-\frac{1}{2}x^2/L^2) \cos(k_0x)$ with $k_0L = 1$. The focusing occurs at $t = 0$.

368 For a particular propagation direction θ it is sufficient that $\delta(\mathbf{k}) \ll 1$ for all
 369 significant values of k . The maximum absolute value of δ_α is at $k = \alpha/2$ where

$$\delta_{\alpha, \max} = |U_{x0}| \sqrt{\alpha/8g}. \quad (34)$$

370 Note that the global maximum of δ_α does not depend on the lengthscale L ,
 371 i.e., $\delta_{\max} \ll 1$ guarantees the accuracy of weak-shear theory independently of
 372 the size and shape of the wave group at focus, as should be expected. However,
 373 note that this is a sufficient, not a necessary condition: if αL is much greater
 374 or smaller than unity, δ_α could remain far smaller than its maximal value for
 375 all k which contribute significantly.

376 We note in passing the correspondence with the assumption in Stewart
 377 & Joy's theory of weak current compared to the phase velocity; at $k = \alpha/2$
 378 the condition $\delta_{\max} \ll 1$ can be written $U_{x0}/2c \ll 1$ since the phase velocity
 379 is approximately $\sqrt{2g/\alpha}$. This is a (reference system invariant) weak current
 380 assumption: the maximum difference in $U_{x0}(z)$ over the water column is much
 381 smaller than twice the phase velocity.

382 The weak-shear approximation, eq. (23), yields

$$\omega(k) \approx \sqrt{gk} - \frac{U_{x0}\alpha k}{2k + \alpha}; \quad (35a)$$

$$A_{\text{sp}} = \xi = \frac{1}{2} \sqrt{\frac{g}{k_{\text{sp}}}} - \frac{U_{x0}\alpha^2}{(2k_{\text{sp}} + \alpha)^2}; \quad (35b)$$

$$B_{\text{sp}} = -\frac{1}{4k_{\text{sp}}} \sqrt{\frac{g}{k_{\text{sp}}}} + \frac{4U_{x0}\alpha^2}{(2k_{\text{sp}} + \alpha)^3} = -\frac{\xi}{2k_{\text{sp}}} - \frac{U_{x0}\alpha^2(\alpha - 6k_{\text{sp}})}{2k_{\text{sp}}(2k_{\text{sp}} + \alpha)^3}. \quad (35c)$$

383 We wish to solve (35b) with respect to k_{sp} . The assumption behind the weak-
 384 shear approximation is that $\delta \ll 1$ as defined in Eq. (20). In this spirit we
 385 write $\alpha U_{0k} \rightarrow \gamma \alpha U_{0k}$ with γ a ‘‘smallness’’ parameter for bookkeeping we will
 386 eventually take to 1. We expand $k_{\text{sp}} = k_{\text{sp}}^{(0)} + \gamma k_{\text{sp}}^{(1)}$ and solve (35b) in orders
 387 of γ and insert into (35c) to obtain

$$k_{\text{sp}} = \frac{g}{4\xi^2} - \frac{2gU_{x0}\alpha^2\xi}{(g + 2\alpha\xi^2)^2} + \mathcal{O}(\gamma^2); \quad (36)$$

$$B_{\text{sp}}(\xi) = -\frac{2\xi^3}{g} - \frac{8U_{x0}\alpha^2\xi^6(g - 6\alpha\xi^2)}{g(g + 2\alpha\xi^2)^3} + \mathcal{O}(\gamma^2). \quad (37)$$

388 The frequency in the weak-shear stationary phase approximation is found by
 389 inserting (36) into (35a) and retaining terms to $\mathcal{O}(\gamma)$,

$$\omega_{\text{sp}} = \frac{g}{2\xi} - \frac{U_{x0}g\alpha(g + 6\alpha\xi^2)}{2(g + 2\alpha\xi^2)^2} + \mathcal{O}(\gamma^2), \quad (38)$$

390 while the applicability of weak-shear theory is well indicated by the Froude-
 391 shear number at the stationary point,

$$\delta_{\alpha,\text{sp}} = \frac{\alpha\xi U_{x0}}{g + 2\xi^2\alpha} + \mathcal{O}(\gamma^2) \quad (39)$$

392 which has its maximum at $\xi = \sqrt{g/2\alpha}$ where the result (34) is regained.

393 We test the stationary phase surface elevation solution in figure 4. The
 394 red line indicates the arbitrary-accuracy numerical solution using the method
 395 of reference [26], whereas the black is the weak-shear stationary phase solu-
 396 tion, found by inserting (38) and (37) into equation (32). We observe a very
 397 slight phase shift over time because the frequency ω_{sp} is only approximate,
 398 whereas the ‘exact’ and approximate envelope of the group are virtually
 399 indistinguishable.

400 3.2.2 Stationary phase approximation for linear shear

401 In the special case of linear shear, an explicit formula is readily derived. Rather
 402 than use Eq. (32) we substitute $\varpi = \sqrt{gk + \sigma^2}$ into the dispersion relation
 403 (14), $\omega = \omega_\sigma = \varpi - \sigma$, from which it follows that $k(\varpi) = (\varpi^2 - \sigma^2)/g$; $dk =$
 404 $(2\varpi/g)d\varpi$, and according to equation (12) $\zeta(x, t)$ is,

$$\begin{aligned} \zeta(x, t) &= 2 \operatorname{Re} \int_0^\infty \frac{dk}{2\pi} \tilde{\zeta}_0(k) e^{ikx - i\omega_\sigma t} \\ &= \frac{2}{\pi g} \operatorname{Re} \left[e^{-ix\sigma^2/g + i\sigma t} \int_{|\sigma|}^\infty d\varpi \varpi \tilde{\zeta}_0(k(\varpi)) e^{ix\varpi^2/g - i\varpi t} \right]. \end{aligned} \quad (40)$$

16 *Wave focusing on a shear current*

405 Formally we write the exponent as $it\phi(\varpi)$ with $\phi(\varpi) = \varpi^2 x/gt - \varpi$, and
 406 consider the asymptote $t \rightarrow \infty$ while assuming $x/t \sim \mathcal{O}(1)$. The stationary
 407 phase $\varpi = \varpi_{\text{sp}}$ is

$$\phi'(\varpi_{\text{sp}}) = \left(\frac{2x}{gt} \varpi_{\text{sp}} - 1 \right) \Big|_{\varpi=\varpi_{\text{sp}}} = 0, \quad (41)$$

408 or, in other words, $\varpi_{\text{sp}} = gt/2x$. (Introduction of the symbol $\xi = x/t$ is not
 409 equally handy as in the previous section, and we retain x and t here.) With
 410 the stationary phase approximation the integral is (e.g., §6.5 of [23])

$$\int_{|\sigma|}^{\infty} d\varpi \varpi \tilde{\zeta}_0(k(\varpi)) e^{ix\varpi^2/g - i\varpi t} \approx \sqrt{\frac{\pi g}{|x|}} \frac{t \tilde{\zeta}_0(k_{\text{sp}})}{2x} \exp i \left[-\frac{gt^2}{4x} + \frac{\pi}{4} \text{Sg}(x) \right] \Theta(k_{\text{sp}}) \quad (42)$$

411 with

$$k_{\text{sp}} = \frac{\varpi_{\text{sp}}^2 - \sigma^2}{g} = \frac{gt^2}{4x^2} - \frac{\sigma^2}{g}. \quad (43)$$

412 There is no stationary point unless $t/2x > |\sigma|$, hence the unit step function Θ .
 413 Thus, taking the real part, the stationary phase approximation to $\zeta(x, t)$ is

$$\zeta(x, t) \approx \sqrt{\frac{g}{\pi|x|}} \frac{t}{x} \text{Re} \left\{ \tilde{\zeta}_0(k_{\text{sp}}) \exp i \left[-\frac{\sigma^2 x}{g} - \frac{gt^2}{4x} + \sigma t + \frac{\pi}{4} \text{Sg}(x) \right] \right\} \Theta(k_{\text{sp}}). \quad (44)$$

414 The approximation is only nonzero when x and t are either both negative or
 415 both positive, as is reasonable since we have assumed propagation towards
 416 positive x . In the symmetrical case where $\zeta(x, 0) = \zeta(-x, 0)$, $\tilde{\zeta}_0(k)$ is real and
 417 the exponential becomes a cosine.

418 3.3 Waves focusing to δ -function singularity

419 Assuming the wave form at focus is a Dirac δ function is the most extreme
 420 form of focusing. As is conventional, we overlook the obvious fact that linear
 421 theory cannot describe such a wave packet close to its maximum, and regard
 422 the solution some time before and after focusing. The case is particular in the
 423 sense that the wave shape at focus has no intrinsic length scale. We write the
 424 elevation at focus with the delta function in the limit form [e.g., 27, §7.2]

$$\zeta(x, 0) = a\delta(x/L) = \lim_{\mu \rightarrow 0^+} \frac{a}{\pi} \frac{\mu}{x^2/L^2 + \mu^2} \quad (45)$$

425 where L is some arbitrary, finite lengthscale for dimensional reasons (in later
 426 sections it will play the role of characteristic width of the wave packet at focus).
 427 Its obtains physical meaning is only when this singular model flow is compared
 428 to whatever real flow it models. The Fourier transform is

$$\tilde{\zeta}_0(k) = aL \lim_{\mu \rightarrow 0^+} e^{-\mu L|k|}. \quad (46)$$

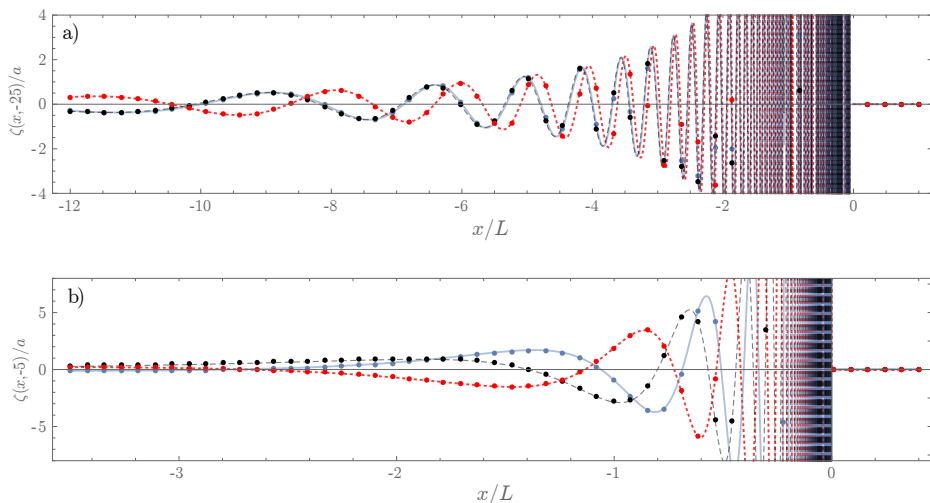


Fig. 5 Surface elevation ζ/a (x in units of L , t in units of $T_{\text{ref}} = \sqrt{L/g}$) for a wave group focusing to a δ -function singularity on a linear shear current. a) $t = -25 T_{\text{ref}}$, b) $t = -5 T_{\text{ref}}$. Three different shear strengths: $T_{\text{ref}}\sigma = -0.5$ (blue, solid), $T_{\text{ref}}\sigma = 0.5$ (black, dashed), and $T_{\text{ref}}\sigma = 0$ (red, dotted); circular markers show the stationary phase approximation (49).

429 Using (12) we have

$$\zeta(x, t) = 2aL \lim_{\mu \rightarrow 0^+} \int_0^\infty \frac{dk}{2\pi} \cos[kx - \omega(k)t] e^{-\mu Lk}. \quad (47)$$

430 The role of μ is to render the integral well defined.

431 For an integral with rapidly oscillating integrand of form

$$\int dq f(q) e^{iX\phi(q)} \quad (48)$$

432 with $\phi(q) \sim \mathcal{O}(1)$, the stationary phase approximation is accurate for $X \gg 1$
 433 assuming $f(q)$ is significant for $q \sim \mathcal{O}(1)$. Substituting $q = \mu k$ into (47),
 434 we observe that $X = x/\mu$, which is very large for any nonzero x . Thus the
 435 stationary phase approximation should be sufficiently accurate everywhere, for
 436 practical purposes.

437 From equation (44) the stationary phase approximation for linear shear is

$$\zeta(x, t) = aL \sqrt{\frac{g}{\pi|x|}} \frac{t}{x} \cos \left[\frac{\sigma^2 x}{g} + \frac{gt^2}{4x} - \sigma t - \frac{\pi}{4} \text{Sg}(x) \right] \Theta \left(\frac{gt^2}{2x} - |\sigma|t \right). \quad (49)$$

438 Corresponding expressions for $\zeta(x, t)$ on other shear currents, including the
 439 special case of an exponential currents, are obtained by inserting $\tilde{\zeta}_{\text{sp}} = aL$ into
 440 the results in sections 3.2.

441 The surface elevation for a linear wave focusing towards a δ -function sin-
 442 gularity is shown in Fig. 5. Lines show a direct calculation of integral (47)

443 with the integration path rotated slightly into the complex k plane (closed
 444 with a non-contributing arc at infinity), ensuring exponential convergence. Let
 445 $\tilde{\sigma} = \sigma T_{\text{ref}}$ and $\tilde{t} = t/T_{\text{ref}}$ with reference time $T_{\text{ref}} = \sqrt{L/g}$. Three differ-
 446 ent shear strengths are shown: $\tilde{\sigma} = -0.5, 0$ and 0.5 with reference time The
 447 circular markers are the values obtained using equation (49); these are indis-
 448 tinguishable from the exact integral in all cases. As discussed in connection
 449 with equation (44), the cases $\tilde{\sigma} = -0.5$ and 0.5 are nearly indistinguishable at
 450 $\tilde{t} = -25$, but differences manifest at the later time $\tilde{t} = -5$.

451 In stark contrast, the behaviour of the wave phase for case $\tilde{\sigma} = 0$ is always
 452 quite distinct from the others, as should be obvious from inspection of the
 453 argument of the cosine in Eq. (49), where the term $\sigma^2 x/g$ is highly significant
 454 when $t/x \sim \sigma/g$. This observation has consequences for creating a focusing
 455 wave in a laboratory with a shear current.

456 An approximate solution in the shallow-water limit, which generalises
 457 results in Refs. [25, 28], is found in appendix A.2.

458 3.4 Long wave group with Gaussian envelope

459 We next consider a group with Gaussian envelope of characteristic length L
 460 and carrier wave number $k_0 > 0$, i.e.,

$$\zeta(x, 0) = ae^{-x^2/2L^2} \cos(k_0 x). \quad (50)$$

461 We allow the shear current $U(z)$ in equation (1) to be arbitrary and assume
 462 $\omega(k)$ and its first and second derivatives are known. Note that $k_0 L$ now acts as
 463 a bandwidth parameter: The higher $k_0 L$, the narrower the bandwidth: $k_0 L$ is
 464 approximately the number of wavelengths of the carrier wave within the group.
 465 We will assume in derivations that the group is long (i.e., narrowband), $k_0 L \gg$
 466 1, yet we will see in the following that narrowband (long-group) approximations
 467 are excellent for many practical purposes already at $k_0 L = 3 - 5$ which would
 468 not in most cases be considered a ‘long’ group.

469 Taking the Fourier transform of the Gaussian group we obtain with
 470 equation (11)

$$\zeta(x, t) = \frac{aL}{\sqrt{2\pi}} \int_0^\infty dk \left[e^{-\frac{1}{2}(k-k_0)^2 L^2} + e^{-\frac{1}{2}(k+k_0)^2 L^2} \right] \cos[kx - \omega(k)t]. \quad (51)$$

471 When $k_0 L \gg 1$, only the first term in the brackets makes a significant con-
 472 tribution, so, ignoring a term of order $\exp(-\frac{1}{2}k_0^2 L^2)$, we may simplify (51)
 473 to

$$\zeta(x, t) \approx \frac{aL}{\sqrt{2\pi}} \int_0^\infty dk e^{-\frac{1}{2}(k-k_0)^2 L^2} \cos[kx - \omega(k)t]. \quad (52)$$

474 This simplification becomes suspect for $k_0 L \lesssim 3$, depending on the required
 475 level of accuracy.

476 This is the Gaussian group in the sense of [15], prescribing the spatial shape
 477 of the wave at focus, slightly different from the definition used in, e.g., [29, 30]
 478 where the time series of the wave elevation is specified in the time domain.

479 The integral (52) gets its significant contributions from near $k = k_0$. The
 480 longer the group, i.e., the more periods of the carrier wave it contains, the more
 481 focused the integral is around this value. We thus assume the group width L
 482 is much larger than a wavelength, i.e., $k_0L \gg 1$. Following [15] we expand the
 483 dispersion relation in a Taylor series around $k = k_0$,

$$\omega(k) = \omega(k_0) + A_0(k - k_0) + \frac{1}{2}B_0(k - k_0)^2 + \dots \quad (53)$$

484 where

$$A_0 = \left. \frac{d\omega}{dk} \right|_{k=k_0}; \quad B_0 = \left. \frac{d^2\omega}{dk^2} \right|_{k=k_0} \quad (54)$$

485 are found from the dispersion relation, either analytically or numerically using,
 486 e.g., the Direct Integration Method [26].

487 Since k_0L is large the resulting integral is of Laplace type and is approx-
 488 imated as such (see, e.g., § 6.4 of [23]) whereby ζ tends asymptotically to
 489

$$\frac{\zeta(x, t)}{a} \approx \frac{L}{\sqrt{2\pi}} \operatorname{Re} \left\{ e^{ik_0x - i\omega(k_0)t} \int_{-\infty}^{\infty} dq e^{-\frac{1}{2}(L^2 + iB_0t)q^2 + iq(x - A_0t)} \right\} \quad (55a)$$

$$= \operatorname{Re} \left\{ \frac{L}{\sqrt{L^2 + iB_0t}} \exp \left[ik_0x - i\omega(k_0)t - \frac{(x - A_0t)^2}{2(L^2 + iB_0t)} \right] \right\} \quad (55b)$$

490 with $q = k - k_0$. Taking the real part readily yields

$$\begin{aligned} \frac{\zeta(x, t)}{a} &\approx \left(\frac{L^4}{L^4 + B_0^2 t^2} \right)^{\frac{1}{4}} \exp \left[-\frac{L^2(x - A_0t)^2}{2(L^4 + B_0^2 t^2)} \right] \\ &\times \cos \left[k_0x - \omega(k_0)t - \frac{1}{2} \arctan \left(\frac{B_0t}{L^2} \right) + \frac{(x - A_0t)^2 B_0t}{2(L^4 + B_0^2 t^2)} \right]. \end{aligned} \quad (56)$$

491 This is the very general result of Ref. [15]. The effect of currents (and other
 492 factors affecting the dispersion, such as finite depth) is only to modify the
 493 expressions for A_0 and B_0 through the more general dispersion relation. For
 494 gravity waves, A_0 is typically positive and B_0 negative. In the cases we con-
 495 sider, the approximation (56) is reasonable already at $k_0L \sim 3$, adequate for
 496 many purposes.

497 3.4.1 Linear shear

498 Turning to our special case of constant shear and deep water, A_0 and B_0 are
 499 easily found from Eq. (14) and may be instructively written in terms of a
 500 shear-modified wave number (see eq. (15))

$$\varkappa_0 = k_0 + \sigma^2/g \quad (57)$$

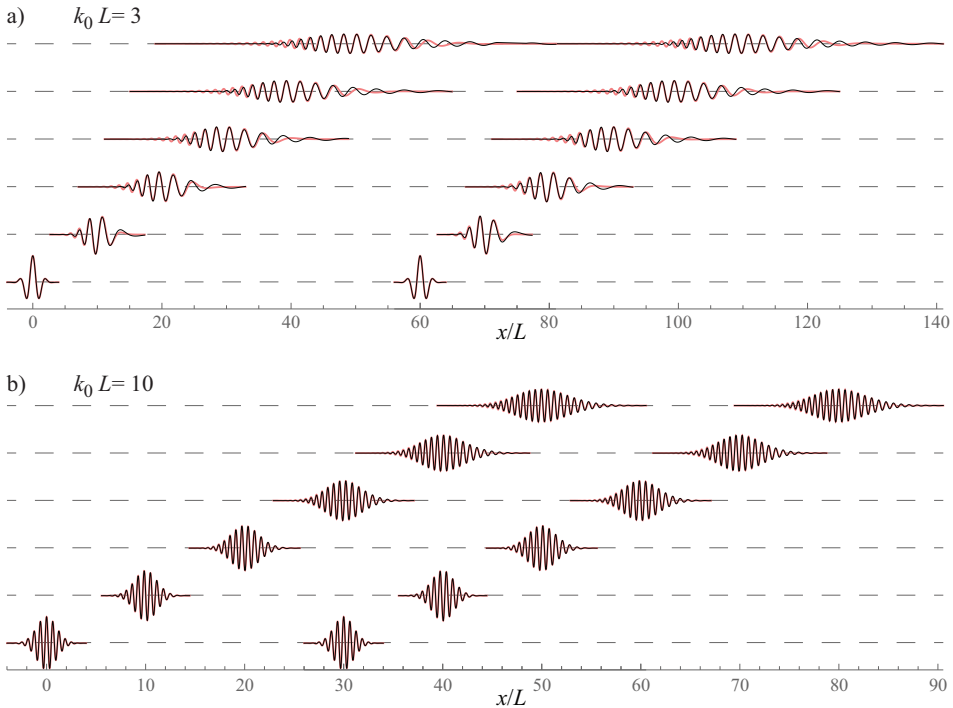
20 *Wave focusing on a shear current*

Fig. 6 Comparison of exact and approximate linear solution for a defocusing Gaussian wave group on linear currents with $\tilde{\sigma} = -0.5$ and $\tilde{\sigma} = 0.5$ for the packets to the left and right on each horizontal line, respectively, as a function of x measured in number of “widths” L of the Gaussian envelope at focus. The first time (bottommost line of graphs) is at focus, whereupon defocusing is illustrated with time increasing from bottom to top in each panel by intervals $\Delta T = 10L/c_g$ with $c_g(k_0) = A_{0,\text{lin.}}$ from Eq. (58) (i.e., the group travels 10 times the ‘envelope width’ between subsequent times). Thin black line: full linear solution (52), thick red graph: approximation (56). a) Short group, $k_0 L = 3$, focusing at $x = 0$ and $x = 60L$. b) Long group, $k_0 L = 10$ focusing at $x = 0$ and $x = 30L$, respectively.

501 as

$$A_{0,\text{lin.}} = \frac{1}{2}c_0(\varkappa_0); \quad B_{0,\text{lin.}} = -\frac{1}{4}c_0(\varkappa_0)/\varkappa_0 \quad (58)$$

502 with $c_0(k) = \sqrt{g/k}$ as usual. Insertion into (56) gives the approximation of
 503 $\zeta(x, t)$ for a long Gaussian focusing group. Expressions for general water depth
 504 are derived in A.3.

505 Figure 6 compares the approximation (56) to the exact linear solution (52)
 506 for Gaussian groups of two different lengths and strong following and opposing
 507 shear, $\tilde{\sigma} = -0.5$ and $\tilde{\sigma} = 0.5$ for the left and right group on each horizontal line,
 508 respectively. In Fig. 6b a moderately long packet ($k_0 L = 10$) is considered, and
 509 the approximation (56) is excellent in all cases, out to having propagated 50
 510 times the initial group width. Surprisingly, Fig. 6a shows how even for a short
 511 package $k_0 L = 3$ performs reasonably well especially in the central region of
 512 the group. In accordance with our discussion in Section 3.1, the development
 513 of the envelopes in time is indistinguishable for the two opposite, strong shear

514 currents, making still images of surface elevations such as these qualitatively
515 indistinguishable.

516 3.4.2 Arbitrary current with weak shear

517 The first two derivatives of $\sigma_\delta(k)$ from equation (22) are

$$\sigma'_\delta(k) = \int_{-\infty}^0 dz (1 + 2kz) U'_x(z) e^{2kz}; \quad (59a)$$

$$\sigma''_\delta(k) = 4 \int_{-\infty}^0 dz z(1 + kz) U'_x(z) e^{2kz}, \quad (59b)$$

518 from which we obtain, by insertion into Eq. (54), the coefficients A_0 and B_0
519 for use in equation (56)

$$A_{0\delta} = \frac{1}{2} c_0(k_0) - \sigma'_{\delta 0}(k_0); \quad B_{0\delta} = -\frac{1}{4} c_0(k_0)/k_0 - \sigma''_{\delta 0}(k_0). \quad (60)$$

520 Comparison with Eq. (58) shows that the first term on the right-hand sides of
521 Eq. (60) are the no-shear expressions, and the remaining terms are corrections
522 due to the weakly sheared current.

523 The quantities σ_δ , σ'_δ and σ''_δ can be written in closed form for a number of
524 different profiles $U_x(z)$ including the linear current (a special case where the
525 weak-shear theory does not perform particularly well [24]) and the exponential
526 which we consider next.

527 Note in passing that with a partial integration of (22) we may write

$$\sigma_\delta(k) = \frac{1}{2} U'_x(0) - \frac{1}{2} \int_{-\infty}^0 dz U''_x(z) e^{2kz}; \quad (61a)$$

$$\sigma'_\delta(k) = - \int_{-\infty}^0 dz z U''_x(z) e^{2kz}; \quad (61b)$$

$$\sigma''_\delta(k) = - 2 \int_{-\infty}^0 dz z^2 U''_x(z) e^{2kz}; \quad (61c)$$

528 in other words, σ_δ represents the first-order correction to the wave-averaged
529 shear compared to the surface shear because $U_x(z)$ has nonzero curvature.
530 This is an indication why the weak-curvature theory in section 2.4.2 becomes
531 exact for the linear current which has $U''(z) = 0$, and also why the linear
532 current is a special case where weak-shear theory does not perform very well:
533 the shear correction to A_0 and B_0 for linear shear in equation (58) (which
534 is exact for the linear-current case) is symmetrical under $\sigma \rightarrow -\sigma$, but (60)
535 does not have this symmetry under $\sigma_\delta \rightarrow -\sigma_\delta$. Another way of putting it is
536 that when shear-current corrections in the surface-following system may be
537 treated perturbatively, the first-order correction to the phase velocity is due
538 to mean shear, but for the group velocity it is due to mean curvature. When

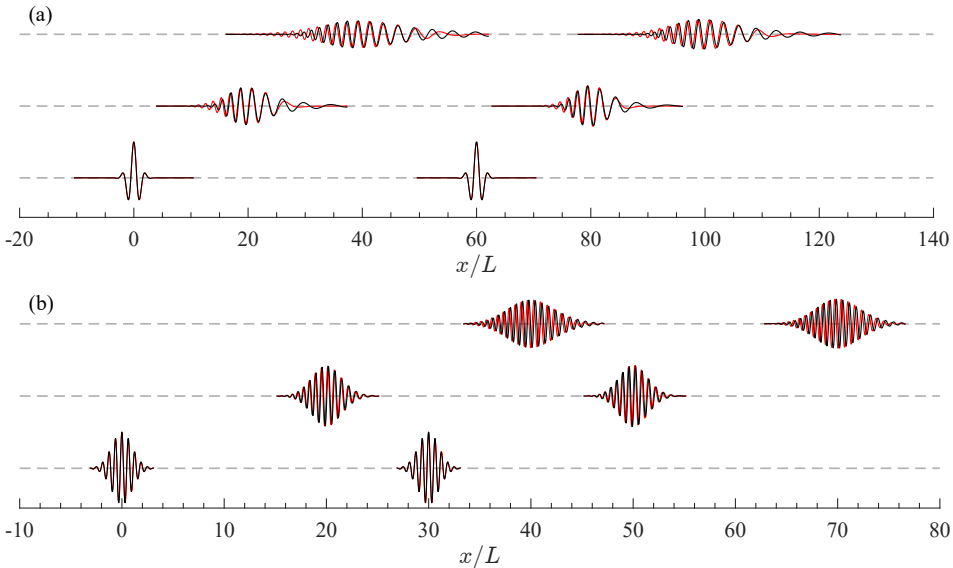
22 *Wave focusing on a shear current*

Fig. 7 Surface elevation of a Gaussian-envelope group on an exponential current (19), where $U_{x0} = 0.2U_{\text{ref}}$ and $-0.2U_{\text{ref}}$ for the wave packets to the left and right, respectively, and $\alpha L = 2.5$. Here $U_{\text{ref}} = \sqrt{gL}$. Red lines refer to the combined narrow-band and weak-shear approximation solution, eqs. (56) and (62). Black lines are the arbitrary-accuracy numerical solution from the DIM algorithm [26]. Top: $k_0 L = 3$ focusing at $x/L = 0$ and 60, bottom: $k_0 L = 10$ focusing at $x/L = 0, 30$. In both panels, ζ is plotted at times (bottom to top) $t = 0, 20L/c_g$ and $40L/c_g$.

539 the curvature vanishes, however, the leading group-velocity correction becomes
540 second order in the average shear. For further discussions, see [20].

541 3.4.3 Exponential shear. Weak-shear approximation vs 542 numerical solution

543 As a particular example consider the exponential current (19). We will see
544 that a number of useful approximate expressions can be found assuming weak
545 shear and exponential current. Note that even the Columbia River delta shear
546 current, considered to be a very strongly sheared current in this context [31],
547 the weak-shear approximation is sufficient for most practical purposes as we
548 detail in section 3.4.4.

549 We find $A_0 = A_{0\alpha}$ and $B_0 = B_{0\alpha}$ with

$$A_{0\alpha} = \frac{1}{2}c_0(k_0) - \frac{U_{x0}\alpha^2}{(2k_0 + \alpha)^2}; \quad B_{0\alpha} = -\frac{c_0(k_0)}{4k_0} + \frac{4U_{x0}\alpha^2}{(2k_0 + \alpha)^3}. \quad (62)$$

550 In figure 7 the approximate solution (56) with coefficients (62) inserted is
551 compared with the ‘exact’ numerical solution of the linear-wave initial value
552 problem. It is striking that although the derivation assumes $k_0 L \gg 1$, the
553 approximation is reasonable already for $k_0 L = 3$. Moreover, the shear is here
554 not extremely weak; from equation (33) we find that for maximally opposing

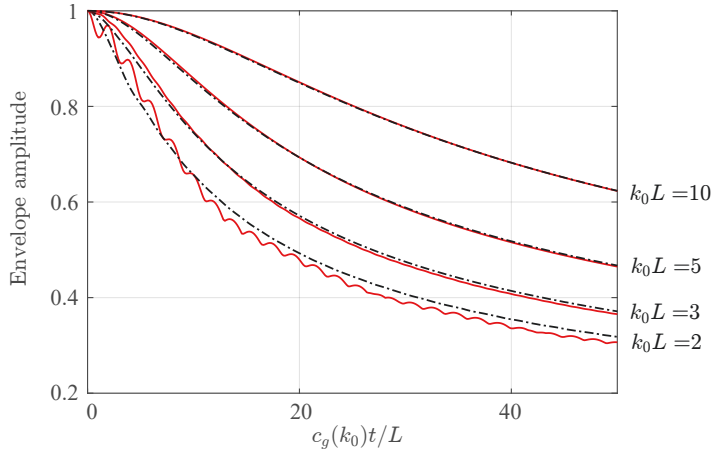


Fig. 8 The decay of envelope amplitude for increasing wave group length k_0L (decreasing spectral bandwidth) on the same exponential shear current as in figure 7. Each point is calculated as the maximum modulus of the Hilbert transform of the analytic surface elevation. Red solid lines: narrow-band weak-shear approximation. Black dash-dot lines: ‘exact’ numerical solution.

555 shear ($\theta = 0$), $\delta(k_0) = 0.10$ and $\delta(k_0) = 0.07$ for $k_0L = 3$ and 10, respectively,
 556 the former of which is slightly higher than that for the Columbia River scenario
 557 we consider in sections 3.4.4 and 4.5.1. This demonstrates the wide applicabil-
 558 ity of the simple closed-form approximation, equations (56) and (62). A slight
 559 phase shift with propagation is observed in both cases in figure 7 due to the
 560 approximate dispersion relation, from equations (23) and (33). In both cases
 561 in figure 7 the envelope is excellently approximated; we quantify this in figure
 562 8 where the decaying height of the defocusing wave group is plotted. Even for
 563 $k_0 = 2$ the agreement is reasonable although this can in no way be called a
 564 ‘narrowband’ wavegroup.

565 3.4.4 Measured current profiles: The Columbia River estuary

566 The flow conditions in the estuary of the Columbia River have been much
 567 studied for a long time (e.g., [32–34]) due to its strong, and strongly sheared,
 568 tidal current, severe wave climate and high shipping traffic. It is also a much
 569 used case for studies of waves interacting with sheared currents in various
 570 contexts (examples include [24, 26, 35–37]).

571 In their study of the Columbia River delta, Zippel & Thomson [38] (ZT)
 572 measured simultaneous wave spectra and shear current profiles in the delta of
 573 the Columbia River. An even more strongly sheared current is found among
 574 the measurements of Kilcher & Nash (KN) from the same area [39] (another
 575 set of measurements is described and used in refs [33, 35, 37]). Their respective
 576 current profiles are shown in figure 9. In section 4.5.1 we also make use of the
 577 measured wave spectrum in reference [38], while here we shall use a model
 578 wave group which at focus is slightly more narrowband than the one measured;
 579 this would represent the situation where only the part of the spectrum near

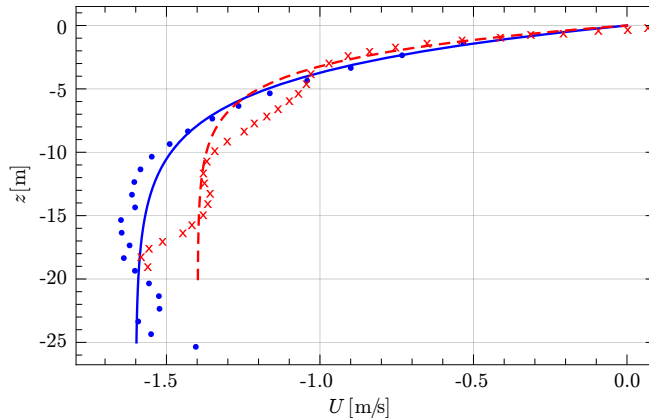


Fig. 9 Shear current profiles of the Columbia River delta current. Measured data by Zippel & Thomson (blue dots) and Kilcher & Nash (red crosses), the lines are exponential functions of form (19) fitted to the data.

580 the peak is involved in the focusing, the remainder forming a small-amplitude
 581 random-phase background which we presently ignore.

582 The velocity profiles shown were shifted to the reference frame following the
 583 mean (Eulerian) surface velocity and fitted to an exponential profile $U(z) =$
 584 $U_0[\exp(\alpha z) - 1]$ (see figure 9c) which gives $U_0 = 1.6$ m/s, $\alpha = 0.26$ m⁻¹ for
 585 current ZT and $U_0 = 1.4$ m/s, $\alpha = 0.39$ m⁻¹ for current KN.

586 To study an example of a focusing group we choose reasonable values for
 587 a dispersively focusing wave group in this location — see also section 4.5.1:
 588 $k_0 = 0.15$ rad/m, $L = 20$ m, which gives $k_0L = 3.0$. We choose for our example
 589 the average of the two values for U_0 and α , respectively.

590 It is worth pointing out at this stage that these parameters give a shear
 591 Froude number of $\delta_{0\alpha} = 0.11$ (KN) and 0.080 (ZT), respectively, when inserted
 592 into equation (33) ($\delta_{0\alpha} = 0.090$ with the chosen model parameters); in other
 593 words, even though the Columbia River current is frequently used as an exam-
 594 ple of a very strongly sheared current where the effect of shear on the waves
 595 is highly significant, we can safely employ weak-shear theory with errors no
 596 greater than a few percent, less than those from typical measurement uncer-
 597 tainty from field measurements. Moreover, although $k_0L = 3$ is not what one
 598 would refer to as a narrowband wave group, we see from Fig. 7 that narrow-
 599 band weak-shear theory gives a more than adequate approximation of the
 600 surface. Thus we may confidently approximate $\zeta(x, t)$ with the approximate
 601 formula (56) with coefficients (62) inserted.

602 With the mentioned approximation we plot a focusing and defocusing wave
 603 group representative of the Columbia River flow conditions, in figure 10. Albeit
 604 less extreme than for the model linear current, the trend is once again clear: in
 605 the case of opposing shear (the focusing group propagates ‘downstream’ in the
 606 river, in an earth-fixed system) the crests and troughs focus and defocus more
 607 gently than for the case of following shear (‘upstream’) where individual crests
 608 and troughs within the group move faster and live shorter. The corresponding

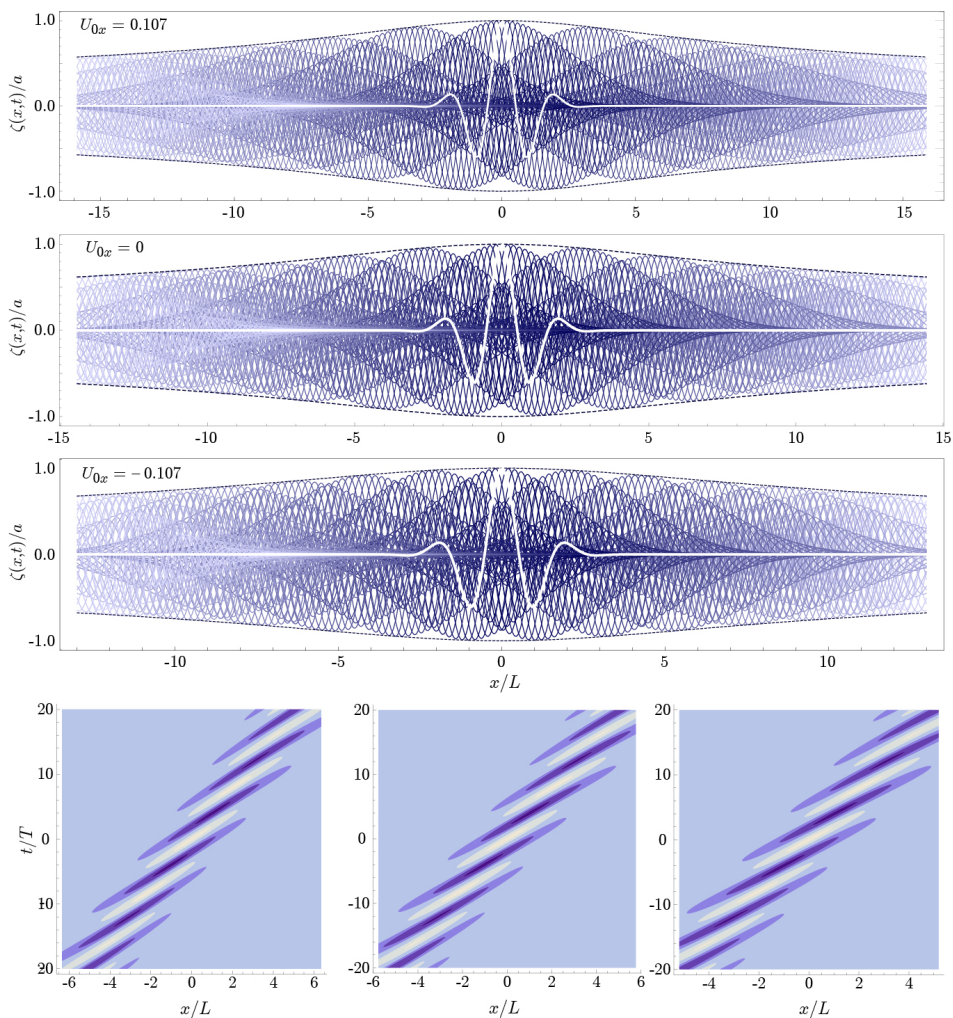


Fig. 10 Same illustration as in figure 2, but with an exponential current representative of the Columbia River, shown in figure 9; see main text for further details. The exponential profile (19) is used with $k_0L = 3$, $\alpha L = 6.5$ and $U_0 = 0.107 U_{\text{ref}}$ with $\theta = 0, \pi/2$ and π (top to bottom). The nondimensional time \tilde{t} runs from from -50 to 50 in steps of 0.4 . The dashed lines are plots of the maximum height, $\pm L(L^4 + B_{0\alpha}^2 t_g(x)^2)^{-1/4}$ with $t_g(x) = x/A_{0\alpha}$.

609 increase in orbital velocities in the latter case is considered and quantified in
 610 section 4.5.1. Once again we notice that the group envelope, represented by
 611 the change in maximum group height with time, varies modestly.

612 3.4.5 Arbitrary current with strong shear

613 Inserting dispersion relation (24) into formula (54) now gives the coefficients
 614 A_0 and B_0 for strong shear in the strong shear, weak curvature approximation

615 (SSWCA) of Ellingsen & Li [20],

$$A_{0,\text{EL}} = \frac{1}{2}c_0(\varkappa_{\delta 0})(1 + 2\sigma_{\delta 0}\sigma'_{\delta 0}/g) - \sigma'_{\delta 0} \quad (63a)$$

$$B_{0,\text{EL}} = -\frac{(g + 2\sigma_{\delta 0}\sigma'_{\delta 0})^2}{4\omega_0(\varkappa_{\delta 0})^3} + \frac{\sigma''_{\delta 0} + \sigma_{\delta 0}\sigma''_{\delta 0}}{\omega_0(\varkappa_{\delta 0})} - \sigma''_{\delta 0}, \quad (63b)$$

616 where we use the shorthand $\varkappa_{\delta 0} = \varkappa_{\delta}(k_0)$ and $\omega_0(\varkappa_{\delta 0}) = \sqrt{g\varkappa_{\delta 0}} = \varkappa_{\delta 0}c_0(\varkappa_{\delta 0})$;
 617 \varkappa_{δ} was defined in equation (25). If the Froude-shear number δ is small we
 618 obtain (60) to leading order, while assuming linear shear ($\varkappa_{\delta}(k) \rightarrow \varkappa$, and
 619 $\sigma'_{\delta} = \sigma''_{\delta} = 0$) yields expressions (58). The SSWCA should replace the weak-
 620 shear approximation when the shear as seen by the significant waves as
 621 extremely strong (by oceanographic standards), i.e., when δ is not small com-
 622 pared to 1, and/or the current shear appears close to constant with depth.
 623 For the exponential current representative of the Columbia River, figure 9,
 624 using expressions (63) instead of (62) gives practically identical results. Deriv-
 625 ing explicit formulae for $A_{0,\text{EL}}$ and $A_{0,\text{EL}}$ with the exponential current (19) is
 626 straightforward, but the resulting expressions are sufficiently bulky that we do
 627 not quote them here. Several realistic situations where the weak-shear theory
 628 is insufficient are mentioned and discussed in reference [20], although these are
 629 not currents which occur in ocean or coastal waters.

630 4 Wave kinematics and orbital velocities

631 We proceed now to considering the shear-affected wave orbital motion. We
 632 consider three cases, a weakly sheared current in the approximation of [14] (see
 633 sections 2.4.1 and 3.4.2), and two cases where an exact solution to the linear
 634 problem exists: a current with constant shear and with exponential shear.

635 Taking a step back to the more general formalism of section 2, we set
 636 $\mathbf{k} = \{k_x, 0\}$ (k_x once again takes either sign) and write the orbital velocities
 637 of a linear plane wave as

$$\begin{bmatrix} u(x, z, t) \\ v(x, z, t) \\ w(x, z, t) \end{bmatrix} = \text{Re} \int_0^{\infty} \frac{dk}{2\pi} \begin{bmatrix} \tilde{u}(z, t; k) \\ \tilde{v}(z, t; k) \\ \tilde{w}(z, t; k) \end{bmatrix} e^{ikx} + \text{c.c.} \quad (64)$$

638 where as before we used that if some function $\varphi(x)$ is real, its Fourier transform
 639 satisfies $\tilde{\varphi}(-k_x) = \tilde{\varphi}^*(k_x)$ to only retain positive values of k . Solving the 3-
 640 dimensional, linearised Euler equation in Fourier form produces the well-known
 641 Rayleigh equation (e.g. [16, 40])

$$\left[\partial_z^2 - k^2 + \frac{\mathbf{k} \cdot \mathbf{U}''(z)}{\omega - \mathbf{k} \cdot \mathbf{U}(z)} \right] \tilde{w}(z, t; \mathbf{k}) = 0 \quad (65)$$

642 (note that $k = |\mathbf{k}| = |k_x|$ here). Once w is found, the horizontal velocity
643 components $\tilde{\mathbf{u}}_{\perp} = \{\tilde{u}, \tilde{v}\}$ are obtained using the general relation [26]

$$k^2(\omega - \mathbf{k} \cdot \mathbf{U})\tilde{\mathbf{u}}_{\perp} = i[\mathbf{k} \cdot \mathbf{U}'\tilde{w} + (\omega - \mathbf{k} \cdot \mathbf{U})\tilde{w}']\mathbf{k} - ik^2\mathbf{U}'\tilde{w}, \quad (66)$$

644 where the arguments of $\tilde{\mathbf{u}}_{\perp}(z, t; \mathbf{k})$, $\tilde{w}(z, t; \mathbf{k})$, $\mathbf{U}(z)$ and $\omega(\mathbf{k})$ are understood,
645 and a prime denotes derivative with respect to z . Note in particular that when
646 $\mathbf{k} = \{k, 0\}$, one finds

$$\tilde{u} = i\tilde{w}'/k; \quad (67a)$$

$$\tilde{v} = \frac{-iU'_y(z)}{\omega - kU_x(z)}\tilde{w}. \quad (67b)$$

647 The eigenvalues of $\omega(k)$ are real provided the denominator in (65) is not zero
648 [41], i.e., no critical layer exists. We shall assume this to be the case, physically
649 implying that no critical layers occur.

650 Equation (67b) shows how the orbital velocities are modified by the shear
651 current also for $\theta = \pi/2$ (i.e., $\mathbf{k} \cdot \mathbf{U} = kU_x = 0$), even though the surface
652 elevation is equal to that without current in that case (equation (3) shows
653 that ζ is affected by the current only via the dispersion relation $\omega(\mathbf{k})$, in turn
654 obtained as eigenvalues of the Rayleigh equation (65) which depends only on
655 $\mathbf{k} \cdot \mathbf{U}$.)

656 We now define

$$\tilde{w}(z, t; k) = \tilde{w}(0, t; k)e^{kz}f(z; k) \quad (68)$$

657 with $f(0; k) = 1$. The function f differs from 1 when $U_x(z)$ has curvature (i.e.,
658 nonzero second derivative) [20] — see e.g., equation (82) below. Thus, from
659 equation (67a),

$$\tilde{u}(z, t; k) = i\tilde{w}(0, t; k)e^{kz}[f(z; k) + f'(z; k)/k]. \quad (69)$$

660 The kinematic boundary condition gives

$$\tilde{w}(0, t; k) = -i\omega(k)\tilde{\zeta}_0(k)e^{-i\omega(k)t} \quad (70)$$

661 where we used (7), whereby we obtain the general expressions

$$w(x, z, t) = 2 \operatorname{Im} \int_0^{\infty} \frac{dk}{2\pi} \omega(k)\tilde{\zeta}_0(k)f(z; k)e^{kz}e^{i\psi(x, t; k)}; \quad (71a)$$

$$u(x, z, t) = 2 \operatorname{Re} \int_0^{\infty} \frac{dk}{2\pi} \omega(k)\tilde{\zeta}_0(k)[f(z; k) + f'(z; k)/k]e^{kz}e^{i\psi(k)t}; \quad (71b)$$

$$v(x, z, t) = -2 \operatorname{Re} \int_0^{\infty} \frac{dk}{2\pi} \frac{\omega(k)U'_y(z)}{\omega(k) - kU_x(z)}\tilde{\zeta}_0(k)f(z; k)e^{kz}e^{i\psi(k)t}. \quad (71c)$$

662 We define the surface velocity amplification as the ratio of the horizontal
663 orbital velocity at the (linearised) surface at the point of focus, $u(0, 0, 0)$, with

664 vs without shear;

$$\text{amp}_0 = \frac{\text{Re} \int_0^\infty dk \omega(k) \tilde{\zeta}_0(k) [1 + f'(0; k)/k]}{\text{Re} \int_0^\infty dk \omega_0(k) \tilde{\zeta}_0(k)} \quad (72)$$

665 with $\omega_0(k) = \sqrt{gk}$ as usual, and noting that $f(z; k) \rightarrow 1$ without shear.

666 In the presence of following shear where $U'_x(z)$ is primarily positive, the
667 maximum of the horizontal velocity at focus $u(0, z, 0)$ can lie below the surface.
668 In this case we define a maximum amplification

$$\text{amp}_{\max} = \max_z \left\{ \frac{u(0, z, 0)}{u_0(0, 0, 0)} \right\}, \quad (73)$$

669 where u_0 is the horizontal velocity of the no-current case.

670 4.1 Long Gaussian group (narrow-band)

671 Assume now as in section 3.4 the initial shape $\tilde{\zeta}_0(k)/aL = \sqrt{\pi/2} \exp[-\frac{1}{2}(k -$
672 $k_0)^2 L^2]$ with $k_0 L \gg 1$. We may restrict ourselves to the upper range of the
673 water column $|z| \ll k_0 L^2$, which is no significant limitation since velocities,
674 which decay exponentially as $\exp(k_0 z)$, are negligible when $|z| \sim k_0 L^2 \gg L$.
675 The Laplace integral approximation becomes identical as in in section 3.4 with
676 expansion around $k = k_0$, giving the orbital velocities as the real part of

$$u \approx \frac{ac(k_0)L}{\sqrt{L^2 + iB_0 t}} \exp \left[ik_0 x - i\omega(k_0)t - \frac{(x - A_0 t)^2}{2(L^2 + iB_0 t)} \right] \frac{d}{dz} [f(z; k_0) e^{k_0 z}]; \quad (74a)$$

$$v \approx -\frac{ac(k_0)k_0 L}{\sqrt{L^2 + iB_0 t}} \exp \left[ik_0 x - i\omega(k_0)t - \frac{(x - A_0 t)^2}{2(L^2 + iB_0 t)} \right] \frac{U'_y(z) f(z; k_0) e^{k_0 z}}{\omega(k_0) - k_0 U_x(z)}; \quad (74b)$$

$$w \approx \frac{-iac(k_0)k_0 L}{\sqrt{L^2 + iB_0 t}} \exp \left[ik_0 x - i\omega(k_0)t - \frac{(x - A_0 t)^2}{2(L^2 + iB_0 t)} \right] f(z; k_0) e^{k_0 z}, \quad (74c)$$

677 with A_0, B_0 as in equation (54). We leave it to the reader write out the real
678 part along the lines of equation (56) if desired. Correction terms of order
679 $(x - A_0 t)/k_0 L$ enter far from the centre of the group at $x = A_0 t$.

680 In the narrowband case it is opportune to also define a surface-shear number

$$\Upsilon_0 = \frac{U'_x(0)}{\omega_0(k_0)} \quad (75)$$

681 as well as a current strength number

$$\mathfrak{U}_0 = \frac{\max[U_x] - \min[U_x]}{c_0(k_0)}. \quad (76)$$

682 Here $\omega_0(k_0) = k_0 c_0(k_0) = \sqrt{gk_0}$ as usual, and the functions \max and \min find
683 extrema with respect to z .

In particular, for linear shear (13)

$$\Upsilon_{0,\text{lin.}} = \frac{2\sigma}{\sqrt{gk_0}} = 2 \text{FS}_{\text{lin.}} \cos \theta = 2\delta_{\text{lin.}},$$

684 (σ was defined in equation (16)) whereas \mathfrak{U}_0 is not defined in deep water. For
685 the exponential current profile in the Stewart & Joy weak-shear approximation,
686 see section 4.2.1.

687 4.2 Wave kinematics with arbitrary, weakly sheared 688 current

689 In this section we derive expressions for the orbital velocities under a focusing
690 wave group on an arbitrary, weakly sheared current. Special cases of the final
691 expressions, equations (83), will be simplified further in the following.

692 Consider a focusing wave group on a current $\mathbf{U}(z) = \{U_x, U_y\}(z)$ which is
693 well described by the approximate theory first put forward by Stewart & Joy
694 [14, 42] as described in section 3.4.2. This is typically a very good approxi-
695 mation even in strongly sheared oceanic flows (e.g. [20, 24, 26]). The orbital
696 velocities of a linear plane wave of wave number k of either sign in the xz -
697 plane for such a situation have been found using assumptions of weak current
698 [14, 42], although as discussed in section 2.4.1 these approximations are in
699 fact valid for weakly sheared current, usefully measured via the small-shear
700 parameter (or Froude number) $\delta(\mathbf{k})$ (see Eq. (20)).

701 The vertical orbital velocity to $\mathcal{O}(\delta)$ is [20, 42]

$$\tilde{w}(z, t; k) = \tilde{w}_0(0, t; k) e^{kz} [1 - \Delta(z; \mathbf{k})]; \quad (77)$$

702 plus terms of $\mathcal{O}(\delta^2)$, \tilde{w}_0 is the vertical velocity without current (which can be
703 related to $\tilde{\zeta}_0$ via equation (70)), and

$$\Delta(z; \mathbf{k}) \equiv \frac{1}{c_0} \int_{-\infty}^z d\tilde{z} U'_x(\tilde{z}) e^{2k(\tilde{z}-z)}. \quad (78)$$

704 Comparison with (20) reveals that

$$\Delta(0; \mathbf{k}) = \delta(\mathbf{k}), \quad (79)$$

705 hence $\Delta(z; \mathbf{k})$ is a generalisation of the small-shear Froude number $\delta(\mathbf{k})$ but
706 with contributions only from the wave-aligned current component $U_x(z)$ at
707 depths greater than $|z|$. (Note: Δ must not be confused with the quantity of
708 the same name in ref [20]). Clearly $\Delta \sim \mathcal{O}(\delta)$. The dependence of Δ and δ on
709 \mathbf{k} will often be suppressed. We will need the derivative

$$\Delta'(z) = -2k\Delta(z) + U'_x(z)/c_0. \quad (80)$$

30 *Wave focusing on a shear current*

710 The corresponding horizontal velocities, obtained via equation (67), are

$$\tilde{u}(z, t; \mathbf{k}) = i\tilde{w}_0(0, t; k)e^{kz} [1 + \Delta(z; \mathbf{k}) - U'_x(z)/\omega_0], \quad (81a)$$

$$\tilde{v}(z, t; \mathbf{k}) = -i\tilde{w}_0(0, t; k)e^{kz}U'_y(z)/\omega_0 \quad (81b)$$

711 plus terms of order δ^2 .

712 In the formalism of equation (68),

$$f(z; k) = \frac{1 - \Delta(z; \mathbf{k})}{1 - \delta(\mathbf{k})}. \quad (82)$$

713 The function only occurs in equations (71) in the constellation $\omega(k)f(z; k) =$
714 $\omega_0(k)[1 - \Delta(z; \mathbf{k})]$, using the weak-shear dispersion relation in equation (23).

715 We shall also require the derivative $\omega f'(z) = 2k\omega_0\Delta(z; \mathbf{k}) - kU'_x(z)$ so that
716 $\omega f'(0) = 2\omega_0k\delta - kU'_x(0)$.

717 For a group which at $t = 0$ focuses to a shape $\zeta(x, 0)$ the velocity fields are
718 found by insertion into (71):

$$u(x, z, t) = 2 \operatorname{Re} \int_0^\infty \frac{dk}{2\pi} \omega_0(k) \tilde{\zeta}_0(k) \left[1 + \Delta(z; \mathbf{k}) - \frac{U'_x(z)}{\omega_0} \right] e^{kz+i\psi}, \quad (83a)$$

$$v(x, z, t) = -2U'_y(z) \operatorname{Re} \int_0^\infty \frac{dk}{2\pi} \tilde{\zeta}_0(k) e^{kz+i\psi}, \quad (83b)$$

$$w(x, z, t) = 2 \operatorname{Im} \int_0^\infty \frac{dk}{2\pi} \omega_0(k) \tilde{\zeta}_0(k) [1 - \Delta(z; \mathbf{k})] e^{kz+i\psi}, \quad (83c)$$

719 plus corrections of order δ^2 ; here, $\psi = \psi(x, t; k)$.

720 The surface velocity amplification for an arbitrary $\mathbf{U}(z)$ satisfying $\delta(\mathbf{k}) \ll 1$
721 for all significantly contributing k , from equation (72), is now

$$\operatorname{amp}_{\text{w.s.,0}} = 1 + \frac{\int_0^\infty dk \operatorname{Re}\{\tilde{\zeta}_0(k)\} [\omega_0\delta(\mathbf{k}) - U'_x(0)]}{\int_0^\infty dk \omega_0 \operatorname{Re}\{\tilde{\zeta}_0(k)\}}. \quad (84)$$

722 **4.2.1 Gaussian wave group on exponential weak shear**

723 Consider the same situation as in section 3.4.3: a Gaussian wave packet with
724 carrier wave number k_0 considerably greater than L^{-1} i.e., the group is fairly
725 narrowbanded. The current profile is exponential, (19) in the now familiar
726 weak-shear approximation. A subscript ‘ α ’ will refer to the exponential current
727 as before, and a subscript 0 means evaluation at $k = k_0$. The velocity fields
728 are readily found from (83) by inserting $\{U'_x, U'_y\}(0) = \alpha\{U_{x0}, U_{y0}\}e^{\alpha z}$ and
729 $\Delta(z) = \Delta_\alpha(z)$ where

$$\Delta_\alpha(z) = \delta_\alpha e^{\alpha z} \quad (85)$$

730 with $\delta_\alpha(\mathbf{k})$ from Eq. (33). We define the shorthand

$$\mathbf{a} \equiv \alpha/k_0. \quad (86)$$

731 and note that for the exponential current the definitions (75) and (76) yield

$$\mathfrak{U}_{0\alpha} = \frac{U_{x0}}{c_0(k_0)}; \quad \Upsilon_{0\alpha} = \frac{\alpha U_{x0}}{\omega_0(k_0)} = \mathfrak{a}\mathfrak{U}_{0\alpha}; \quad \delta_{\alpha 0} = \frac{\mathfrak{a}\mathfrak{U}_{0\alpha}}{\mathfrak{a} + 2}. \quad (87)$$

732 We find from equations (74) and (85) — with (82) and noting that $c(k_0) =$
733 $\omega_0(k_0)(1 - \delta_{\alpha 0})/k_0$ in the Stewart & Joy approximation (23) — that the orbital
734 velocities are approximated by

$$u(x, z, t) \approx \text{Re} \left\{ \frac{a\omega_0(k_0)L}{\sqrt{L^2 + iB_{0\alpha}t}} [1 - (1 + \mathfrak{a})\delta_{\alpha 0}e^{\alpha z}] e^{\Psi_0(x, z, t)} \right\}; \quad (88a)$$

$$v(x, z, t) \approx -\text{Re} \left\{ \frac{aU'_y(z)L}{\sqrt{L^2 + iB_{0\alpha}t}} e^{\Psi_0(x, z, t)} \right\}; \quad (88b)$$

$$w(x, z, t) \approx \text{Im} \left\{ \frac{a\omega_0(k_0)L}{\sqrt{L^2 + iB_{0\alpha}t}} [1 - \delta_{\alpha 0}e^{\alpha z}] e^{\Psi_0(x, z, t)} \right\} \quad (88c)$$

735 with the shorthand

$$\Psi_0(x, z, t) = k_0z + ik_0x - i\omega(k_0)t - \frac{(x - A_{0\alpha}t)^2}{2(L^2 + iB_{0\alpha}t)}, \quad (89)$$

736 and $\Upsilon_{0\alpha}$ from equation (87). $A_{0\alpha}$ and $B_{0\alpha}$ were given in equation (62). The
737 approximate expression (88a) is compared to the exact analytical expression
738 presented below in section 4.4.2 in figure 13.

739 The surface amplification is now easily found from equation (88a),

$$\text{amp}_0 = 1 - (1 + \mathfrak{a})\delta_{\alpha 0}. \quad (90)$$

740 Equation (88) demonstrates a striking observation mentioned above: when
741 shear is opposing, i.e., $\Upsilon_0 > 0$, the maximum value of u is not necessarily
742 at $z = 0$ but can be positioned below the surface. With the approximate
743 expression (88a), the criterion for the maximum to lie below the surface —
744 that $u'(z) < 0$ at $z = 0$ — is readily found to be

$$(\mathfrak{a} + 1)^2\delta_{\alpha 0} > 1 \quad (91)$$

745 or alternatively

$$\mathfrak{U}_{0\alpha} > \frac{\mathfrak{a} + 2}{\mathfrak{a}(\mathfrak{a} + 1)^2} \sim \mathfrak{a}^{-2} + \dots \quad (92)$$

746 with the current strength parameter $\mathfrak{U}_{0\alpha}$ from equation (87). The last form
747 is the asymptotic expansion as $\mathfrak{a} \gg 1$, which is good to better than 10% for
748 $\mathfrak{a} \gtrsim 3.5$. A sufficient criterion for (92) to hold valid asymptotically as $\mathfrak{a} \rightarrow \infty$
749 is thus simply that the maximum lies beneath the surface if

$$\mathfrak{a}^2\mathfrak{U}_{0\alpha} > 1. \quad (93)$$

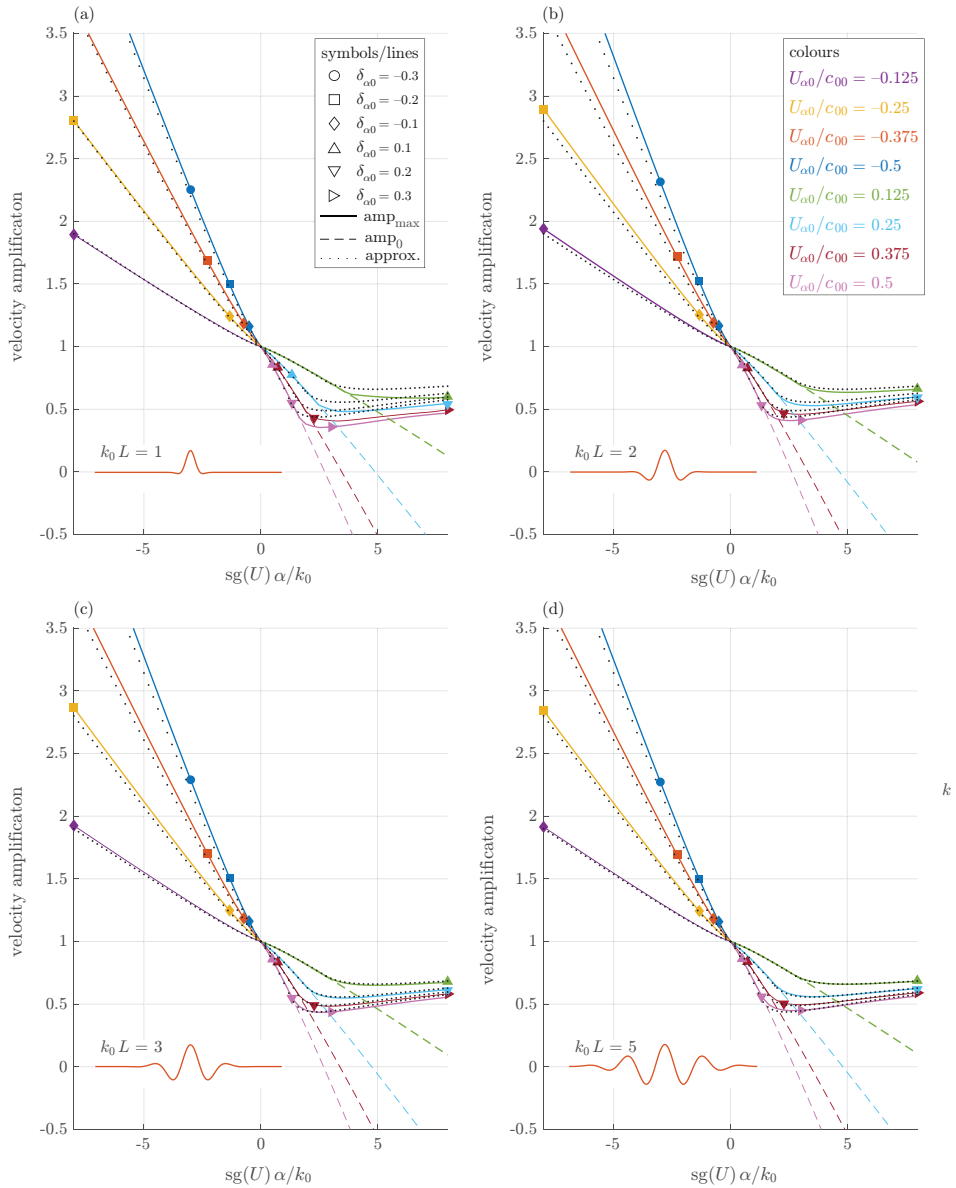


Fig. 11 Velocity amplification for an exponential current. Marker shapes indicate values of $\delta_{\alpha 0}$ as quoted in the legend of panel (a), and graphs and markers are colour coded as the legend in panel (b) shows; both legends are common to all panels; we defined $c_{00} = c_0(k_0)$. The solid lines show the maximum amplification, while the dashed lines of the same colour show the surface amplification (visible only when the two are different). The small black dots show the weak-shear narrowband approximation of equation (95). The insets show the shape of the wave group at focus.

750 Note that the large- \mathbf{a} limit is not in contradiction to the weak-shear approxi-
751 mation if $\mathfrak{U}_{0\alpha} \ll 1$ since $\lim_{\mathbf{a} \rightarrow \infty} \delta_{\alpha 0} = \mathfrak{U}_{0\alpha}$.

752 For $U_{x0} > 0$ the maximum value of u is located where $u'(z) = 0$, provided
753 this occurs at a negative z , otherwise it is at $z = 0$. Differentiating (88a) we
754 find the maximum value at focus to be at level $z_{\max, \alpha}$ and give amplification
755 $\text{amp}_{\max, \alpha}$ as follows,

$$z_{\max, \alpha} = \min \left\{ 0, -\frac{1}{\alpha} \ln[(\mathbf{a} + 1)^2 \delta_{\alpha 0}] \right\}; \quad (94)$$

$$\text{amp}_{\max, \alpha} = \begin{cases} \frac{\alpha}{1+\alpha} [(\mathbf{a} + 1)^2 \delta_{\alpha 0}]^{-1/\alpha}, & \text{if } (\mathbf{a} + 1)^2 \delta_{\alpha 0} > 1, \\ 1 - (\mathbf{a} + 1) \delta_{\alpha 0}, & \text{otherwise} \end{cases} \quad (95)$$

756 with $\delta_{\alpha 0}$ from equation (87). Asymptotes for $\mathbf{a} \rightarrow \infty$ are

$$\text{amp}_{\max, \alpha} \approx \begin{cases} 1 - \frac{1 + \ln(\mathfrak{U}_{0\alpha} \mathbf{a}^2)}{\alpha} + \dots, & \mathfrak{U}_{0\alpha} > 0; \\ -\alpha \mathfrak{U}_{0\alpha} + 1 + \mathfrak{U}_{0\alpha} + \mathcal{O}(\mathbf{a}^{-1}) & \mathfrak{U}_{0\alpha} < 0, \end{cases} \quad (96)$$

757 while

$$\text{amp}_{\max, \alpha} \approx 1 - \frac{1}{2} \alpha \mathfrak{U}_{0\alpha} + \dots, \quad \mathbf{a} \rightarrow 0. \quad (97)$$

758 Equation (95) is a main result of this paper. Although derived assuming a
759 narrowband wave package, it approximates the velocity amplification to within
760 a few percent already for relatively broadband (short) wave groups, $k_0 L = 2$.
761 As the inset of figure 11 shows, this Gaussian group is so short as to hardly
762 be referred to as a “group” at all.

763 The close similarity between the four panels of figure 11 shows with clarity
764 that the amplification factor is essentially determined by two nondimensional
765 groups, the relative current strength $\mathfrak{U}_{0\alpha}$ and the relative shear parameter
766 \mathbf{a} . Moreover, it is striking how closely the simple formulae (95) approximate
767 the numerically calculated amplification for a wide range of parameters of
768 the Gaussian wave group on an exponential profile, even when the underlying
769 assumptions ($k_0 L \gg 1$ and $\delta_{\alpha 0} \ll 1$) are clearly violated.

770 4.3 Wave kinematics with arbitrary strongly sheared, 771 weakly curved current

772 When the current $U_{x0}(z)$ is not weakly sheared, i.e., $\delta(\mathbf{k}) \sim \mathcal{O}(1)$, an approx-
773 imate solution for the vertical velocity is found by applying the method of
774 dominant balance to the Rayleigh equation (65) [20]

$$\tilde{w}(z, t; \mathbf{k}) = \tilde{w}_0(0, t; \mathbf{k}) \left[e^{kz} - \frac{1}{k} \int_{-\infty}^z d\tilde{z} \frac{U_x''(\tilde{z})}{c(\mathbf{k}) - U_x(\tilde{z})} e^{k\tilde{z}} \sinh k(z - \tilde{z}) \right] \quad (98)$$

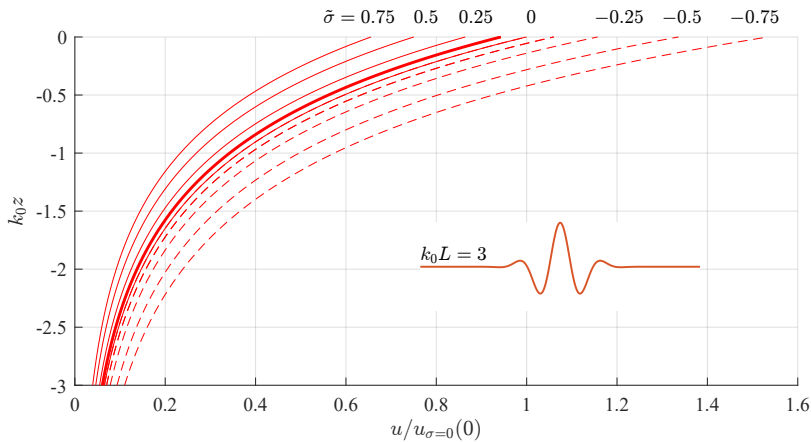


Fig. 12 Horizontal velocity profiles with linear shear current. The shear profile is expressed as $U_x(z) = 2\sigma z$ with, left to right, $\bar{\sigma} = \{0.75, 0.5, 0.25, .0125, 0, -0.125, -0.25, -0.5, -0.75\}$. The wave shape at focus, shown as inset, is $\zeta(x, 0, t)/a = \exp(-\frac{1}{2}x^2/L^2) \cos(k_0 x)$ with $k_0 L = 3$, i.e., a maximum Froude-shear number $|\text{FS}_{\text{lin.}}| = 0.43$ according to equation (18).

with c approximated by equation (24). With (67a) it follows that

$$\tilde{u}(z, t; \mathbf{k}) = i\tilde{w}_0(0, t; \mathbf{k}) \left[e^{kz} - \frac{1}{k} \int_{-\infty}^z d\tilde{z} \frac{U_x''(\tilde{z})}{c(\mathbf{k}) - U_x(\tilde{z})} e^{k\tilde{z}} \cosh k(z - \tilde{z}) \right]. \quad (99)$$

When $U_x(z)/c \ll 1$ these expressions can be reduced to equations (77) and (81a), respectively, in the latter case noting that $\cosh \xi = -\sinh \xi + 2 \exp(\xi)$.

When an exponential current (19) is inserted, the integral can be evaluated in closed form and expressed in terms of a hypergeometric function. However, the resulting expression is no simpler than the exact solution in this case with no restrictions on shear or curvature, presented in 4.4.2. Due to the relative complexity of the analytical expressions we will not pursue the weak-curvature approximation further for the purposes of kinematics.

4.4 Exact linear solutions

Exact solutions to the Rayleigh equation (65) exist for nonzero ω only in special situations [16]. We consider two cases: \mathbf{U} being a linear or exponentially decaying function of z .

4.4.1 Current with linear shear

Consider linear shear, $\mathbf{U}(z) = \{U_x, U_y\} = Sz\{\cos \theta, \sin \theta\}$ and $\omega = \sqrt{\varkappa} - \sigma$, $\varkappa = k + \sigma^2/g$ and $\sigma = \frac{1}{2}S \cos \theta$ as before. The linear-theory orbital velocities for a wave with wave vector $\mathbf{k} = \{k, 0\}$ on such a current are well known. Since $U_x''(z) = 0$, the Rayleigh equation (65) becomes near trivial and following [43] (after a rotation of the coordinate system) gives the simple result

$$\tilde{w}(z, t; \mathbf{k}) = \tilde{w}(0, t; \mathbf{k})e^{kz}; \quad \tilde{u}(z; \mathbf{k}) = i\tilde{w}(0, t; \mathbf{k})e^{kz}. \quad (100a)$$

794 This is ostensibly the potential wave solution, which one obtains for a strictly
795 2-dimensional flow with constant vorticity [43], but note that \tilde{v} is not zero;
796 instead

$$\tilde{v}(z, t; \mathbf{k}) = -\frac{iS \sin \theta}{\omega(\mathbf{k}) - kU_x(z)} \tilde{w}(0, t; \mathbf{k}) e^{kz}. \quad (101)$$

797 This accords with [43] and describes a shifting and twisting of vortex lines as
798 the plane wave passes. \tilde{v} vanishes when shear is zero or the current is parallel
799 or antiparallel to the wave ($\theta = 0$ or π).

800 Thus for the focusing wave group one obtains (notice that with our
801 convention, $\mathbf{k} = \{k, 0\}$ with $k > 0$)

$$w(x, z, t) = 2 \operatorname{Im} \int_0^\infty \frac{dk}{2\pi} \omega(k) \tilde{\zeta}_0(k) e^{kz} e^{i\psi}; \quad (102a)$$

$$u(x, z, t) = 2 \operatorname{Re} \int_0^\infty \frac{dk}{2\pi} \omega(k) \tilde{\zeta}_0(k) e^{kz} e^{i\psi}; \quad (102b)$$

$$v(x, z, t) = -2 \operatorname{Re} \int_0^\infty \frac{dk}{2\pi} \frac{S\omega(k) \sin \theta}{\omega(k) - kU_x(z)} \tilde{\zeta}_0(k) e^{kz} e^{i\psi}. \quad (102c)$$

802 At first glance it might seem as if u and w are not much affected by the
803 shear, having as they do the same structure as the expressions sans current.
804 However, the quantitative effect is highly significant, because as previously
805 discussed the frequency ω contained in ψ varies very significantly with the
806 sign of σ when the latter is not very small compared to \sqrt{gk} . Thus, being
807 proportional to $\omega(k)$, the orbital velocities u, w can be very significantly greater
808 for $\sigma < 0$ compared to $\sigma > 0$. Secondly an oblique angle between wave and
809 current makes for significant horizontal motion across the wave plane (also true
810 for currents of more general depth profile, provided vertical shear is non-zero,
811 according to equation (67b)).

812 For the linear profile the velocity is always highest at the surface, hence
813 the velocity amplification is

$$\operatorname{amp}_{\text{lin}} = \frac{\int_0^\infty dk \omega(k) \operatorname{Re}\{\tilde{\zeta}_0(k)\}}{\int_0^\infty dk \omega_0(k) \operatorname{Re}\{\tilde{\zeta}_0(k)\}} \quad (103)$$

814 with $\omega(k)$ from equation (14). The case of a narrowband wave group is con-
815 sidered in section 4.5, in which case the amplification becomes particularly
816 simple.

817 The qualitative difference in behaviour during focusing and defocusing was
818 illustrated in figures 2 and 3. Figure 12 shows the horizontal velocity pro-
819 files beneath the focus point, $u(0, z, 0)$ for linear shear currents of different
820 strengths, for a Gaussian wave group with $k_0 L = 3$. The qualitative shape of u
821 remains the same, except amplified. The surface amplification varies between
822 approximately 0.65 and 1.52 for the strongest opposing and following shear,
823 respectively.

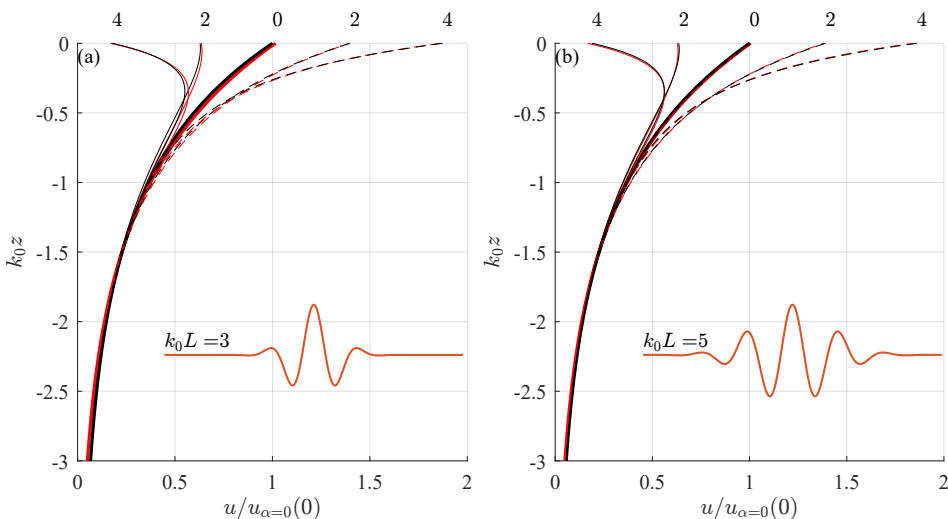


Fig. 13 Horizontal orbital velocity profiles at focus, $u(0, z, 0)$, normalised by the surface value without shear, for a medium-bandwidth focusing wave, $k_0 L = 3$ (a) and $k_0 L = 5$ (b) on an exponential current, equation (19). Insets show the wave group shape at focus. Here $U_{x0} = 0.2 U_{\text{ref}}$ (solid lines) and $-0.2 U_{\text{ref}}$ (dashed lines). Comparison of exact solution [equations (67a) and (106)] (black lines) and the weak-shear narrowband approximation (red lines), equation (88). The values on the top of each curve refer to α/k_0 .

824 4.4.2 Current with exponential shear

825 In the case of an exponential current (19), Hughes & Reid [44] showed that the
826 Rayleigh equation (65) permits the exact solution (see also [45] and Appendix
827 B of [46])

$$\tilde{w}(z, t; k) = \tilde{W}(t; k) {}_2F_1(\mathcal{A}_-, \mathcal{A}_+; \mathcal{R}; \mathcal{W}(z)) e^{kz} \quad (104)$$

828 with ${}_2F_1$ being the hypergeometric function, $\tilde{W}(t, k)$ follows from free-surface
829 boundary conditions, and

$$\mathcal{A}_{\pm} = (k \pm \sqrt{\alpha^2 + k^2})/\alpha; \quad \mathcal{R} = 1 + 2k/\alpha; \quad \mathcal{W}(z) = \frac{kU_{x0}e^{\alpha z}}{\omega + kU_{x0}}. \quad (105)$$

830 The horizontal velocity $\tilde{u}(z, t; k)$ is found from equations (67), $u = i\tilde{w}'/k$,
831 giving

$$\tilde{w}'(z) = k\tilde{w}(z) - \frac{\alpha k U_{x0} \tilde{W}(t; k)}{(\omega + kU_{x0})\mathcal{R}} e^{(k+\alpha)z} {}_2F_1(\mathcal{A}_-+1, \mathcal{A}_++1; \mathcal{R}+1, \mathcal{W}(z)) \quad (106)$$

832 The dispersion relation to find $\omega(k)$ is implicit, given by the combined
833 free-surface boundary condition (see [26])

$$\omega^2 \tilde{w}'(0) - k(gk - \omega \alpha U_{x0}) \tilde{w}(0) = 0. \quad (107)$$

834 whose solution $\omega(k)$ is readily found numerically. Alternatively we may apply
835 the Direct Integration Method [26] directly.

836 The solutions (104) and (106) are exact for linear waves regardless of how
 837 strongly sheared the current is. The comparison of the exact solution using the
 838 theory in this section and the approximate solution in section 4.2.1 is shown
 839 in figure 13. The results demonstrate that the approximate expression gives
 840 fairly accurate solution given a relatively weak shear current. Although the
 841 exact solution (106) can be used without difficulty, the computation of the
 842 hypergeometric function can be time consuming. Therefore, one may consider
 843 the approximate expression instead.

844 4.5 Surface velocity amplification for long, Gaussian 845 groups

846 Consider the case of a long, or narrowbanded, Gaussian group with carrier
 847 wavenumber k_0 , as considered in section 3.4, i.e., $\tilde{\zeta}_0(k)/a = \sqrt{\pi/2}L \exp[\frac{1}{2}(k -$
 848 $k_0)^2 L^2]$, where $k_0 \gg 1$ (as we have seen, $k_0 L \sim 5$ is sufficiently large). At
 849 $x = z = t = 0$ the integrals in equation (72) now particularly simple in the
 850 Laplace approximation, and we obtain

$$\text{amp}_0 \approx \frac{c(k_0)}{c_0(k_0)} \left[1 + \frac{1}{k_0} f'(0; k_0) \right]. \quad (108)$$

851 In other words a typical value of the amplification is, to leading order, the
 852 ratio of phase velocities at the carrier frequency with and without shear, which
 853 as discussed in section 3.1 can vary greatly for realistic shear currents, with a
 854 correction term playing a role if the profile $U_x(z)$ has significant curvature.

855 In particular, for linear shear $U_x(z) = Sz$, we have $f'(z) = 0$ (e.g. [17]) and
 856 with (14),

$$\text{amp}_{\text{lin.shear}} \approx \sqrt{1 + \frac{\sigma^2}{\omega_0^2}} - \frac{\sigma}{\omega_0} = \sqrt{1 + \text{FS}_{\text{lin.}}^2 \cos^2 \theta} - \text{FS}_{\text{lin.}} \cos \theta \quad (109)$$

857 where the shear-Froude number was defined in (18), taken here at $k = k_0$.
 858 This accords with equation (26) which was based on the difference in phase
 859 velocity only.

860 4.5.1 Velocity and amplification in real conditions: the 861 Columbia River Estuary

862 We consider now the current and wave climate measured in the estuary of the
 863 Columbia River, as detailed in section 3.4.4. To make the study as realistic as
 864 possible, we devise a focusing wave based on the wave spectrum reported in
 865 reference [38] and generate a wave field from this. The power spectrum we use
 866 is shown in figure 14 (a).

867 We devise a smooth initial-value spectrum $\tilde{\zeta}_0(k)$ based on the measured
 868 wave spectrum $S(f)$ with $f = \omega/2\pi$ is the wave frequency in cycles per second.
 869 In this paragraph only, we use dimensional units without an asterisk. Unlike for

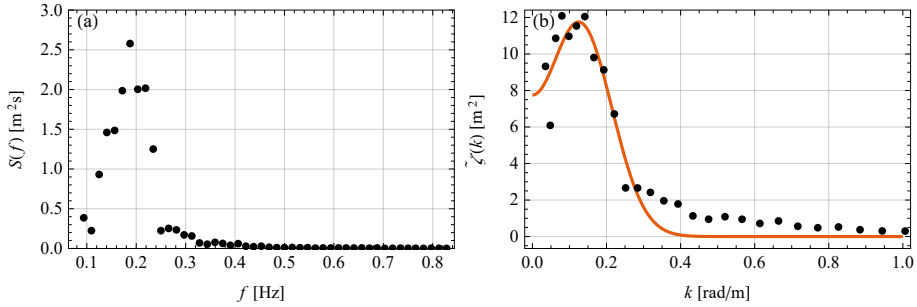


Fig. 14 (a) Power energy spectrum measured in the Columbia River delta [38], (b) initial-value spectrum $\tilde{\zeta}_0(k)$ based on $S(f)$. Circular markers: measured data. Solid line: fitted function.

870 generating a random sea state [47], for a focusing wave group we can obtain an
 871 initial wave elevation spectrum $\tilde{\zeta}_0(k)$ which resembles that which is measured,
 872 as follows. The discrete measured values $\{f_i, S_i\}$ are transformed to a set of
 873 discrete value pairs $\{k_i, \tilde{\zeta}_i\}$,

$$\sqrt{2S_i\Delta f} = \tilde{\zeta}_i\Delta k \quad (110a)$$

$$\tilde{\zeta}_i = \frac{\sqrt{2S_i\Delta f}}{\Delta\omega} \left(\frac{d\omega}{dk} \right)_i = \frac{\sqrt{2S_i\Delta f}}{4\pi^2\Delta f} \frac{g}{2f_i} \quad (110b)$$

874 where we used $\Delta\omega/\Delta k \approx d\omega/dk$, Δf is the distance between frequency values
 875 f_i , and we used $\omega = \sqrt{gk}$. We finally fit the set of points $\{k_i, \tilde{\zeta}_i\}$ to the spectrum
 876 of a broadband Gaussian group, (51), $\tilde{\zeta}_0(k) = \sum_{\pm} a \exp[-L^2(k \pm k_0)^2/2]$,
 877 which gives $k_0 = 0.13$ rad/m and $1/L = 0.087$ /m. The measured spectrum $S(\omega)$
 878 is shown in panel (a) of figure 14, and the smooth $\tilde{\zeta}_0(k)$ is plotted along with
 879 the measurements, transformed with equation (110b) in figure 14(b).

880 The governing nondimensional parameters are thus $\mathfrak{U}_{0\alpha} = 0.18$, $\mathfrak{a} = 2.03$
 881 (ZT) and $\mathfrak{U}_{0\alpha} = 0.16$, $\mathfrak{a} = 3.05$ (KN). The shear-Froude number for current ZT
 882 and KN are $\delta_{\alpha 0} = 0.092$ and 0.095 , respectively, so although these currents are
 883 frequently referred to as very strongly sheared in the context of natural flows
 884 [31, 34, 35], the conditions lie safely in the weak-shear regime where Stewart &
 885 Joy's approximation (sections 2.4.1 and 4.2) can be used. Moreover, although
 886 the wave shape at focus is so broadband as to hardly be called a group (resem-
 887 bling the shape in the inset of figure 11a), the narrow-band approximation
 888 (88a) is an excellent approximation to the velocity profiles at focus.

889 The resulting horizontal orbital velocity profile $u(z, 0, 0)$ at focus is shown
 890 in figure 15(a) for the wave group propagating downstream, across and
 891 upstream on the Columbia River current as seen by an earth-fixed observer,
 892 corresponding to, respectively, maximally opposing, zero and maximally fol-
 893 lowing shear, i.e., $\theta = 0$, $\theta = \pi/2$ and $\theta = \pi$. (Bear in mind that velocities in
 894 our formalism are measured in the system following the mean surface velocity;
 895 see figure 9).

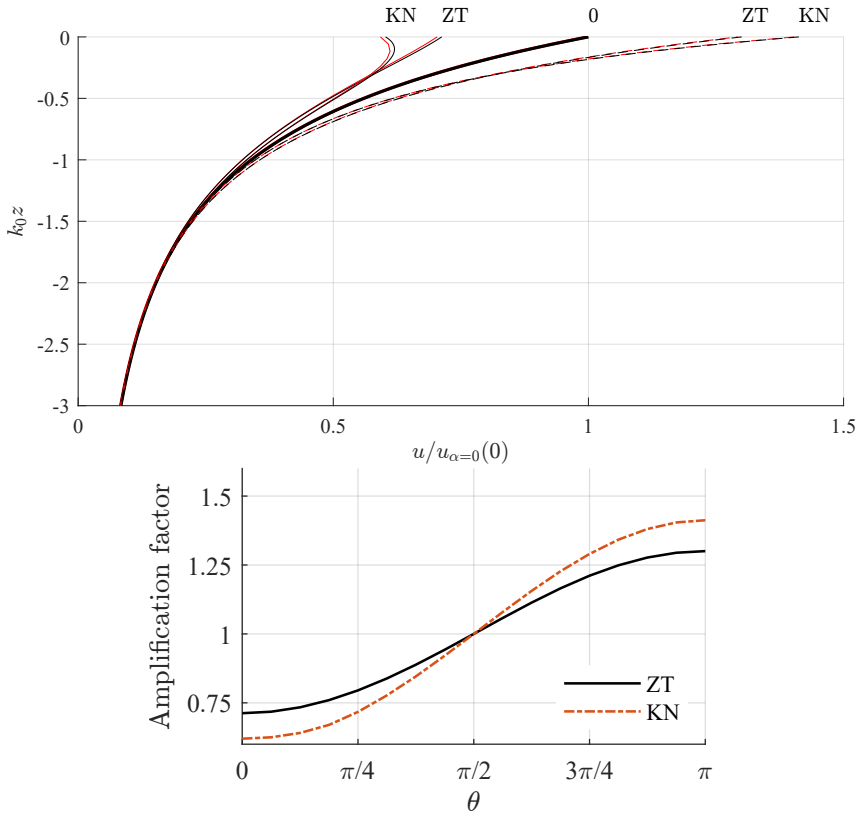


Fig. 15 Top: Horizontal orbital velocity $u(0, z, 0)$ beneath the focus of a medium-bandwidth Gaussian group ($k_0 L = 1.48$) in the presence of measured currents in the Columbia River Estuary, as measured by Zippel & Thomson (ZT, [38]) and Kilcher & Nash (KN, [39]), shifted so that $U(0) = 0$ and approximated by exponentials $U(z) = U_0[\exp(\alpha z) - 1]$. Values for $|U_{x0}|, \alpha, a$ and $\delta_{\alpha 0}$ for ZT and KN are found in the main text. Black lines show ‘exact’ numerical solutions, red lines are the weak-shear-narrowband approximation, equation (88a). Solid, thick, and dashed lines refer to $\cos \theta = 0, \pi/2$ and π , respectively. Bottom: velocity amplification as a function of the angle θ between wave propagation direction and current for the same two velocity profiles.

896 The surface shape at focus is identical by construction, and the envelope
 897 of the focusing and defocusing groups are virtually indistinguishable, yet the
 898 difference in maximum orbital velocity is dramatic. The wave-induced orbital
 899 velocity beneath the focus point, $u(0, 0, 0)$, is increased and reduced by factors
 900 of approximately 1.4 and 0.7 compared to the no-shear case for groups propa-
 901 gating upstream and downstream on the river, respectively. This corresponds
 902 to the wave-induced dynamic pressure, at $x = t = 0$, $p_{\text{dyn}} = \frac{1}{2}\rho u^2$, being
 903 approximately doubled and halved, respectively, very significantly affecting
 904 the force exerted on vessels and constructions. (For balance is worth bearing
 905 in mind that waves propagating against the current are typically higher than
 906 those propagating downstream in this location [38]).

5 Conclusions

We have considered the linearised theory of focusing long-crested wave groups on shear currents of arbitrary vertical depth dependence, allowing an arbitrary angle between the current and wave propagation. Although limited in steepness, a number of insights into the way groups of waves focus and defocus can be gained. We derive a large number of approximate relations which can explicitly reveal the underlying physics, while at the same time being useful tools in their own right, for instance for the generation of focusing wave groups in a wave tank along the lines of [15].

Particular attention is paid to two groups of currents: the current varying linearly with depth, and currents of arbitrary depth dependence whose effect on waves may be approximated using the theory by Stewart & Joy's [14] and others, the criterion for which is that the depth-averaged shear is, in the appropriate sense, sufficiently weak. For the linear current, exact and readily tractable solutions exist, allowing several classical results without shear to be generalised. The "weak-shear" assumption behind the latter class of currents is not a significant limitation in practice, since the vast majority of oceanographic currents and wave spectra satisfy the appropriate criterion of validity. For instance in the Columbia River delta which we consider as an example, the shear is frequently described as being very strongly sheared [31, 34, 35], yet remains safely within the weak-shear assumption's range of validity. The assumption is already in widespread use in ocean modelling (e.g. [35]).

For the much used model of a current profile varying exponentially with depth — modelled as $U(z) = U_0[e^{\alpha z} - 1]$ with $\alpha > 0$ — the weak-shear approximation yields a number of broadly applicable, simple and closed-form approximate relations for the surface elevation of a progressing wave group, and its concomitant orbital velocity field.

Particular attention is paid to Gaussian wave groups which at focus takes the shape of a carrier wave (wavenumber k_0) with a Gaussian envelope of width L : $\zeta_0(x) \propto \exp(-\frac{1}{2}x^2/L^2) \cos k_0x$. Assuming a long group — i.e., narrowband in Fourier space — we may derive a wealth of relations which can describe a wide range of realistic situations. Strikingly, the group does not need to be particularly long (or narrowband): the narrowband results are excellent for most practical purposes already $k_0L = 3$, a group which at the point of focus mainly consists of a single tall crest with deep troughs either side.

A key observation from studying the developing wave group is that while the shear current has modest effect on the evolution of the group envelope, the behaviour inside the group is far more affected. In opposing shear individual crests rise slowly and take longer to traverse the length of the group, while following shear causes the wave behaviour inside the group to appear more volatile, with individual crests and troughs rising and falling more rapidly.

Regarding the orbital wave motion beneath the surface, this difference in behaviour depending on the direction of sub-surface shear becomes even more important. For following shear, horizontal orbital velocities are significantly

952 amplified compared to the case sans shear, and reduced in opposing shear.
 953 The amplification can significantly alter the wave forces acting on a body
 954 encountering the focusing group.

955 We derive a simple approximate relation for the velocity amplification
 956 beneath the focus point of a Gaussian wave group atop an exponential velocity
 957 profile, as a function of two nondimensional groups of parameters: the relative
 958 current strength $U_0\sqrt{k_0/g}$, and the vertical vs horizontal rate of variation,
 959 α/k_0 .

960 For illustration of these observed phenomena in a practical setting we have
 961 considered waves in the mouth of the Columbia River, where depth-resolved
 962 current measurements as well as measured wave spectra are available [38, 39].
 963 For a focusing wave with the same spectrum as that measured, i.e., hav-
 964 ing the same surface elevation $\zeta(x,0)$ at the point of focus, the horizontal
 965 orbital velocity beneath the crest is increased by approximately 40% for fol-
 966 lowing shear (i.e., propagating upstream in an earth-fixed frame) compared
 967 to a depth-uniform current, whereas for opposing shear (downstream propa-
 968 gation) the amplitude is reduced by about a factor 0.72. This corresponds to
 969 the wave-induced dynamic pressure being approximately doubled and halved,
 970 respectively, greatly affecting the forces such a focused group will exert on
 971 vessels and structures.

972 A Linear focusing theory in shallow water

973 A.1 Linear shear

974 The dispersion relation with finite depth h is now (e.g. [43]),

$$\omega(k) = \sqrt{gk \tanh kh + (\sigma \tanh kh)^2} - \sigma \tanh kh. \quad (111)$$

975 Following Refs. [25, 28], the surface elevation integral (11) can be solved
 976 approximately in shallow water by expanding $\omega(k)$ in powers of h and k

$$\begin{aligned} \omega(k) = & kc_h - k\sigma h + \frac{1}{2}k\sigma^2 g^{-\frac{1}{2}} h^{\frac{3}{2}} - g^{-\frac{3}{2}} \left(\frac{1}{6}g^2 k^3 + \frac{1}{8}k\sigma^4\right) h^{\frac{5}{2}} \\ & + \frac{1}{3}k^3 \sigma h^3 - g^{-\frac{3}{2}} \sigma^2 \left(\frac{1}{4}g^2 k^2 - \frac{1}{16}\sigma^4\right) h^{\frac{7}{2}} + \mathcal{O}(h^{\frac{9}{2}}) \end{aligned} \quad (112a)$$

$$\equiv w_1 k - \frac{1}{3} w_3 k^3 + \dots \quad (112b)$$

977 with

$$w_1 = c_h - h\sigma + \frac{1}{2}\sigma^2 g^{-\frac{1}{2}} h^{\frac{3}{2}} - \frac{1}{8}g^{-\frac{3}{2}} k\sigma^4 h^{\frac{5}{2}} + \mathcal{O}(h^3); \quad (113a)$$

$$w_3 = \frac{1}{2}c_h h^2 - \sigma h^3 + \mathcal{O}(h^{\frac{7}{2}}), \quad (113b)$$

978 where $c_h = \sqrt{gh}$ is the phase (and group) velocity in the shallow-water limit
 979 in absence of a shear current.

A.2 δ -function singularity in shallow water with linear current profile

Consider the case of a group focusing to the delta function singularity, equation (47), where the expansion (111) is inserted. We shall need the linear and cubic in k .

Evaluating the integral (47), the surface shape at any time t is then, approximately,

$$\zeta(x, t) = \frac{aL}{(w_3t)^{1/3}} \text{Ai} \left[\frac{x - w_1t}{(w_3t)^{1/3}} \right]. \quad (114)$$

This is a direct generalisation of the result of refs. [25, 28] including a constant shear.

A.3 Gaussian wave group, arbitrary depth

For linear shear S and general depth h , the expressions for $A_0 = \omega'(k_0)$ and $B_0 = \omega''(k_0)$ which may be inserted into (56) are

$$A_0 = -\frac{h\sigma}{C_0^2} + \frac{C_0 S_0 + (2\kappa - k_0)h}{2C_0^2 \sqrt{\mathcal{T}_0}} \sqrt{\frac{g}{\kappa}}; \quad (115a)$$

$$B_0 = \frac{2h^2 \sigma \mathcal{T}_0}{C_0^2} - \sqrt{g\kappa} \mathcal{T}_0 \left[\frac{1}{4\kappa^2} \left(\frac{hk_0}{C_0 S_0} - 1 \right)^2 + \frac{h^2}{C_0^2} \left(2 - \frac{k_0}{\kappa} \right) \right], \quad (115b)$$

with shorthand

$$C_0 \equiv \cosh k_0 h, \quad S_0 \equiv \sinh k_0 h, \quad \mathcal{T}_0 \equiv \tanh k_0 h = S_0/C_0, \quad (116)$$

and shear-modified wave number

$$\kappa = k_0 + \sigma^2 \mathcal{T}_0 / g \longrightarrow \begin{cases} k_0 + \sigma^2 / g & k_0 h \rightarrow \infty \\ k_0 (1 + \sigma^2 h / g) & k_0 h \rightarrow 0 \end{cases}. \quad (117)$$

(Note $\omega(k_0) = \sqrt{g\kappa} \mathcal{T}_0 - \sigma \mathcal{T}_0$ in this formalism).

In the shallow water regime, $k_0 h \equiv \xi_0 \ll 1$ we obtain

$$A_0 = \sqrt{gh} - v_\sigma \xi_0 + \frac{1}{2} (v_\sigma^2 / c_{00}) \xi_0^3 - \frac{1}{2} c_{00} \left(1 + \frac{1}{4} v_\sigma^4 / c_{00}^4 \right) \xi_0^5 + v_\sigma \xi_0^3 + \dots \quad (118a)$$

$$k_0 B_0 = -c_{00} \xi_0^5 + 2v_\sigma \xi_0^3 + \dots \quad (118b)$$

with $c_{00} = c_0(k_0) = \sqrt{g/k_0}$ and $v_\sigma = \sigma/k_0$. For example, from equation (56) one sees that for a Gaussian package the time it takes for the group to change significantly is $t \sim L^2/B_0 \approx (k_0 L^2/c_{00}) \xi_0^{-5/2}$, by which time the group has traveled of order $A_0 t / \lambda_0 \sim (k_0^2 L^2 / 2\pi) \xi_0^{-2}$ wavelengths of the carrier wave. However, notice that the leading-order correction to the phase and group

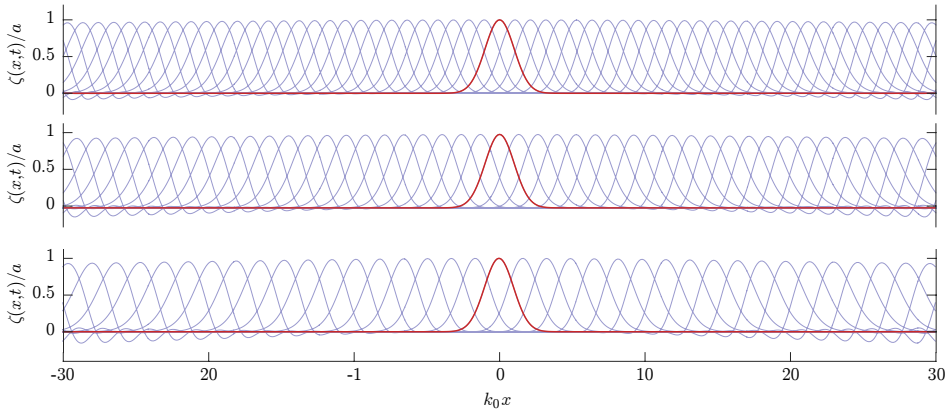


Fig. 16 Waves focusing into a group with a Gaussian envelope in moderately shallow water, $k_0h = 0.2$. The solid graphs show $\eta(x, t)/a$ for $\sqrt{gk_0}t$ from -45 to 45 in steps of 0.5 with the shape at $t = 0$ shown in red. Here $S = \sqrt{gk_0}$, $k_0L = 3$, and $\theta = 0$ (top), $\pi/2$ (centre) and π (bottom).

1001 velocities are order $\text{FS}_{\text{lin.}} \xi_0^{\frac{1}{2}}$ and can be significantly affected by the shear even
 1002 when ξ_0 is not extremely small. This is illustrated in Figure 16 in moderately
 1003 shallow water, $\xi_0 = 0.2$: The group at focus (red graph) does not change shape
 1004 perceptibly, but the phase velocity is clearly increased for $\sigma < 0$ and decreased
 1005 for $\sigma > 0$.

1006 **Conflict of interest.** corresponding author avers that there is no conflict
 1007 of interest.

1008 **Data availability.** No new data was generated in the research reported, and
 1009 all equations necessary to reproduce the results are included.

1010 **Acknowledgments.** SÅE was supported in part by the European Union
 1011 (ERC, WaTurSheD, project 101045299) and the Research Council of Norway
 1012 (project 325114). ZZ acknowledges the support from China Scholarship Council
 1013 through project 201906060137. YL acknowledges the financial support from
 1014 the Research Council of Norway through a FRIPRO mobility grant (project
 1015 no. 287398) and a POS-ERC grant (project no. 342480). Views and opinions
 1016 expressed are those of the authors only and do not necessarily reflect those of
 1017 the European Union or the European Research Council. Neither the European
 1018 Union nor the granting authority can be held responsible for them.

1019 References

- 1020 [1] Kharif, C., Pelinovsky, E.: Physical mechanisms of the rogue wave
 1021 phenomenon. *European Journal of Mechanics-B/Fluids* **22**(6), 603–634
 1022 (2003)
- 1023 [2] Dysthe, K., Krogstad, H.E., Müller, P.: Oceanic rogue waves. *Annu. Rev.*
 1024 *Fluid Mech.* **40**, 287–310 (2008)

- 1025 [3] Onorato, M., Residori, S., Bortolozzo, U., Montina, A., Arecchi, F.: Rogue
1026 waves and their generating mechanisms in different physical contexts.
1027 *Physics Reports* **528**(2), 47–89 (2013)
- 1028 [4] Johannessen, T.B., Swan, C.: A laboratory study of the focusing of
1029 transient and directionally spread surface water waves. *Proceedings of*
1030 *the Royal Society A: Mathematical, Physical and Engineering Sciences*
1031 **457**(2008), 971–1006 (2001)
- 1032 [5] Brown, M.G., Jensen, A.: Experiments on focusing unidirectional water
1033 waves. *Journal of Geophysical Research: Oceans* **106**(C8), 16917–16928
1034 (2001)
- 1035 [6] Grue, J., Clamond, D., Huseby, M., Jensen, A.: Kinematics of extreme
1036 waves in deep water. *Applied Ocean Research* **25**(6), 355–366 (2003)
- 1037 [7] Vyzikas, T., Stagonas, D., Buldakov, E., Greaves, D.: The evolution of free
1038 and bound waves during dispersive focusing in a numerical and physical
1039 flume. *Coastal Engineering* **132**, 95–109 (2018)
- 1040 [8] Adcock, T.A.A., Taylor, P.H.: Focusing of unidirectional wave groups
1041 on deep water: an approximate nonlinear schrödinger equation-based
1042 model. *Proceedings of the Royal Society A: Mathematical, Physical and*
1043 *Engineering Sciences* **465**(2110), 3083–3102 (2009)
- 1044 [9] Kharif, C., Pelinovsky, E., Talipova, T., Slunyaev, A.: Focusing of
1045 nonlinear wave groups in deep water. *JETP Letters* **73**, 170–175 (2001)
- 1046 [10] Kharif, C., Abid, M., Touboul, J.: Rogue waves in shallow water in the
1047 presence of a vertically sheared current. *Journal of Ocean Engineering*
1048 *and Marine Energy* **3**(4), 301–308 (2017)
- 1049 [11] Xin, Z., Li, X., Li, Y.: Coupled effects of wave and depth-dependent
1050 current interaction on loads on a bottom-fixed vertical slender cylinder.
1051 *Coastal Engineering*, 104304 (2023)
- 1052 [12] Zheng, Z., Li, Y., Ellingsen, S.Å.: Dispersive wave focussing on a shear
1053 current. Part 2: Weakly nonlinear theory. Submitted manuscript (2023)
- 1054 [13] Touboul, J., Kharif, C.: Effect of vorticity on the generation of rogue
1055 waves due to dispersive focusing. *Natural Hazards* **84**(2), 585–598 (2016)
- 1056 [14] Stewart, R.H., Joy, J.W.: HF radio measurements of surface currents.
1057 *Deep Sea Research and Oceanographic Abstracts* **21**(12), 1039–1049
1058 (1974). Elsevier
- 1059 [15] Clauss, G.F., Bergmann, J.: Gaussian wave packets: a new approach to

- 1060 seakeeping tests of ocean structures. *Applied Ocean Research* **8**(4), 190–
1061 206 (1986)
- 1062 [16] Peregrine, D.H.: Interaction of water waves and currents. *Advances in*
1063 *Applied Mechanics* **16**, 9–117 (1976)
- 1064 [17] Ellingsen, S.Å.: Initial surface disturbance on a shear current: The
1065 Cauchy-Poisson problem with a twist. *Physics of Fluids* **26**(8), 082104
1066 (2014)
- 1067 [18] Akselsen, A.H., Ellingsen, S.: Weakly nonlinear transient waves on a
1068 shear current: Ring waves and skewed Langmuir rolls. *Journal of Fluid*
1069 *Mechanics* **863**, 114–149 (2019)
- 1070 [19] Abdullah, A.J.: Wave motion at the surface of a current which has an
1071 exponential distribution of vorticity. *Annals of the New York Academy of*
1072 *Sciences* **51**(3), 425–441 (1949)
- 1073 [20] Ellingsen, S.A., Li, Y.: Approximate dispersion relations for waves on
1074 arbitrary shear flows. *Journal of Geophysical Research: Oceans* **122**(12),
1075 9889–9905 (2017)
- 1076 [21] Skop, R.A.: Approximate dispersion relation for wave-current interac-
1077 tions. *Journal of Waterway, Port, Coastal, and Ocean Engineering* **113**(2),
1078 187–195 (1987)
- 1079 [22] Kirby, J.T., Chen, T.-M.: Surface waves on vertically sheared flows:
1080 approximate dispersion relations. *Journal of Geophysical Research:*
1081 *Oceans* **94**(C1), 1013–1027 (1989)
- 1082 [23] Bender, C.M., Orszag, S., Orszag, S.A.: *Advanced Mathematical Methods*
1083 *for Scientists and Engineers I: Asymptotic Methods and Perturbation*
1084 *Theory* vol. 1. Springer, New York (1999)
- 1085 [24] Banihashemi, S., Kirby, J.T., Dong, Z.: Approximation of wave action
1086 flux velocity in strongly sheared mean flows. *Ocean Modelling* (2017)
- 1087 [25] Pelinovsky, E., Talipova, T., Kurkin, A., Kharif, C.: Nonlinear mechanism
1088 of tsunami wave generation by atmospheric disturbances. *Natural Hazards*
1089 *and Earth System Sciences* **1**(4), 243–250 (2001)
- 1090 [26] Li, Y., Ellingsen, S.Å.: A framework for modelling linear surface waves on
1091 shear currents in slowly varying waters. *Journal of Geophysical Research:*
1092 *Oceans* **124**, 2527–2545 (2019)
- 1093 [27] Morse, P.M., Feshbach, H.: *Methods of Theoretical Physics, Pt 1.*
1094 McGraw-Hill, New York (1953)

- 1095 [28] Pelinovsky, E., Talipova, T., Kharif, C.: Nonlinear-dispersive mechanism
1096 of the freak wave formation in shallow water. *Physica D: Nonlinear*
1097 *Phenomena* **147**(1-2), 83–94 (2000)
- 1098 [29] Neumann, G., Pierson, W.J.J.: *Principles of Physical Oceanography*.
1099 Prentice Hall, Englewood Cliffs, N.J. (1966)
- 1100 [30] Magnusson, A.K., Donelan, M.A., Drennan, W.M.: On estimating
1101 extremes in an evolving wave field. *Coastal Engineering* **36**(2), 147–163
1102 (1999)
- 1103 [31] Dong, Z., Kirby, J.T.: Theoretical and numerical study of wave-current
1104 interaction in strongly-sheared flows. *Coast. Engr. Proc.* **1**, 2 (2012)
- 1105 [32] Gonzalez, F.I., Rosenfeld, C.: Star and in situ observations of ocean
1106 swell modification by currents and bathymetry at the Columbia River
1107 entrance. *IEEE Transactions on Geoscience and Remote Sensing* (6),
1108 598–602 (1984)
- 1109 [33] Moritz, H.R., Gelfenbaum, G.R., Kaminsky, G.M., Ruggiero, P., Oltman-
1110 Shay, J., Mckillip, D.J.: Implementing regional sediment management to
1111 sustain navigation at an energetic tidal inlet. In: Kraus, N.C., Rosati, J.D.
1112 (eds.) *Sixth International Symposium on Coastal Engineering and Science*
1113 *of Coastal Sediment Process*, pp. 1768–1786. American Society of Civil
1114 Engineers, Reston, VA (2007). <https://doi.org/10.1061/9780784409268>
- 1115 [34] Kassem, S., Özkan-Haller, H.T.: Forecasting the wave-current interac-
1116 tions at the mouth of the Columbia River, OR, USA. *Coastal Engineering*
1117 *Proceedings* **1**(33), 53 (2012). <https://doi.org/10.9753/icce.v33.waves.53>
- 1118 [35] Elias, E.P., Gelfenbaum, G., Van der Westhuysen, A.J.: Validation of
1119 a coupled wave-flow model in a high-energy setting: The mouth of
1120 the Columbia River. *Journal of Geophysical Research: Oceans* **117**(C9)
1121 (2012)
- 1122 [36] Campana, J., Terrill, E.J., de Paolo, T.: The development of an inversion
1123 technique to extract vertical current profiles from X-band radar observa-
1124 tions. *Journal of Atmospheric and Oceanic Technology* **33**(9), 2015–2028
1125 (2016)
- 1126 [37] Akan, Çiğdem, Moghimi, S., Özkan-Haller, H.T., Osborne, J., Kurapov,
1127 A.: On the dynamics of the Mouth of the Columbia River: Results from a
1128 three-dimensional fully coupled wave-current interaction model. *Journal*
1129 *of Geophysical Research: Oceans* **122**(7), 5218–5236 (2017)
- 1130 [38] Zippel, S., Thomson, J.: Surface wave breaking over sheared currents:

- 1131 Observations from the mouth of the Columbia River. *Journal of Geophysical Research: Oceans* **122** (2017)
1132
- 1133 [39] Kilcher, L.F., Nash, J.D.: Structure and dynamics of the Columbia River
1134 tidal plume front. *J. Geophys. Res.: Oceans* **115**(C5) (2010)
- 1135 [40] Shrira, V.I.: Surface waves on shear currents: solution of the boundary-
1136 value problem. *Journal of Fluid Mechanics* **252**, 565–584 (1993)
- 1137 [41] Morland, L.C., Saffman, P.G., Yuen, H.C.: Waves generated by shear
1138 layer instabilities. *Proceedings of the Royal Society of London. Series A*
1139 **433**(1888), 441–450 (1991)
- 1140 [42] Zakharov, V.E., Shrira, V.I.: Formation of the angular spectrum of wind
1141 waves. *Soviet physics, JETP* **71**, 1091–1100 (1990)
- 1142 [43] Ellingsen, S.Å.: Oblique waves on a vertically sheared current are rota-
1143 tional. *European Journal of Mechanics-B/Fluids* **56**, 156–160 (2016)
- 1144 [44] Hughes, T.H., Reid, W.H.: On the stability of the asymptotic suction
1145 boundary-layer profile. *Journal of Fluid Mechanics* **23**(4), 715–735 (1965)
- 1146 [45] Abid, M., Kharif, C.: Free surface water-waves generated by instability
1147 of an exponential shear flow. Submitted manuscript, in review. <https://arxiv.org/abs/2305.11983>
1148 (2023)
- 1149 [46] Morland, L., Saffman, P.: Effect of wind profile on the instability of wind
1150 blowing over water. *Journal of Fluid Mechanics* **252**, 383–398 (1993)
- 1151 [47] Tucker, M., Challenor, P.G., Carter, D.: Numerical simulation of a random
1152 sea: a common error and its effect upon wave group statistics. *Applied*
1153 *ocean research* **6**(2), 118–122 (1984)

Article III

**Dispersive wave focussing on a shear current. Part 2:
effect of weak nonlinearity**

Zibo Zheng, Yan Li, Simen Å. Ellingsen

This paper is awaiting publication and is not included in NTNU Open

ISBN 978-82-326-7714-6 (printed ver.)
ISBN 978-82-326-7713-9 (electronic ver.)
ISSN 1503-8181 (printed ver.)
ISSN 2703-8084 (online ver.)



NTNU

Norwegian University of
Science and Technology